Numerical Modeling of Hydraulic Fracturing in Weakly Consolidated Sandstones

by

Siavash Taghipoor

A thesis submitted in partial fulfillment of the requirements for the degree of

Doctor of Philosophy

in

Petroleum Engineering

Department of Civil and Environmental Engineering
University of Alberta

Abstract

Hydraulic fracturing is a technique to enhance hydrocarbon production by inducing fracture(s) into reservoir rock. A fracture is induced by injecting fluid into the reservoir at pressures greater than the formation breakdown pressure. The fracture(s) geometry, mode, initiation and propagation pressure, and other characteristics, may vary depending on geomechanical conditions such as in situ stresses and the rock's physical and mechanical properties.

Hydraulic fracturing was originally used to stimulate wellbores drilled into brittle hard rocks. These rocks typically behaved like linear elastic material and exhibited low permeability. Recently, there has been interest in stimulating unconsolidated and poorly consolidated formations which possess low shear strength and high permeability. In these cases, the assumption of linear elastic fracture mechanics (LEFM) and small leak-off from fracture walls may not be valid.

Laboratory experiments have shown that hydraulic fracturing of weakly/unconsolidated sandstones can occur in the form of shear failure/fractures, (a) tensile fracture(s) or a combination of the two. The tensile fracture's conductivity is a nonlinear function of the fracture width. Shear failure/fracturing results in dilative deformation, which enhances rock permeability. Shear dilation increases the local stresses and, consequently, increases the fracturing pressure.

Most of the current continuum-based numerical models require a predetermined hydraulic fracture direction. Some recent continuum models have been adopted to capture fractures in a general direction, but they either lack a proper tensile

fracture-flow law, or do not simulate the development of shear failure/fracture and the interaction between the shear and tensile fractures. Beside continuum-based models, models have been developed based on the discrete element method. These models do not impose the limitations of continuum-based models, but are computationally costly and impractical for large-scale field problems.

The main objective of this research is to develop a hydraulic fracture model for weakly/unconsolidated sandstones and combine it with field observations to study the main mechanisms involved and features required for modeling hydraulic fracturing. These include the fracturing direction, fracture modes and their interaction, and fracturing pressure and its variation over time. This proposed numerical model can simulate poroelasticity effects, rock shear failure/fracturing, tensile fracturing, leak-off, and shear-induced permeability variation.

This thesis presents a method to implement the cubic law to describe the flow inside a tensile fracture in a continuum-smeared tensile fracture model. Touhidi-Bahgini's shear permeability model, which describes the shear-induced permeability enhancement of oil sands, is implemented to simulate shear failure. The smeared shear and tensile fracture schemes (including both geomechanical and flow aspects) are implemented to develop the smeared hydraulic fracture model.

The model is validated by simulating a series of well tests in oil sands during cold water injection. According to the simulation results of the well tests, at injection pressures below the vertical stress, shear failure governs the reservoir response resulting in a breakdown pressure (to induce a tensile fracture) larger

than the maximum in situ stress. Sensitivity analysis illustrate the high sensitivity of the fracturing pressure and length to the minimum and maximum in situ stresses, the mechanical properties of the reservoir sand such as the elastic modulus and cohesion, and the physical properties of the reservoir sand such as the absolute permeability.

Propagation pressure is shown to be directly and fracture length is shown to be inversely proportional to the magnitude of the maximum principal stress as larger deviatoric stress would induce more intense shearing and larger dilation around the wellbore and the tensile fracture. Results also show lower propagation pressure and longer tensile fractures for sandstones with higher cohesion.

A smaller elastic modulus is found to result in a shorter fracture and lower breakdown pressure but higher propagation pressure. It is also shown that absolute permeability of a reservoir has little influence on its breakdown pressure. However, lower permeabilities tend to lower the propagation pressure and increase the length of the tensile fracture.

Preface

The research conducted for this thesis was a part of a research program funded by NSERC through a Collaborative Research Development program supported by BP.

Chapter 3 (excluding the sensitivity analysis) was published as Taghipoor S., Nouri A., Chan D. and Vaziri H., 2013, "Numerical Modeling of Hydraulic Fracturing in Weakly Consolidated Sandstones Using Smeared Fracture Approach," *Canadian Energy and Technology Innovation (CETi) Journal*, vol. 1 (2), CETI 12-050, pp 31-41.

Part of Chapter 4 was published as Taghipoor S., Nouri A. and Chan D. 2015 "Numerical Modeling of Hydraulic Fracturing in Cohesionless Sand – Validation against a Laboratory Experiment," *Journal of Canadian Petroleum Technology (JCPT)*, vol. 54, issue 06, SPE-178439-PA.

A slightly different version of Chapter 5 (excluding the sensitivity analysis) was published as Taghipoor S., Roostaei M., Nouri A. and Chan D., 2014, "Numerical Investigation of the Hydraulic Fracturing Mechanism in Oilsands," *SPE Heavy Oil Conference*, Calgary, Alberta, June 10-12 2014, SPE-170132-MS.

Dedicated to

my lovely wife, Arezoo

for her heart-warming support

and supporting love,

my parents

for their unconditional love

and

my brother, Reza

for his inspiration and encouragement

Acknowledgements

I wish to express my gratitude to my supervisor, Dr. Alireza Nouri, for providing me with the opportunity to study with him, and for his great support, guidance and encouragement during my PhD program.

To Dr. Dave Chan, who stood shoulder-to-shoulder with me during my program and for his fruitful guidance, which enlightened me in my research and my life.

A special thank you to Dr. Bahman Bohloli, Dr. Yashar Pourrahimian, Dr. Ali Abbaspour, Dr. Daniel Oloumi, Dr. Reza Banaei, Mr. Masoud Shafieiefar, Mr. Roobin Roshan Zamir, Mr. Morteza Roostaei, my peer graduate students and other dear friends for their support.

A special thank you to my parents-in-law for their sincere support and love.

I would also like to acknowledge the research funding for this study, provided by NSERC through a Collaborative Research Development program supported by BP.

Table of Contents

CHAPTER 1: INTRODUCTION 1

1.1 MOTIVATION 3
1.2 PROBLEM STATEMENT 4
1.3 RESEARCH OBJECTIVE 5
1.4 RESEARCH METHODOLOGY 6
1.5 THESIS LAYOUT 7
1.6 SIGNIFICANCE OF THE WORK 8

CHAPTER 2: LITERATURE REVIEW 9

2.1 INTRODUCTION 9
2.2 DEFINITION OF FAILURE VERSUS FRACTURE 9
2.3 FRACTURE GEOMETRY 10
2.4 FRACTURING MECHANISMS 11
2.4.1 Fracturing mechanisms in laboratory experiments 12
2.4.1.1 Tensile fracturing mode 12
2.4.1.2 Shear fracturing mode 13
2.4.1.3 Mixed mode 14
2.4.2 Field observations of failure modes in hydraulic fracturing 15
2.4.2.1 Off-Balance Fracture Growth 16
2.4.2.2 Types of Off-Balance Fractures 17
2.4.3 Summary of Field Observations 19
2.5 PARAMETERS THAT AFFECT THE HYDRAULIC FRACTURING RESPONSE 19
2.5.1 Stress-dependent elastic properties 19
2.5.2 Rock Strength 20
2.5.3 Dilation 20
2.5.4 Permeability 20
2.5.5 Fluid Viscosity 21
2.5.6 Stress Magnitude and Direction 22
2.5.7 Wellbore Direction 23
2.5.8 Injection Rate 23
2.6 REVIEW OF NUMERICAL MODELS FOR HYDRAULIC FRACTURE 24
2.6.1 Models with Prescribed Fracture Direction 25
2.6.1.1 Continuum Approaches 25
2.6.1.2 Continuum-Discontinuum Approaches 31
2.6.2 Models without Prescribed Fracture Direction 32
2.6.2.1 Discontinuum Models (Discrete Element Models) 32
2.6.2.2 Continuum Models 34

2.6.2.2.1 Discrete Fracture Approach 34
2.6.2.2.2 Smeared Fracture Approach 35
2.6.3 Assessment of the Existing Tools and Approaches 42
2.7 FRACTURE FLOW FORMULATION 43
2.7.1 Tensile fracture flow equations 43
2.7.2 Transition from Laminar to Turbulent Flow in Fractures 47
2.7.3 Forchheimer Equation for Turbulent Flow in Fractures 47
2.7.4 Izbash Equation (Power Law) for Fully Turbulent Flow in Fractures 48
2.7.5 Shear Failure/Fracture Flow 49
2.7.6 Porosity Alteration 51
2.8 SUMMARY 52

CHAPTER 3: SMEARED HYDRAULIC FRACTURE MODEL: FORMULATION AND MODEL VERIFICATION 54

3.1 INTRODUCTION 54
3.2 THE SMEARED TENSILE FRACTURE FLOW FORMULATION 54
3.3 EXAMINATION OF MESH DEPENDENCY 55
3.4 VERIFICATION OF THE SMEARED TENSILE HYDRAULIC FRACTURE MODEL 58
3.4.1 Numerical Model Description 58
3.4.1.1 Material Properties 59
3.4.1.2 Model and Grid Size 60
3.4.1.3 Initial and Boundary Conditions 60
3.4.1.4 Numerical Modeling Results 61
3.5 SENSITIVITY ANALYSIS 68
3.5.1 Dilation Angle 69
3.5.2 Tensile Strength 70
3.5.3 Fluid Viscosity 71
3.6 SUMMARY AND CONCLUSION 72

CHAPTER 4: SMEARED MODELING OF HYDRAULIC FRACTURING IN COHESIONLESS SAND: VALIDATION AGAINST LABORATORY EXPERIMENTS .. 74

4.1 THE HYDRAULIC FRACTURE EXPERIMENTS 74
4.1.1 Sand Pack Material 75
4.1.2 Testing Procedure 76
4.1.3 Results of the experiments 78
4.2 MODEL FORMULATION 80
4.2.1 Material Constitutive Model 80
4.2.2 Smeared Tensile Fracture Flow Model 80
4.2.3 Smeared Shear Failure Flow Model 81

4.2.4 Fluid Flow Model *81*
4.3 NUMERICAL MODEL SPECIFICATION 82
4.3.1 Model and grid size *82*
4.3.2 Initial and Boundary Condition *82*
4.3.3 Material properties *83*
4.4 VALIDATION RESULTS 84
4.4.1 Calibration of the B Values *84*
4.4.2 Shear and Tensile Failure Zones *88*
4.4.3 Mesh size effect *90*
4.5 SUMMARY AND CONCLUSION 93

CHAPTER 5: A NUMERICAL INVESTIGATION OF THE HYDRAULIC FRACTURING MECHANISM IN OIL SANDS 95

5.1 INTRODUCTION 95
5.2 MODEL FORMULATION 96
5.2.1 Material Constitutive Model *96*
5.2.2 Smeared Tensile Fracture Flow Model *96*
5.2.3 Smeared Shear Failure Flow Model *97*
5.2.4 Fluid Flow Model *98*
5.2.5 Porosity Change *98*
5.3 ITERATIVE COUPLING SCHEME 99
5.4 IMPROVING NUMERICAL STABILITY 100
5.5 SIMULATION OF THE WELL TESTS 102
5.5.1 Reservoir Geology *102*
5.5.2 Description of the Well Tests *103*
5.6 DESCRIPTION OF NUMERICAL MODEL 103
5.6.1 Model and Grid Size *104*
5.6.2 Initial and Boundary Conditions *104*
5.6.3 Reservoir Fluid Properties *106*
5.6.4 Oil Sands Properties *106*
5.6.4.1 Geomechanical Model and Calibration 106
5.6.4.2 Permeability of Oil Sands 108
5.6.4.3 Summary of Oil Sands Properties 109
5.6.5 Single-Phase versus Two-Phase Flow Calculations *110*
5.7 NUMERICAL MODEL RESULTS 112
5.7.1 The Base Numerical Model *112*
5.7.1.1 Absolute Permeability 112
5.7.1.2 Examining Mesh Size Effect 113

5.7.2 Fracture Initiation and Propagation Pressure 118
5.7.3 Sensitivity Analysis..... 121
5.7.3.1 Mesh size effect 122
5.7.3.2 Apparent tensile strength 122
5.7.3.3 The minimum principal stress..... 124
5.7.3.4 The maximum principal stress 125
5.7.3.5 Cohesion 126
5.7.3.6 Elastic Modulus (E) 127
5.7.3.7 Absolute permeability..... 127
5.7.3.8 Shear permeability-evolution rate (B parameter). 129
5.7.3.9 Ramp-up time 130
5.8 CONCLUSION..... 131

CHAPTER 6: CONCLUSION AND DISCUSSION..... 134

6.1 SUMMARY 134
6.2 MAJOR FINDINGS AND CONTRIBUTIONS..... 136
6.3 RECOMMENDATION FOR FUTURE WORK 137

BIBLIOGRAPHY..... 139

APPENDIX A: VALIDATION OF TOUHIDI-BAGHINI'S MODEL FOR SANDSTONE 148

APPENDIX B: CONSTITUTIVE MODEL CALIBRATION FOR SAMPLES FROM COLD LAKE OIL SANDS BASED ON TRIAXIAL COMPRESSION TESTS..... 151

LIST OF TABLES

TABLE 5-1: SUMMARY OF THE INPUT MATERIAL PROPERTIES USED IN THE BASE CASE NUMERICAL MODEL 110

List of Figures

FIG. 2-1: FRACTURING MODES: A) TENSILE MODE, B) SHEAR MODE, C) TEARING MODE, D AND E) COMBINATION OF MODES (DANESHY, 2003) 11
FIG. 2-2: DOMINANT TENSILE MODE OF FRACTURING DURING HYDRAULIC FRACTURING (BOHLOLI AND DE PATER, 2006) 13
FIG. 2-3: SHEAR FAILURE AND BRANCHING DURING HYDRAULIC FRACTURING, A) SHEAR AND SUBPARALLEL FRACTURES DURING CROSS LINK GEL INJECTION WITH 35 LB/MGAL POLYMER LOADING (KHODAVERDIAN AND MCELFRESH, 2000), AND B) SHEAR FAILURE DURING INJECTION OF BENTONITE SLURRY WITH CONCENTRATION OF 150 G/L (BOHLOLI AND DE PATER, 2006) 14
FIG. 2-4: SHEAR STRESS CONCENTRATION IN THE PROCESS ZONE AHEAD OF THE FRACTURE TIP (VAN DAM ET AL., 2000) 14
FIG. 2-5: SCHEMATIC OF POSSIBLE MECHANISMS OF FRACTURE TIP PROPAGATION: A) MOBILITY DRIVEN SHEAR AND TENSILE FRACTURES, AND B) A FORMATION-DAMAGE-DRIVEN FRACTURE (KHODAVERDIAN ET AL., 2010) 15
FIG. 2-6: MULTIPLE FRACTURING, A NEAR WELLEBORE PHENOMENA (DANESHY, 2005) 18
FIG. 2-7: VARIATION OF ELASTIC MODULUS WITH EFFECTIVE CONFINING STRESS (RAHMATI ET AL., 2012; RAHMATI, 2013) 20
FIG. 2-8: HYDRAULIC FRACTURING MECHANISM OF DIFFERENT GEOMATERIALS (PAK, 1997) 21
FIG. 2-9: EFFECT OF INITIAL STRESS STATE ON THE FAILURE MODE 22
FIG. 2-10: INITIATION PRESSURE AS A FUNCTION OF THE WELLBORE DEVIATION ANGLE FROM MAXIMUM HORIZONTAL STRESS (ABASS ET AL., 1996) 23
FIG. 2-11: MULTIPLE PRIMARY FRACTURES FORM BEFORE PROPAGATION OF THE MAIN FRACTURE (JASAREVIC ET AL., 2010) 24
FIG. 2-12: PROCESSES DURING FRACTURING OF OIL SANDS (SETTARI, 1988) 27
FIG. 2-13: QUARTER LAYOUT OF THE FRACTURE/RESERVOIR MODEL (JI ET AL., 2009) 30
FIG. 2-14: CONTINUUM-DISCONTINUUM MODEL BY (ZHANG ET AL., 2010) 31
FIG. 2-15: FRACTURE PATTERN IN DEM MODEL BY COOK ET AL. (2004); A) MULTIPLE FRACTURING IN AN ISOTROPIC STRESS CONDITION, B AND C) FRACTURE PERPENDICULAR TO THE MINIMUM STRESS AT A STRESS RATIO OF 2:1 AND 1:2 (COOK ET AL., 2004) 33
FIG. 2-16: FRACTURE MODEL WITH NODE-SPLITTING TECHNIQUE (PAK, 1997) 34

FIG. 2-17: ZIGZAG CRACK BAND WITH LENGTH "A" AND OVERALL DIRECTION OF THE CRACK (BAŽANT AND OH, 1983) 36
FIG. 2-18: PERMEABILITY CHANGE IN THE MODEL BEFORE AND AFTER FRACTURING (ZHAI AND SHARMA, 2005) 39
FIG. 2-19: WATER PERMEABILITY VS. POROSITY FOR ABSOLUTE PERMEABILITY OF 3000 MD, INITIAL WATER SATURATION OF 15% AND INITIAL POROSITY OF 34% (XU ET AL., 2010) 40
FIG. 2-20: TYPICAL STRESS PATH AND MATRIX MECHANICAL BEHAVIOR (XU AND WONG, 2010) 41
FIG. 2-21: SCHEMATIC OF PERMEABILITY MULTIPLIER AS A FUNCTION OF EQUIVALENT PLASTIC STRAIN (XU AND WONG, 2010) 42
FIG. 2-22: TYPICAL VOLUMETRIC STRAIN BEHAVIOR AND THE CORRESPONDING ABSOLUTE PERMEABILITY VARIATION (TOUHIDI-BAGHINI, 1998) 50
FIG. 2-23: SCHEMATIC REPRESENTATION OF ELASTIC COMPRESSION AND DILATION DURING FRACTURING (YUAN AND HARRISON, 2005) 52
FIG. 3-1: FRACTURE ENERGY DISSIPATION (CROOK ET AL., 2003) 56
FIG. 3-2: COHESIVE BEHAVIOR OF FRACTURE (PAPANASTASIOU, 1999) 59
FIG. 3-3: FINITE DIFFERENCE GRID AND BOUNDARY CONDITIONS 61
FIG. 3-4: FRACTURE APERTURE FOR THE THREE VALIDATION CASES 62
FIG. 3-5: FRACTURE NET-PRESSURE PROFILE FOR THE THREE VALIDATION CASES 64
FIG. 3-6: NET PRESSURE VS. FRACTURE LENGTH FOR THE THREE VERIFICATION CASES 65
FIG. 3-7: COMPARISON OF THE FRACTURE APERTURE FOR THE REGULARIZED AND UN-REGULARIZED STATIC MODELS WITH THE DYNAMIC MODULUS AS WELL AS FOR THE ELASTOPLASTIC MODEL 67
FIG. 3-8: COMPARISON OF THE NET-PRESSURE PROFILE FOR THE REGULARIZED AND UN-REGULARIZED STATIC MODELS WITH THE DYNAMIC MODULUS AS WELL AS FOR THE ELASTOPLASTIC MODEL 68
FIG. 3-9: FRACTURE APERTURE, SENSITIVITY TO THE DILATION ANGLE OF THE ROCK IN THE ELASTOPLASTIC MODEL 69
FIG. 3-10: NET-PRESSURE AT FULL PROPAGATION, SENSITIVITY TO THE DILATION ANGLE OF THE ROCK IN THE ELASTOPLASTIC MODEL 69
FIG. 3-11: COMPARISON OF TENSILE AND SHEAR ZONES IN THE THREE DILATION ANGLE CASES 70
FIG. 3-12: FRACTURE APERTURE, SENSITIVITY TO TENSILE STRENGTH OF THE ROCK IN THE ELASTOPLASTIC MODEL 71
FIG. 3-13: NET PRESSURE AT FULL PROPAGATION, SENSITIVITY TO TENSILE STRENGTH OF THE ROCK IN THE ELASTOPLASTIC MODEL 71
FIG. 3-14: FRACTURE APERTURE, SENSITIVITY TO FLUID VISCOSITY IN THE ELASTOPLASTIC MODEL 72

FIG. 3-15: NET-PRESSURE AT FULL PROPAGATION, SENSITIVITY TO FLUID VISCOSITY IN THE ELASTOPLASTIC MODEL 72
FIG. 4-1: SCHEMATIC CROSS SECTION OF THE LARGE-SCALE TRIAXIAL CHAMBER USED FOR A HYDRAULIC FRACTURE EXPERIMENT (PAK, 1997) 75
FIG. 4-2: LOCATION OF THE PIEZOMETERS FOR TEST NO. 4 OF PHASE II OF THE EXPERIMENTS (PAK, 1997) 77
FIG. 4-3: PATTERN OF FLUORESCENT DYE IN THE SAMPLE (PAK, 1997) 79
FIG. 4-4: FINITE DIFFERENCE MESH AND THE BOUNDARY CONDITIONS 83
FIG. 4-5: VARIATION OF THE FRICTION AND DILATION ANGLES WITH SHEARING PLASTIC STRAIN ... 84
FIG. 4-6: COMPARISON OF THE CALCULATED AND MEASURED PORE PRESSURE AT THE INJECTION POINT 85
FIG. 4-7: COMPARISON OF THE CALCULATED AND MEASURED PORE PRESSURE FOR THE UPPER MONITORING LEVEL (LEVEL 1) 86
FIG. 4-8: COMPARISON OF THE CALCULATED AND MEASURED PORE PRESSURE FOR THE MID-MONITORING LEVEL (LEVEL 2) 87
FIG. 4-9: COMPARISON OF THE CALCULATED AND MEASURED PORE PRESSURES FOR THE LOWER MONITORING LEVEL (LEVEL 3) 88
FIG. 4-10: THE SHEAR FAILURE ZONE (TOP RIGHT), PLASTIC SHEAR STRAINS (BOTTOM) AND THE SIZE OF THE TENSILE FAILURE ZONE (TOP LEFT) IN THE NUMERICAL MODEL 89
FIG. 4-11: MESH SENSITIVITY OF THE RESULTS 91
FIG. 4-12: EVALUATING THE EFFECTIVENESS OF FRACTURE ENERGY REGULARIZATION 92
FIG. 4-13: COMPARISON OF THE DEGRADED ZONE WITH AND WITHOUT FRACTURE ENERGY REGULARIZATION. THE RED COLOUR SHOWS THE FULLY DEGRADED MATERIAL..... 93
FIG. 5-1: COHESIVE BEHAVIOR OF FRACTURE (PAPANASTASIOU, 1999)..... 97
FIG. 5-2:THE ITERATIVE COUPLING SCHEME IN THE DEVELOPED HYDRAULIC FRACTURE MODEL. THE FLUID FLOW MODULE CALCULATES PORE PRESSURES (P). THEN THE PRESSURES ARE MAPPED ONTO THE GEOMECHANICS GRID. THE GEOMECHANICS MODULE CALCULATES THE STRESS AND STRAINS (σ AND ε). BASED ON THE STRAINS (THE PRIMARY VARIABLES), THE SECONDARY VARIABLES (I.E., THE VOLUMETRIC STRAINS (ε_V) AND TENSILE STRAINS (ε_T)) ARE CALCULATED. USING THESE SECONDARY VARIABLES, THE CONNECTING VARIABLES (I.E., POROSITY (ϕ) AS WELL AS THE SHEARED MATRIX PERMEABILITY AND TENSILE FRACTURE PERMEABILITIES (K_M AND K_F)) ARE CALCULATED AND MAPPED ONTO THE FLUID FLOW GRID. IN THIS WAY, PORE PRESSURES, POROSITY AND PERMEABILITIES ARE EXCHANGED BETWEEN THE MODULES IN THE ITERATIONS. 101
FIG. 5-3: RESULTS OF WELL TESTS IN OIL SANDS IN BURNT LAKE PROJECT (XU, 2010) 103
FIG. 5-4: THE FINITE DIFFERENCE MODEL AND THE BOUNDARY CONDITIONS OF THE GEOMECHANICAL PLANE-STRAIN MODEL..... 105

FIG. 5-5: COHESION, FRICTION AND DILATION ANGLES OF COLD LAKE OIL SAND SAMPLES AS A FUNCTION OF THE EQUIVALENT PLASTIC STRAIN AT LOW AND HIGH EFFECTIVE CONFINING STRESSES 107
FIG. 5-6: SIMULATION RESULTS FOR THE TRIAXIAL COMPRESSION TESTS PERFORMED BY WONG ET AL. (1993). LEFT: THE STRESS-STRAIN PLOTS FOR THE ENTIRE TEST. RIGHT: A TYPICAL SHEAR BAND CAPTURED DURING THE LOWEST EFFECTIVE STRESS TEST. THE UNLOADING AND LOADING CYCLES ARE NEGLECTED. 108
FIG. 5-7: HORNER PLOT OF THE THREE WELL TESTS 109
FIG. 5-8: SCHEMATIC OF VOID AND WATER VOLUME SATURATION DUE TO VOLUMETRIC STRAINING 110
FIG. 5-9: RELATIVE PERMEABILITY CURVE USED IN THE MODEL (KISMAN AND YEUNG, 1995)..... 112
FIG. 5-10: IMPACT OF ABSOLUTE PERMEABILITY ON NUMERICAL RESULTS 113
FIG. 5-11: MESH SIZE EFFECT 114
FIG. 5-12: SIMULATION RESULTS OF THE BASE-CASE MODEL 115
FIG. 5-13: STRESS PATH OF WELL TEST 3 IN THE 3D NUMERICAL ANALYSIS CONDUCTED BY XU (2010) USING THE STRAIN-INDUCED ANISOTROPIC SHEAR PERMEABILITY MODEL (WONG, 2003) 116
FIG. 5-14: STRESS PATH AT THE WELLBORE IN THE SIMULATED WELL TESTS 117
FIG. 5-15: THE FRACTURING RESPONSE OF THE OIL SANDS UPON COLD WATER INJECTION..... 119
FIG. 5-16: STRESS PATH AT THE WELLBORE IN THE SIMULATED HYDRAULIC FRACTURING 120
FIG. 5-17: SHEARED YIELD ZONE DUE TO INJECTION. LEFT: THE SIMULATED WELL TESTS. RIGHT: THE INDUCED HYDRAULIC FRACTURED MODEL 121
FIG. 5-18: THE MESH SIZE IMPACT ON FRACTURE PRESSURE AND LENGTH 122
FIG. 5-19: SENSITIVITY ANALYSIS WITH RESPECT TO THE TENSILE STRENGTH OF OIL SANDS 123
FIG. 5-20: THE IMPACT OF THE MINIMUM PRINCIPAL STRESS MAGNITUDE..... 124
FIG. 5-21: THE IMPACT OF THE MAXIMUM PRINCIPAL STRESS MAGNITUDE 125
FIG. 5-22: THE INFLUENCE OF COHESION ON THE FRACTURING RESPONSE 126
FIG. 5-23: THE IMPACT OF THE ELASTIC MODULUS ON THE FRACTURE LENGTH AND FRACTURING PRESSURE 128
FIG. 5-24: THE EFFECT OF THE RESERVOIR'S ABSOLUTE PERMEABILITY ON THE FRACTURE RESPONSE 128
FIG. 5-25: THE INFLUENCE OF THE SHEAR PERMEABILITY EVOLUTION RATE (B PARAMETER)..... 130
FIG. 5-26: SENSITIVITY ANALYSIS WITH RESPECT TO RAMP-UP TIME..... 131
FIG A-1: PERMEABILITY MEASUREMENT DURING TRIAXIAL TESTS CONDUCTED BY HU ET AL. (2010) 148
FIG. A-2: PERMEABILITY EVOLUTION OF RED SANDSTONE DURING COMPACTION (HU ET AL., 2010) 149

FIG. A-3: VARIATION OF PERMEABILITY RATIO OF RED SANDSTONE DURING COMPACTION (HU ET AL., 2010) 149
FIG. A-4: TOUHIDI-BAGHINI'S MODEL WITH B=0.233 FOR ALL THE EXPERIMENTS DONE BY HU (2010) 150
FIG. B-1: ELASTIC MODULUS OF THE OIL SANDS AS A FUNCTION OF CONFINING STRESS 152
FIG. B-2: FRICTION AND DILATION ANGLE OF COLD LAKE OIL SANDS AS A FUNCTION OF THE EQUIVALENT PLASTIC STRAIN AT LOW AND HIGH EFFECTIVE CONFINING STRESSES 154
FIG. B-3: COHESION OF COLD LAKE OIL SANDS AS A FUNCTION OF THE EQUIVALENT PLASTIC STRAIN AT LOW AND HIGH EFFECTIVE CONFINING STRESSES 154
FIG. B-4: SIMULATION RESULTS FOR THE TRIAXIAL COMPRESSION TESTS PERFORMED BY WONG ET AL. (1993): TOP) THE STRESS-STRAIN PLOTS FOR ALL TESTS, AND BOTTOM) A TYPICAL SHEAR BAND CAPTURED FOR THE LOWEST EFFECTIVE STRESS TEST 155

List of Symbols

a - constant for relating friction factor to Reynolds number

a, b - constants in Wong's shear permeability model

B_v, B_h - shear- permeability enhancement rates in the Touhidi-Baghini model

C - constant representing geometry of the flow

C_r - *real cohesion*

c_k - coefficient for deviation from ideal condition

D - fracture half-aperture, m

dx and dy - size of the control volume

EPS - equivalent plastic strain

E_{stat} - static and dynamic elastic modulus

E_{dyn} - dynamic elastic modulus

f - friction factor

F_{rough} - friction factor counting for deviation from cubic law

g_k - components of the gravity vector, m/s^2

g^p, $g^{p(m)}$, $g^{p(e)}$ - inelastic fracturing strain, superscripts m and e represent material and element, respectively

$HECS$ - high effective confining stress

h - hardening modulus

k, k_0 - new and original permeability, respectively, m^2

k_f - hydraulic conductivity of fracture

k_m - *matrix permeability*

k_x, k_{xy}, k_y and k_i - elements of anisotropic permeability matrix

k_{ij} - mobility coefficient

$l_c^{(m)}$, $l_c^{(e)}$ - material and element characteristic length, respectively, m

L - length of the fracture, m

$LECS$ - low effective confining stress

mod_fac - modification factor

P - second invariant of the deviatoric stress tensor

PM - permeability multiplier

q and q_r - tension limit and tension limit at low effective confining stress, respectively

q_m - mass flow rate

q_i - specific discharge vector

N_{Re} - Reynolds number

PM - permeability multiplier

q_i - specific discharge vector, m/s

Q - flow rate, m^3/s

r_e, r_w - outer and wellbore radius, respectively, m

s_w and s_b - water and bitumen saturations

t - element thickness, m

T - second invariant of the deviatoric stress tensor

u_x and u_x - fluid velocities in x and y directions

V_b - volume of the block

W - thickness of the fracture, m

$\overline{w}_f$ - fracture aperture, m

x_j - components of coordinate system, m

∇ - gradient operator

Δe_m^{ps} - volumetric plastic shear strain increment

Δe_j^{ps} - principal plastic shear strain increments

β_c - conversion factor

ε - height of asperities, m

$\varepsilon_1, \varepsilon_3$ - principal strains

ε_T - tensile strain

ε_v - volumetric strain

ε^p - accumulated plastic shear strain

Φ - hydraulic head

ϕ and ϕ_0 - porosity of the porous media. Subscribt "o" denotes the initial value.

ϕ_a and ϕ_r - friction angle and friction angle at low effective confining stress, respectively

μ and $\mu_{\sigma r}$ - friction coeficient and friction coeficient at LECS

μ - fluid dynamic viscosity, Pa.s

μ_f - fluid viscosity

ρ - mass density of the fluid, kg/m^3

σ_r' and σ_z' - effective radial and axial stress, respectively.

σ_T - tensile strength

σ_e - equivalent stress

σ_e^0 - initial equivalent stress

τ_w - wall shear stress, Pa

υ - fluid kinematic velocity, m^2/s

v - iteration number

An invasion of armies can be resisted; an invasion of ideas cannot be resisted.

Victor Hugo, The History of a Crime (Translation by T.H. Joyce and A. Locker)

Chapter 1: Introduction

Hydraulic fracturing generally refers to a process in which hydraulic pressure initiates and propagates a fracture in the ground (Adachi et al., 2007). Hydraulic fracturing is a tool to enhance hydrocarbon production by inducing fracture(s) in reservoir rock. A hydraulic fracture is induced by injecting fluid into a reservoir rock at pressures higher than fracture initiation pressure. The fracture(s) geometry (size, orientation, etc), mode (shear/tensile), initiation and propagation pressure and other characteristics may vary depending on the geomechanical conditions such as in situ stresses and the rock's physical properties.

Hydraulic fracturing was first used in the Houston gas field in western Kansas in 1947 (Howard and Fast, 1970) and has been successfully used for stimulation purposes to improve oil recovery. Hydraulic fracturing has been the stimulation method for more than 85 percent of gas wells and 60 percent of all oil wells in North America. This ratio is rising (Economides et al., 2002).

In addition to well productivity enhancements, hydraulic fracturing has been implemented in a variety of other unrelated applications, including carbon sequestration (Reynolds and Buendia, 2017), in situ stress measurement (Hannan and Nzekwu, 1992), enhanced geothermal energy (Kumar et al., 2015), solid waste injection (Dusseault et al., 1998), groundwater remediation (Adams and Rowe, 2013), preconditioning in block cave mining (He et al., 2015), rock burst mitigation (Zhao et al., 2012), water well development (Adams and Rowe, 2013), and biosolid injection (Xia et al., 2007). The hydraulic fracturing process in weak rocks results in significant changes in rock strength and stiffness, porosity and permeability, and ground stresses, which are the parameters that largely influence the fracture response of the formation. Intricate relationships between these

parameters render the conventional fracture analysis methods insufficient to predict the fracturing process, particularly in weak sandstones. Hence, it is necessary to develop a proper modeling tool which incorporates these parameters.

Originally, hydraulic fracturing was employed to stimulate hard-rock reservoirs, which typically behaved like a brittle linear-elastic material. These reservoirs were mostly impermeable or exhibited low permeability (Xu, 2010). Recently, there has been interest in stimulating unconsolidated and poorly consolidated formations where the material possesses low shear strength and higher permeability (Khodaverdian et al., 2010). Here the assumptions of linear-elastic fracture mechanics and small fluid leak-off from fracture walls may not be valid.

Researchers have found that the mode of failure during hydraulic fracturing of weakly consolidated sandstone is influenced by material properties such as dilative behavior, strength, porosity and permeability, injection pressure ramp-up rate, injection rate, in situ stresses, injection fluid properties, and possible solid concentrations in the injection fluid (Golovin et al., 2010). Moreover, wellbore orientation and completion type (e.g., number and direction of perforations) can affect the fracture geometry and propagation pattern (Daneshy, 2003, 2011). As a result, a complex fractured zone rather than a simple planar fracture may develop in weakly consolidated sandstones (Daneshy, 2003, 2011).

Laboratory experiments have shown that hydraulic fracturing of weakly/unconsolidated sandstone could be in the form of shear failure/fracture, tensile fracture or a combination of these two modes (Daneshy, 2003). The hydraulic conductivity of a tensile fracture is a nonlinear function of the fracture width (Zimmerman and Bodvarsson, 1996; Waite et al., 1999; White, 2011). In shear failure, the permeability enhances due to dilation and formation of shear bands (Touhidi-Baghini, 1998). The shear dilation increases the local stresses and, consequently, increases the fracturing pressure (Pak, 1997). Due to the low strength of weakly consolidated sandstones, shear failure/fracturing of the reservoir rock during injection is likely and has been related to phenomena such

as multiple fracturing and fracture branching in field operations (Daneshy, 2003), which are generally neglected in numerical hydraulic fracture numerical models.

Most of the current continuum-based numerical models require a predetermined hydraulic fracture direction (e.g., Ji (2008)). Even though some recent continuum models have been adopted to capture fractures in general directions (e.g., Xu (2010)), they lack a proper tensile fracture-flow law, or do not simulate the development of shear bands and their interactions with tensile fractures. Models have been developed by utilizing discontinuum mechanics in the form of the Discrete Element Method (DEM) and other methods. These models are computationally costly and impractical for large-scale field problems.

1.1 Motivation

Most current hydraulic fracture models, particularly those that are based on the discrete fracture approach, assume a two-wing planar fracture that is believed to occur in competent rocks. Laboratory tests indicate that weakly consolidated sand formations are prone to shear failure/fracturing around water injection wells, resulting in shear dilation; hence, higher permeability and higher compressive stresses around the wellbore. The shear failure process may lead to the formation of a fracture network instead of a planar tensile fracture commonly observed in hard rocks. According to the literature (which will be reviewed in Chapter 2), the assumption of a two-wing tensile fracture with a well-defined fracture direction may not be an appropriate justification to simulate hydraulic fracturing in weakly consolidated sandstone formations. Therefore, new modeling approaches need to be developed.

Smeared fracture modeling techniques are found to be more suitable than the discrete fracture modeling technique for hydraulic fracturing simulation in unconsolidated and weakly consolidated sandstones. However, there are limitations to some aspects of existing smeared fracturing models for hydraulic fracturing. They either do not distinguish between the flow conductivity of a shear failure/fracture and a tensile fracture (Xu, 2010) or they assign a constant permeability to the tensile fracture which is not a function of the fracture aperture

(Zhai, 2006). However, the physics of fluid flow in tensile and shear fractures is different. Fluid flow in a tensile fracture can be considered as flow through an open space whereas flow in shear fractures (or failure zone) should be considered as flow through crushed materials. For a tensile fracture, fluid flow can be modeled by using the parallel plate theory. In such cases, the fracture hydraulic conductivity is a function of the fracture's aperture. However, in a shear failure/fracture, the permeability of the crushed rock in the fracture band is a function of the fabric alteration and the dilative deformation of the shear bands. In existing smeared fracture models, shear fractures are only simulated as diffused shear failure zones.

In the current research, a literature review was carried out to study the results of small- and large-scale laboratory experiments on unconsolidated and weakly consolidated sandstones. Next, field-fracturing data in the literature were collected to investigate the fracturing response of weak sandstone reservoirs. A combination of the field and laboratory data assessments provided some insights on the possible fracture modes and patterns in weak sandstones.

A literature survey was also carried out on the existing numerical modeling tools used to simulate hydraulic fracturing in weakly consolidated sandstones. Various features of the numerical tools were evaluated, particularly those related to the prediction of the fracture direction, fracture modes, and the permeability variation of the rock matrix due to shear and tensile fracturing.

In this research, a pseudo three-dimensional numerical tool has been developed to simulate hydraulic fracturing in weakly consolidated sandstones. The model is capable of simulating the possible failure modes and fracture rotation around injection wellbores. A smeared fracture approach was implemented and utilized based on the continuum mechanics assumption.

1.2 Problem statement

A significant amount of research has been directed towards understanding the hydraulic fracturing mechanism in weakly consolidated sandstone. These studies

cover a wide range of materials, stresses and injecting fluids. There are, however, aspects of the hydraulic fracturing process that remain unresolved for weakly consolidated sandstones. These issues include fracture modes and geometries for weak sandstones; and higher-than-expected fracture pressure in some field projects, which are underestimated by the numerical models.

Shear and tensile failures/fractures are believed to be the two possible failure/fracture modes for hydraulic fracturing in weakly consolidated sandstones. The fracturing pattern in a reservoir is believed to be influenced by the formation of shear bands in the process zone ahead of the fracture, on the fracture walls, and elsewhere in the reservoir. Shear band development may precede tensile fracturing in weak sandstones. Further, it is believed that shear and tensile fractures interact with each other, resulting in un-planar (off-balance) fracture development in weakly consolidated sandstones. The development of shear bands and the concomitant shear dilation may result in stress alterations in the reservoir, requiring higher injection pressures to induce tensile fractures. Further, pressure redistribution in the medium can result in stress increases which can create conditions in which a tensile fracture may not be induced under the operating conditions. This can lead to the development of only a shear-fractured zone around the wellbore.

A hydraulic fracture model is needed in which the conductivity of a tensile fracture is calculated according to governing fracture flow rules (e.g., cubic law) and the direction of a tensile fracture is not predetermined. Also, the potential transformation of a shear fracture to a tensile fracture and potential re-orientation of a tensile fracture due to shear banding at the fracture tip has not been addressed in the literature.

1.3 Research objective

The primary objective of this research is to develop a numerical tool to study the failure modes and pattern and the variation of fracturing pressure during field-scale hydraulic fracturing of weakly consolidated sandstones. A smeared fracture approach will be used to develop a numerical tool capable of simulating shear and

tensile fractures (the latter without a prescribed direction). This research will enhance the understanding of the mechanisms involved in the process of hydraulic fracturing in weakly consolidated sandstones. The main questions to be answered in this research are:

- Why do some reservoirs require large fracturing pressure?
- What factors play a role in increasing the fracturing pressure?

This research will provide valuable information in guiding fracturing practices in field operations, for optimization and management of fracturing projects.

1.4 Research methodology

The methodology in this research consists of developing a pseudo-3D continuum-based numerical hydraulic fracture model capable of capturing both shear and tensile fracturing processes. A finite difference software, FLAC (ITASCA Consulting Group, 2006), was used to carry out the stress/strain analysis. A single-phase finite difference fluid flow analysis code was developed and linked to the geomechanical model using an iterative coupling scheme.

A Mohr-Coulomb plasticity model with tension cut-off was used in this research to simulate the shear failure in the reservoir. Fracture mechanics criteria such as linear elastic fracture mechanics (LEFM) (stress intensity factor or energy release rate) were not used as they are deemed inappropriate for weakly consolidated sandstones due to the large shear failure zone at the tensile fracture face and tip during the injection (Khodaverdian and McElfresh, 2000; McElfresh et al., 2002; Di Lullo et al., 2004; Bohloli and de Pater, 2006; Huang et al., 2011).

The fracture energy regularization method (Crook et al., 2003) was used to reduce the mesh-size dependency in the simulation of the shear failure and tensile fractures. The mesh-size dependency in assigning the equivalent permeability to tensile fractured elements was also considered.

For tensile fractures detected in an element considered to be a hydraulic fracture in the developed model, the fractures must be continuously connected to

the injection point (wellbore). If this criterion is satisfied, the fracture flow scheme is activated and simulated in the numerical model in accordance with fracture flow laws. Tensile fractures of isolated elements in the reservoir (elements not connected to the wellbore) were not considered as hydraulic fractures as fracture flow cannot be established in cracks that are not connected to the injection point. An algorithm was implemented in the numerical model to recognize connected tensile hydraulic fractures in the model and distinguish them from isolated tensile cracks (failures or fractures).

1.5 Thesis layout

The research is presented in six chapters.

Chapter 1 (the current chapter) provides the background and the scope of the research.

Chapter 2 presents a literature review of hydraulic fracturing with emphasis on hydraulic fracturing in weak sandstones.

In Chapter 3, a permeability tensor model for tensile fractures is used to relate the permeability of an element, which is fractured in tension, to its deformation. The permeability tensor includes permeabilities in the directions parallel and perpendicular to the fracture. The smeared fracture approach makes it possible to predict a tensile fracture's direction based on the numerical model's solution instead of prescribing the fracture direction in advance. The difficulty in simulating tensile fracture in a continuum model is how to relate the element deformation to its permeability such that it results in accurate tensile fracture conductivity. A procedure for the permeability calculations is presented in this chapter and the results are validated against available data in the literature.

Chapter 4 describes the calculation of the permeability in the elements that fail in shear. The existing shear permeability models are described, their limitations and advantages are discussed, and a proper criterion is selected to calculate shear-enhanced permeability to further develop the hydraulic fracture model. The chapter also includes the results of the model validation including

both shear and tensile fracture criteria against a large-scale laboratory hydraulic fracturing experiment.

In Chapter 5, the coupled model is used to simulate a series of well tests in oil sands. The chapter presents the numerical study used to assess the fracturing pressures of the reservoir in a sensitivity analysis with respect to the flow and geomechanical parameters of the formation. These parameters include, among others, the minimum and maximum principal stress, apparent tensile strength and cohesion of the oil sands, and absolute permeability.

Chapter 6 summarizes the current research and presents the major findings from this work. It also includes suggestions to further develop the model.

1.6 Significance of the work

Hydraulic fracturing has been the stimulation method for more than 85 percent of the gas wells and 60 percent of all oil wells in North America and the ratio is still rising (Economides et al., 2002). Investment in hydraulic fracturing has grown from $2 billion to almost $15 billion in the last decade (Marongiu-Porcu et al., 2010) and has become the petroleum industry's second largest outlay after drilling (Economides and Wang, 2010). This technique has become a standard practice to develop tight gas, shale gas and coal bed methane formations and is still popular in oil-bearing formations in all permeability ranges (Economides and Wang, 2010).

The model developed in this research will greatly increase the understanding of the mechanisms involved in hydraulic fracturing of weakly consolidated sandstones, including fracture modes and patterns. Such improved understanding can help to manage and optimize fracturing jobs. Understanding the failure mode of hydraulic fracturing in weak or unconsolidated sandstones is important in the optimum design of fracturing jobs and to avoid inadvertent fractures in reservoir or its caprock.

Chapter 2: Literature Review

2.1 Introduction

This chapter presents a literature review on fracture mechanisms and numerical hydraulic fracture models. Fracture mechanisms involved in hydraulic fracturing of unconsolidated and weakly consolidated sandstones were studied by reviewing publications on laboratory research and field fracturing observations. Numerical hydraulic fracture models are also reviewed with an emphasis on their capability in simulating fracturing mechanisms in weak sandstone reservoirs.

2.2 Definition of failure versus fracture

The literature on the material behavior presents different definitions for failure. Bieniawski et al. (1969) defined failure as a change in the state of behavior of a material. Examples are fracturing (new cracks form or existing cracks are extended) and rupture (the structure disintegrates into two or more pieces). Goodman (1989) described failure as the total loss of integrity of a rock sample, and Bésuelle et al (2000) related failure to the formation of a shear band accompanied with the sample's strain-softening response.

Failure (material behavior) refers to the peak strength and post-peak behavior of the material where the material becomes unable to bear additional stress and its permeability starts to change significantly. Following the peak-strength state, micro-cracks join and form macro-cracks or a fracture (shear or tensile band) resulting in the loss of strength (strain softening/ fracturing). This fracture forms a highly permeable zone for fluid flow, which enhances the permeability of the matter.

As failure (softening) progresses, the material totally loses its strength (or, in the case of unconsolidated and weakly consolidated geomaterial, its cohesion) and disintegrates. This thesis refers to this state as fracturing. Shear fracture in this

research refers to residual strength where a fracture has fully formed. Shear permeability of the material starts to evolve during the softening (failure) stage and is enhanced to the end of the fracturing stage.

In addition to considering the material behavior, it is necessary to consider geometric constraints when distinguishing failure from fracture. Geometric constraints in this research refer to the numerical model mesh size effect. A large mesh size may lead to a diffused failure zone while strain localization and shear banding are expected according to observations (a clear example will be illustrated in Chapter 4 of this thesis). In this research, shearing is simulated in a diffused form since the mesh size is not fine enough to capture localization of strain. For this reason, all the diffused shear zones in the numerical results are referred to as shear failure, independent of the nature of the material behavior (i.e., failure or fracture). Failure is more spread and diffused in the material while fracture is more discrete and localized.

2.3 Fracture geometry

In hydraulic fracturing of competent impermeable rocks, a clear tensile fracture may develop in the direction normal to the minimum principal stress. In weak and unconsolidated sandstones, a tensile planar fracture may occur only when the injection rate is greater than the rate of fluid leak-off from the fracture into the formation. This usually happens when the pumping rate is high, or the rock permeability is low, or the injecting fluid is very viscous or contains solid particles that build up skin (Pak, 1997; Khodaverdian and McElfresh, 2000; de Pater and Dong, 2007; Golovin et al., 2010; Khodaverdian et al., 2010). At the other extreme, shearing can be the predominant fracturing mode in weak rocks when the leak-off is large due to high permeability (Pak, 1997; Khodaverdian and McElfresh, 2000; Khodaverdian et al., 2010). A transition exists where both shear and tensile modes of failure may occur simultaneously (Pak, 1997; Khodaverdian and McElfresh, 2000; Khodaverdian et al., 2010).

2.4 Fracturing mechanisms

The fracturing mechanism in a rock may consist only of a single mode or a combination of three modes: opening mode, sliding mode and tearing mode, as shown in Fig. 2-1 (Daneshy, 2003). A tensile fracture is created by tensile stress and the main resistance comes from the minimum in situ stress and the tensile strength of the material. In this process, the fracture width is the result of the compression of the material surrounding the fracture walls. Larger amounts of net pressure (NFP1) make the fracture wider. The width is proportional to the fracture length and height (Daneshy, 2003).

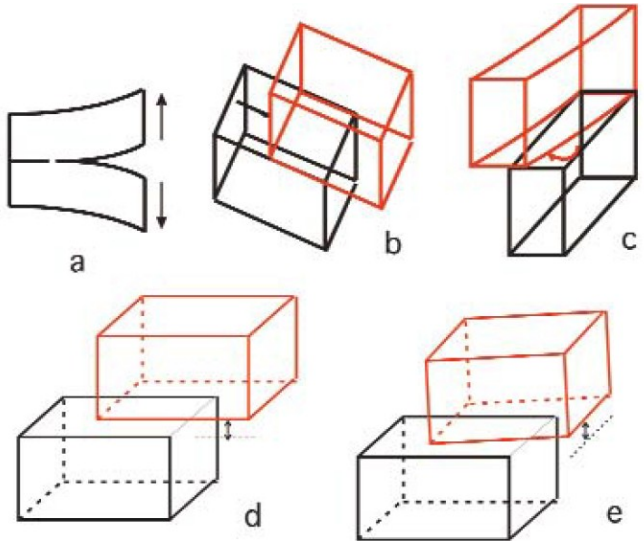

Fig. 2-1: Fracturing modes: a) Tensile mode, b) shear mode, c) tearing mode, d and e) combination of modes (Daneshy, 2003)

Shear failure/fracture occurs when shear stress along a plane exceeds the shear strength of the material on that plane. In this process, two surfaces of the fracture slide over each other in opposite directions but there is no separation between them. This type of fracture does not reverse as easily as the tensile mode because it requires the two walls to slide back. Tearing mode of fracturing occurs due to tearing action in which two faces twist away from each other but no gap forms between them (Daneshy, 2003).

[1] Net fracturing pressure is defined as the difference between the minimum in situ stress and the fracturing pressure

By combining tensile and shear forces, a tensile-shear fracture may take place. In this case, the fracture results in a gap with lateral displacement (Daneshy, 2003) as illustrated in Fig. 2-1 d and e. It is likely that during hydraulic fracturing of weakly consolidated sandstones, shearing occurs at the initial stages of injection due to the material's low shear strength.

Many researchers have performed theoretical and experimental investigations of the initiation and subsequent propagation of tensile fractures. (Hagoort et al., 1980; Settari, 1980; Nghiem et al., 1984; Papanastasiou, 1997b; van Dam et al., 2000; Wu, 2006; Ji, 2008). These studies have been driven by the assumption that a two-wing planar fracture is parallel to minimum principal stress. This assumption, however, may not result in realistic outcomes or may even yield misleading results (Di Lullo et al., 2004) when shear fracturing takes place (Di Lullo et al., 2004; Bohloli and de Pater, 2006; Huang et al., 2011).

2.4.1 Fracturing mechanisms in laboratory experiments

This section reviews the literature on small- and large-scale laboratory hydraulic fracturing experiments conducted to investigate possible fracturing modes during injection into weak sandstones.

2.4.1.1 Tensile fracturing mode

A tensile hydraulic fracture naturally aligns itself according to the direction of in situ stresses, as shown in Fig. 2-2. The fracture plane propagates in the direction normal to the minimum in situ stress since this direction requires the least energy for propagation.

Tensile fractures observed in hydraulic fracturing experiments have been reported extensively in the literature (van Dam et al., 2000; Cook et al., 2004; de Pater and Dong, 2007; Golovin et al., 2010; Zhou et al., 2010). Tensile fracture occurs in a single plane (two-wing planar fracture) and grows in an orderly manner, and its trend is predictable. As more fluid is injected, the fracture grows and becomes longer in its original plane (Daneshy, 2003). This type of fracture is particularly seen where the leak-off is small (impermeable rock, high viscosity fluid or efficient external filter cake). Tensile fracture due to the formation of a

filter cake is known as a formation-damage-driven fracture (Khodaverdian et al., 2010).

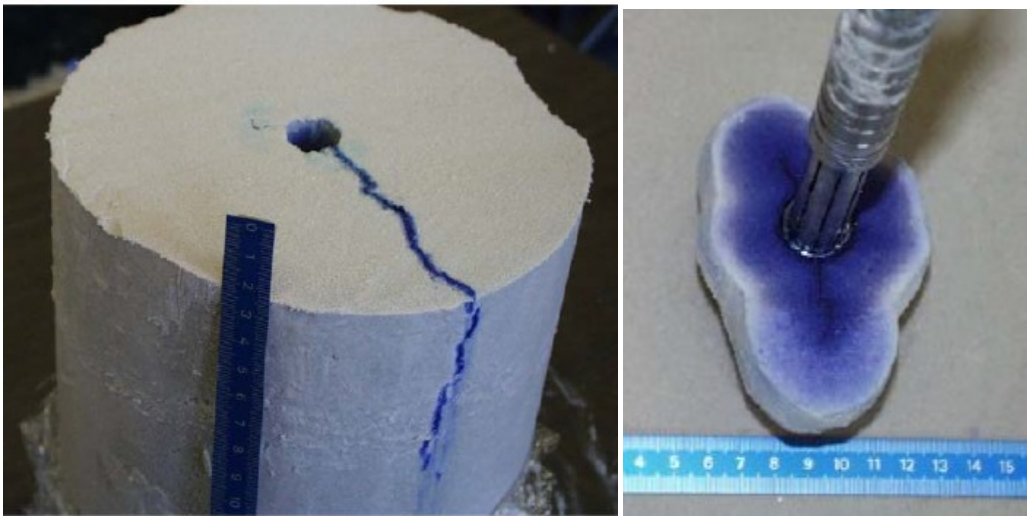

Fig. 2-2: Dominant tensile mode of fracturing during hydraulic fracturing (Bohloli and de Pater, 2006)

2.4.1.2 Shear fracturing mode

Shear fracture during injection is known as mobility-driven fracture (Khodaverdian et al., 2010). Material properties, stress level, fluid rheology, solid concentration, permeability and pore pressure are the most important parameters affecting shear fracturing (Bohloli and de Pater, 2006).

Shear fracture usually consists of multiple bands, channeling and out-of-plane propagation (see Fig. 2-3) as observed in hydraulic fracturing experiments (Pak, 1997; Khodaverdian and McElfresh, 2000; Chang, 2004; Bohloli and de Pater, 2006; de Pater and Dong, 2007; Golovin et al., 2010; Jasarevic et al., 2010; Khodaverdian et al., 2010; Zhou et al., 2010; Olson et al., 2011). Injection fluids in hydraulic fracturing operations cover a wide range of low-to-high viscosity with no-to-high concentration of solid particles with different injection rates and confining stresses. In these observations, shear failure could be the dominant mechanism or part of a mixed mode of fracturing, for instance, a process zone exists ahead of the tensile fracture tip, and a large concentration of shear stress in that zone (Papanastasiou, 1997b; Wu, 2006), as illustrated in Fig. 2-4.

Sometimes shear failure/fracturing is the only dominating mechanism (Pak, 1997; Khodaverdian and McElfresh, 2000) in weak sandstones. Shear fractures are more likely to occur in highly permeable rocks with no-or-small skin at the fracture wall (high leak-off) (Zhai and Sharma, 2005; Zhai, 2006; de Pater and Dong, 2007; Khodaverdian et al., 2010). The development of shear bands is a major reason that permeability is enhanced in the formation rock (Wong, 2003; Zhai and Sharma, 2005; Khodaverdian et al., 2010; Zhou et al., 2010).

.

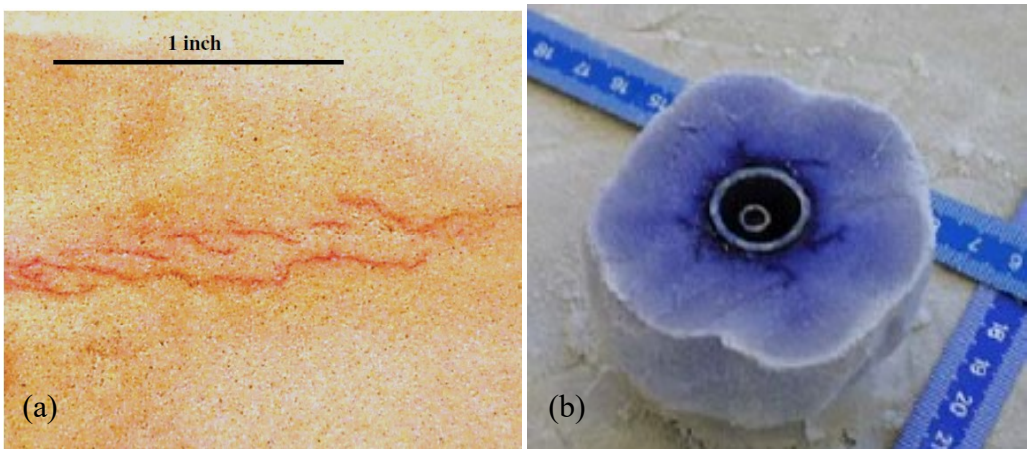

Fig. 2-3: Shear failure and branching during hydraulic fracturing, a) shear and subparallel fractures during cross link gel injection with 35 lb/Mgal polymer loading (Khodaverdian and McElfresh, 2000), and b) shear failure during injection of bentonite slurry with concentration of 150 g/l (Bohloli and de Pater, 2006)

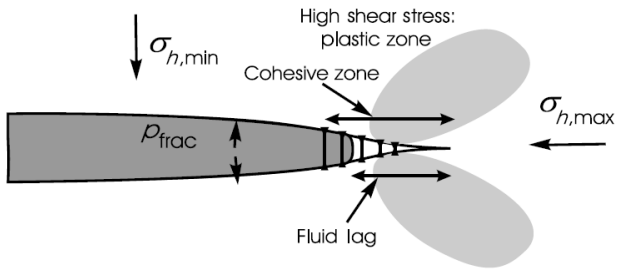

Fig. 2-4: Shear stress concentration in the process zone ahead of the fracture tip (van Dam et al., 2000)

2.4.1.3 Mixed mode

Shear fractures may open under fluid pressure (mixed mode - shear prior to tensile fracture) and fluid can flow inside the fracture as shown in Fig. 2-3b. In

this case, the shear fracture creates a conduit for fluid flow, which may allow the fluid pressure to exert force on the shear fracture wall and convert the shear fracture to a tensile fracture.

Further, shear failure may occur at the tensile fracture faces. Such a fracture is known as a mobility-driven fracture (Khodaverdian et al., 2010). Fig. 2-5a schematically demonstrates the fracture zone which consists of the main fracture and several sub-parallel fractures and branches. The development of an efficient filter cake on the fracture wall can significantly reduce the shear failure at the tensile fracture walls, resulting in damage-driven fractures as shown in Fig. 2-5b.

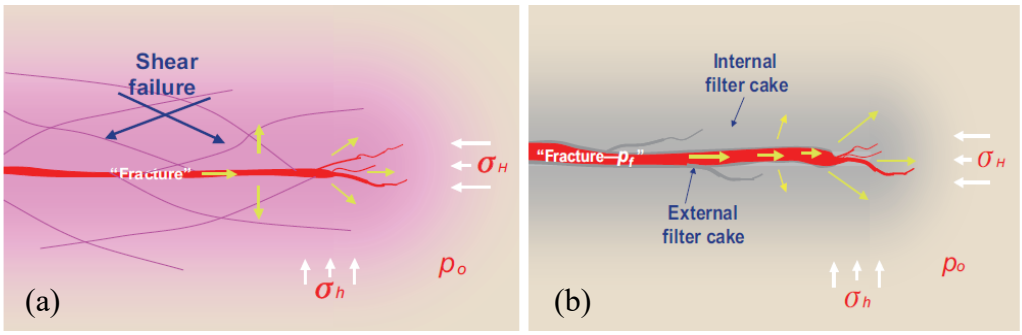

Fig. 2-5: Schematic of possible mechanisms of fracture tip propagation: a) mobility driven shear and tensile fractures, and b) a formation-damage-driven fracture (Khodaverdian et al., 2010)

Shear failure during hydraulic fracturing may increase the net fracturing pressure (Pak, 1997; Khodaverdian and McElfresh, 2000; Khodaverdian et al., 2010). These shear fractures may reduce the length of the main fracture and cause premature tip screen-out during fracpacking (Khodaverdian and McElfresh, 2000). In contrast, they can increase the capacity of the rock for slurry and waste injection (Cook et al., 2004).

2.4.2 Field observations of failure modes in hydraulic fracturing

Data collected from recovered cores, minebacks, microseismicity, overcores and borehole video, fracturing pressure response and surface tilts (Tiltmeter mapping) in sandstones, jointed granites and shales as well as laboratory tests indicate that hydraulic fractures may not always be planar single two-wing fractures as conventionally thought. There is a need for a new perspective

including a potential for multiple far-field fracture occurrence that should replace the old view of a single planar fracture (Mahrer et al., 1996).

Some field observations cannot be explained by classical models (Settari, 1988; Weijers et al., 2000; Daneshy, 2003; Onaisi et al., 2011). The dimensions of field fractures are usually much smaller (Settari, 1988; Weijers et al., 2000; Daneshy, 2003, 2005) and their widths are much larger than predicted by the conventional models (Settari, 1988; Daneshy, 2003), which can be attributed to the plastic deformation of the material surrounding the fracture. The actual fracture aperture may also be narrower than predicted (Weijers et al., 2000; Daneshy, 2005) due to the possible formation of multiple fractures and branches. Neither a larger volume of fluid nor more proppants guarantee that a longer fracture can be induced (Daneshy, 2003).

The literature also indicates higher measured fracturing pressures than the model calculations (Settari, 1988; Leshchyshyn et al., 1996; Weijers et al., 2000; Daneshy, 2003; Palmer et al., 2007; Osorio and Lopez, 2009). The Delft Fracturing Consortium worldwide survey on fracturing pressures indicated that net pressures encountered in the field are commonly 50% to 100% higher than their corresponding values predicted by conventional fracturing simulators based on linear fracture mechanics (de Pater, 1996) cited by Papanastasiou, (1997b)).

2.4.2.1 Off-Balance Fracture Growth

Daneshy (2003) introduced the new concept of off-balance growth in hydraulic fracturing. A tensile planar fracture whose growth pattern is predictable is called “balanced.” The fracturing mode in an off-balance fracture is not solely Mode I and the fracture is not planar anymore; instead it is in a mixed mode and a multi-branch geometry. This fracture growth pattern is called “off-balance growth”. Most hydraulic fractures in weak rocks occur in an off-balance pattern (Daneshy, 2003, 2005).

Branching and shear fracturing are responsible for off-balance growth and the result is shorter and narrower fractures than what have been designed (Daneshy, 2003, 2005). The narrow width causes a larger pressure drop along the fracture.

Also, fluid and proppant movement follows this off-balance pattern. Depending on their width, these shear fractures can open and intake proppants or prevent proppant placement (Daneshy, 2005).

2.4.2.2 Types of Off-Balance Fractures

According to Daneshi (2003), two distinct fracture characteristics are involved in off-balance growth: multiple fracturing and fracture branching.

Multiple fracturing is a near-wellbore phenomenon referring to separate fractures created at the wellbore (Daneshi, 2003). This phenomenon has also been observed in laboratory experiments when the two stresses perpendicular to the wellbore axis are equal (Cook et al., 2004). This near-wellbore phenomenon, which is also known as tortuosity, is responsible for premature screen-out and/or low proppant concentration (Cleary et al., 1993; Aud et al., 1994).

Multiple fracturing is dependent on the well completion design (e.g., borehole inclination; and number, size and distribution of the perforation). Additional important parameters in the development of multiple fractures include fluid pressure inside the wellbore, and wellbore inclination (Daneshy, 2003). Further details follow.

- **Injection rate:** Higher injection rates result in quick pressure increases while leak-off is still small. Large diameter perforation and shorter perforated intervals provide more flow rate to a specific part of the reservoir, increasing the probability of tensile fracture. Some researchers recommend high-rate injection to reduce the intensity of near-wellbore tortuosity (Cleary et al., 1993; Weijers et al., 2000).
- **Length of perforation interval:** Multiple fracturing is less likely when the perforated interval is shorter (Cleary et al., 1993; Aud et al., 1994; Abass et al., 1996; Weijers et al., 2000; Daneshy, 2003).
- **Perforation diameter and direction:** Perforating perpendicular to the direction of the minimum in situ principal stress can reduce the intensity of multiple fracturing (Daneshy, 2003). So can a larger perforation diameter

(Cleary et al., 1993; Aud et al., 1994; Weijers et al., 2000), by providing more flow rate to a specific interval.

- **Fluid viscosity:** High viscosity fluids can also reduce multiple fracturing (Cleary et al., 1993; Aud et al., 1994; Leshchyshyn et al., 1996; Weijers et al., 2000). Armirola et al. (2011) found that fluid leak-off in hydraulic fracturing controls the fracture geometry. High-viscosity fluids create larger fracture width due to the low leak-off. In addition, shear fracturing is less likely to occur when more viscous fracturing fluids are used (Armirola et al., 2011).
- **Borehole orientation:** This parameter can affect multiple fracturing (Cleary et al., 1993; Osorio and Lopez, 2009; Onaisi et al., 2011) due to stress rotation. The most impact is when fracturing a horizontal wellbore in a reservoir where the minimum in situ stress is parallel to the wellbore axis (Abass et al., 1996; Osorio and Lopez, 2009).
- **Stress anisotropy:** The material stress state is closer to the shear failure envelope when the stress difference is larger (i.e., shear failure is more probable) (de Pater and Dong, 2007; Golovin et al., 2010). Osorio and Lopez (2009) reported different results in their laboratory experiments as a greater difference between in situ stresses increased the probability of tensile fracturing.

Fracture branching is another type of off-balance fracture growth. Each fracture branch can have its own sub-branches (Daneshy, 2003).

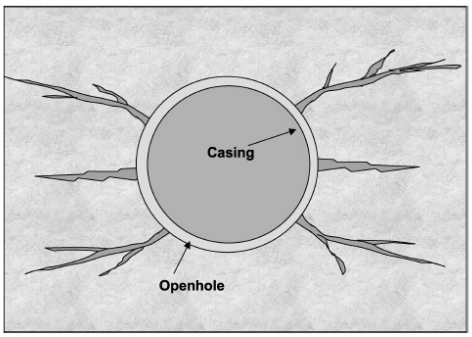

Fig. 2-6: Multiple Fracturing, a near wellebore phenomena (Daneshy, 2005)

Higher net fracturing pressure can be a sign of multiple fracturing and shearing (Leshchyshyn et al., 1996; Weijers et al., 2000; Osorio and Lopez,

2009), even in fracturing low permeability rocks such as shale (Palmer et al., 2007).

2.4.3 Summary of Field Observations

The results of laboratory experiments are consistent with most field observations. The major common conclusions are that both tensile and shear fracturing may occur during hydraulic fracturing. Shear-enhanced permeability is possible and higher fracturing pressure may be expected when weak and unconsolidated sandstones are fractured. Fluid type and injection rate, as well as wellbore completion and deviation, are the parameters that can be selected in such a way to reduce fracturing pressure.

An ideal numerical hydraulic fracture model should be equipped with enough physics to capture the potential fracturing modes and their interaction as well as multiple fracturing/branching and the possible fracture reorientation around a wellbore.

2.5 Parameters that affect the hydraulic fracturing response

The following parameters are believed to influence the fracturing response of weakly consolidated sandstones.

2.5.1 Stress-dependent elastic properties

Laboratory experiments on weakly consolidated sandstones indicate that the sandstones' elastic modulus strongly depends on the effective confining stress. Fig. 2-7 demonstrates such dependence for Salt Wash Sandstone. Increased pore pressure reduces effective stresses, leading to a lower elastic modulus. Further, tensile fracturing reduces the effective confining stress around the fracture, resulting in low elastic moduli in the near-fracture zone.

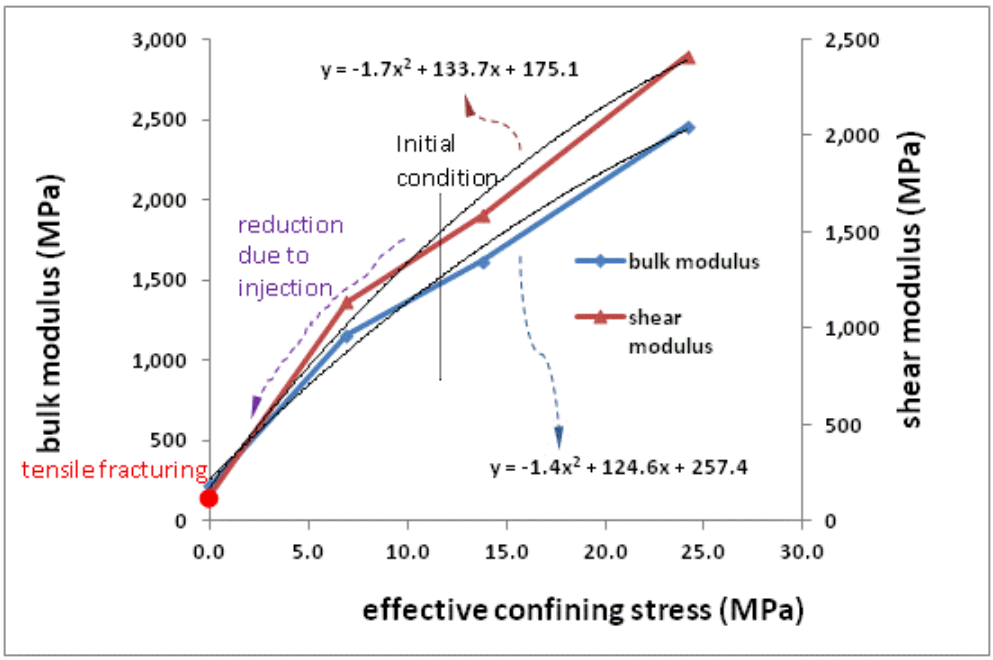

Fig. 2-7: Variation of elastic modulus with effective confining stress (Rahmati et al., 2012; Rahmati, 2013)

2.5.2 Rock Strength

Stronger rocks are less prone to shear failure during injection. The higher the cohesion, the higher the likelihood of tensile fracturing preceding shear fracturing (Rahmati, 2013).

2.5.3 Dilation

Shear failure of weakly consolidated sandstones results in shear dilation, hence, increased permeability and faster pore pressure diffusion. This, in turn, increases the likelihood of additional shear failure. Further, dilation enhances in situ stresses (Pak, 1997) increasing the tensile fracturing pressure.

2.5.4 Permeability

Rock permeability is important because it influences pore pressure diffusion in the matrix, leading to the shear failure that, in turn, may result in higher net fracturing pressure. In weakly consolidated and unconsolidated sandstones, shearing results in dilative shear deformation, which leads to greater local stresses and higher fracturing pressure.

Pak (1997) presented a qualitative chart for the expected hydraulic fracture pattern in a wide range of geomaterials. This chart relates the fracture pattern to the permeability and cohesion of geomaterials (Fig. 2-1). According to the chart, a dominant planar fracture is expected in low permeability rocks with high cohesion, while multiple fractures are likely to occur in permeable sandstones with lower cohesion. In highly permeable rock with high cohesion, a rough and irregular fracture plane is expected, while for highly permeable rock with low cohesion, a zone of tiny inter-connected cracks is anticipated.

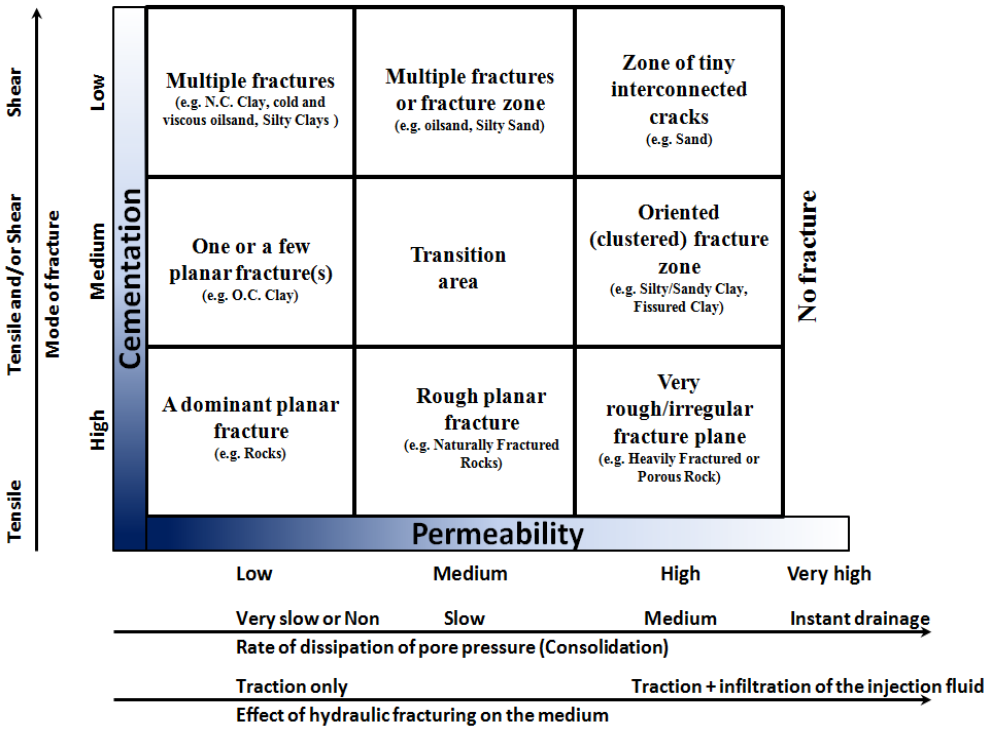

Fig. 2-8: Hydraulic fracturing mechanism of different geomaterials (Pak, 1997)

2.5.5 Fluid Viscosity

Higher fluid viscosity reduces leak-off and results in a smaller poroelasticity effect, less permeability enhancement, and lower net fracturing pressure (Khodaverdian and McElfresh, 2000). It also reduces the possibility of shear failure. A viscous fluid may be injected into a highly permeable material and induce shear fracture while a less viscous fluid may be injected into a very low-preamble material and result in tensile fracture. Therefore, the material's

hydraulic conductivity to the injecting fluid should be considered a determining factor in the mode of fracture.

2.5.6 Stress Magnitude and Direction

The tendency to shear failure increases when the difference between the minimum and maximum principal stresses is higher (de Pater and Dong, 2007; Golovin et al., 2010). Fig. 2-9 illustrates the stress paths of a material with two different initial conditions. As can be seen, higher maximum principal stresses at Point A would lead to shear failure while the same stress path starting at Point B would result in a tensile fracture. Based on their laboratory experiments, however, Osorio and Lopez (2009) reported a higher potential of tensile fracturing for those cases with a greater difference between the principal in situ stresses.

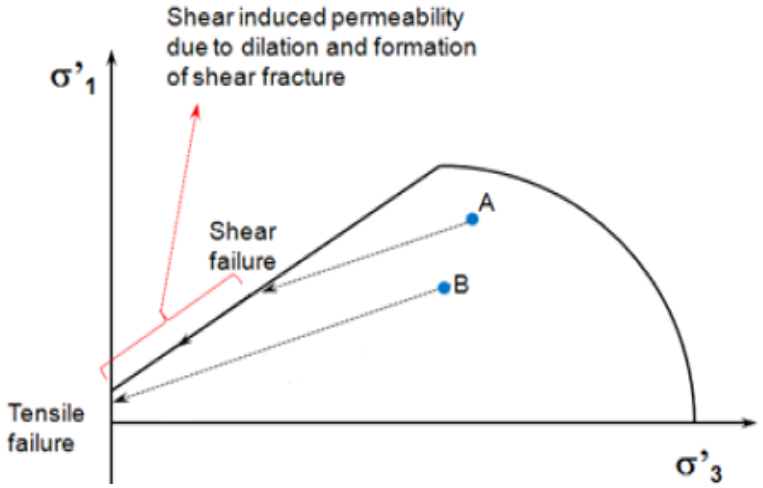

Fig. 2-9: Effect of initial stress state on the failure mode

Cook et al. (2004) reported the results of laboratory-numerical research on injecting drill cuttings (slurry with viscosity of 50 cp) into Berea sandstone blocks under true triaxial testing conditions. The samples were rectangular (7.6 by 7.6 by 16.5 cm) with a 0.6 cm well in the centre. The experiments showed multiple fractures for equal principal stresses. A distinct fracture, parallel to the direction of maximum horizontal stress, was observed for the experiments with un-equal horizontal principal stresses (Cook et al., 2004).

2.5.7 Wellbore Direction

Abass et al. (1996) performed an experimental study on hydraulic fracturing of horizontal wells with openhole completion to study non-planar fractures and their consequences. They defined a non-planar fracture as any fracture that does not follow the conventional single-fracture geometry. They found three types of non-planar fractures: multiple parallel fractures, reoriented fractures and T-shaped fractures. The type of fractures depended on the deviation angle of the wellbore with respect to the maximum horizontal stress.

Fracture initiation pressure is a reflection of the disturbed stress field around the wellbore and also is a function of a wellbore azimuth, while propagation pressure represents the minimum in situ stress (Abass et al., 1996). Referring to Fig. 2-10, as the angle between the horizontal wellbore axis and the maximum horizontal stress increases, fracture breakdown pressure increases (Abass et al., 1996).

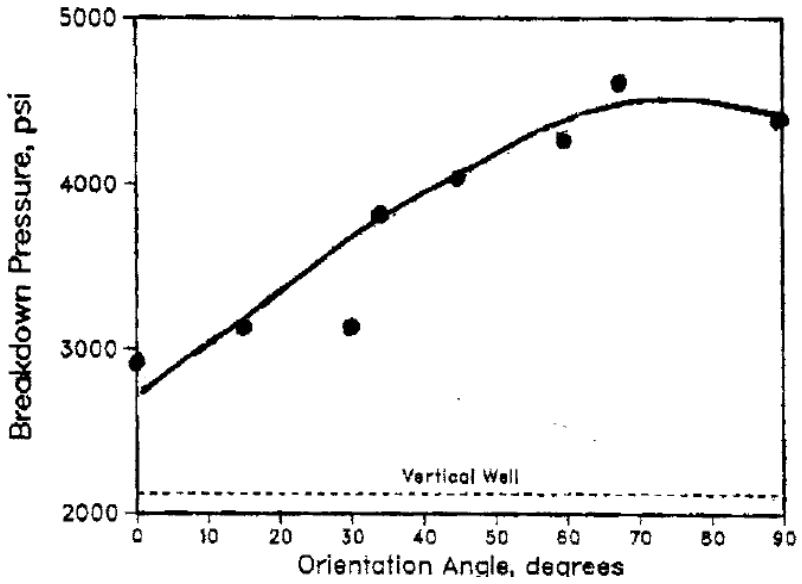

Fig. 2-10: Initiation pressure as a function of the wellbore deviation angle from maximum horizontal stress (Abass et al., 1996)

2.5.8 Injection Rate

In the experiments conducted by Zhou et al. (2010), a lower injection rate of a viscous fluid of 3500 cp into unconsolidated sand of 300-600 md resulted in branching and sub-parallel fractures while a higher injection rate induced a planar

tortuous fracture. Fracturing pressure was 2.5 times the confining stress (7 MPa) for the lower injection rate, which may be attributed to higher pressure diffusion and more shearing.

When fluid with a 2% solid concentration was injected into cohesionless sand, higher injection rates resulted in a transition from a single planar crack to multiple branching all around the wellbore (Golovin et al., 2010). In their large-scale experiment on cubic samples of cohesionless sand, Jasarevic et al. (2010) observed multiple primary fractures formed at random locations all around the cased and perforated wellbore before the main fracture propagated in the direction perpendicular to the minimum stress (Fig. 2-11). They found that the length of these primary fractures is inversely related to the flow rate.

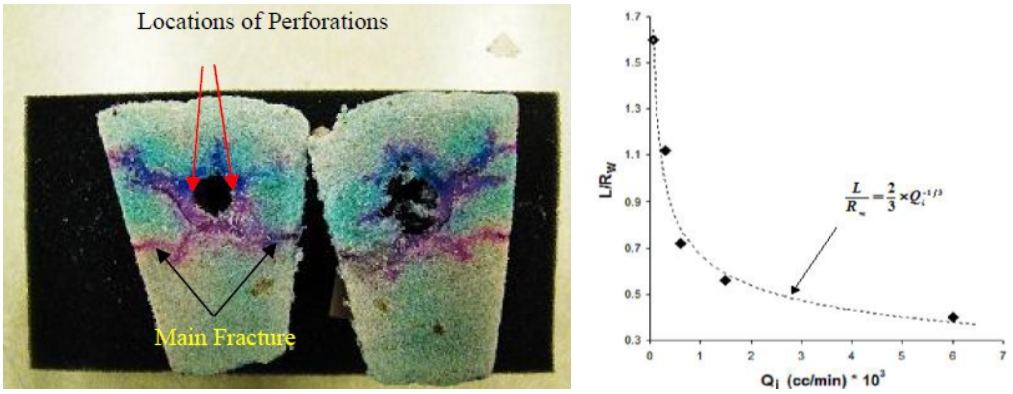

Fig. 2-11: Multiple primary fractures form before propagation of the main fracture (Jasarevic et al., 2010)

2.6 Review of Numerical Models for Hydraulic Fracture

The following are three important aspects of hydraulic fracturing of unconsolidated sandstones which should be incorporated in the modeling (Xu and Wong, 2010):

- The poroelastic deformation and shear and tensile failure/fracture of the matrix induced by pore fluid pressure;
- Fluid flow in shear and tensile fractures as well as the matrix;
- Initiation and propagation of the shear and tensile fractures in the matrix.

Tensile mode hydraulic fracturing has been extensively studied in past decades (Pak, 1997; Papanastasiou, 1997b; van Dam et al., 2000; Settari et al., 2002b; Cook et al., 2004; Lian et al., 2006; Xue et al., 2006; Ji, 2008; Zandi et al., 2010; Zhang et al., 2010). Several researchers have also investigated shear mode hydraulic fracturing of weak sand (Settari et al., 1989; Pak, 1997; Pak and Chan, 2004; Zhai and Sharma, 2005; Wu, 2006; Zhai, 2006; Xu, 2010; Xu and Wong, 2010).

The assumptions of linear elastic fracture mechanics (LEFM) for crack-tip propagation and a tensile two-wing fracture are not valid in unconsolidated and weakly-consolidated sandstones when plastic deformation is involved (Khodaverdian and McElfresh, 2000; McElfresh et al., 2002; Di Lullo et al., 2004; Bohloli and de Pater, 2006; Huang et al., 2011).

Existing numerical hydraulic fracture models are based either on smeared fracturing (Chin and Montgomery, 2004; Zhai and Sharma, 2005; Zhai, 2006; Xu, 2010; Xu and Wong, 2010; Xu et al., 2010), or discrete fracture (Hagoort et al., 1980; Settari, 1980; Nghiem et al., 1984; Settari, 1988; Settari et al., 1989; Settari et al., 1990; Settari et al., 1992; Papanastasiou, 1997a; Papanastasiou, 1997b; Papanastasiou, 1999; van Dam et al., 2000; Settari et al., 2002a; Settari et al., 2002b; Ji et al., 2004; Ji et al., 2006; Wu, 2006; Ji, 2008; Ji et al., 2009) or discrete element (Cook et al., 2004; Gil, 2005; Gil and Roegiers, 2006) approaches. They can also be divided into two major groups: models that need a predefined direction for the hydraulic fracture and models that can predict the fracture direction. Based on this classification, the following sections provide a description of existing numerical models of hydraulic fracturing.

2.6.1 Models with Prescribed Fracture Direction

2.6.1.1 Continuum Approaches

Conventional hydraulic fracture models were developed for designing hydraulic fracturing treatments in the 1960s. In these models, fracture was simulated based on the material (volume) balance of injected fluid (Howard and Fast, 1970). The fracture volume at each time was equal to the total volume of

injected fluid minus the fluid volume leaked off from the fracture walls into the reservoir. The material balance of injected fluid is in the form of Eq. (2-1) (Ji, 2008) where V_f is the fracture volume and q_i and q_l are fluid injection and leak-off rates, respectively.

$$\frac{\partial V_f}{\partial t} = q_i - q_l \,, \quad \text{(2-1)}$$

Using Eq. (2-1) , the assumed fracture shape and the pressure distribution in the fracture can be used to calculate the fracture length and width (Howard and Fast, 1970; Gidley et al., 1989; Ji, 2008). The most popular two-dimensional fracture models are Carter's, PKN and GdK (Howard and Fast, 1970) models, which mainly differ in their basic assumptions. Carter's model assumes that fracture width is uniform through the fracture body. In the PKN model, the plane strain condition and elliptical fracture cross section are assumed for each vertical cross section perpendicular to the fracture. However, in the GdK model, the plane strain condition is assumed for the horizontal cross section. Both models assume a fixed fracture height equal to the height of the pay zone. For injection with a constant flow rate, these models calculate the fracture aperture at the wellbore, fracture length and injection pressure.

Conventional hydraulic fracturing models do not consider all the complex features (e.g., poroelasticity, plastic deformation and shearing around a fracture) and may not be adequate to simulate hydraulic fracturing in unconsolidated oil sands (Settari, 1988; Ji et al., 2004; Xu et al., 2010).

The initial (old) fracture/reservoir models included two different grid systems for solving fracture flow and reservoir flow (and heat transfer) (Settari, 1980; Nghiem et al., 1984) in which the equations could be solved in an uncoupled, sequentially or iteratively coupled manner. The initial models did not account for the way in which stress/deformation affected reservoir flow and the fracturing process (Settari, 1980). Settari (1980) used a fracture/flow model based on mass balance law (GdK model). In the initial fracture-reservoir models, the pressure drop in the fracture was considered negligible and the fracture flow was treated as

a boundary condition for reservoir flow (Hagoort et al., 1980; Settari, 1980; Nghiem et al., 1984). Hagoort (1978) derived equations to estimate the fracture initiation, propagation and opening/closure pressures. Settari (1980) used these equations to consider the effect of pore pressure (poroelasticity) on fracturing. Nghiem et al. (1984) used the GdK fracture model and developed a 3D reservoir-fracture model to evaluate the fracture initiation, propagation and closure pressures.

Settari (Settari, 1988; Settari et al., 1989) introduced a method for the modular (partial) coupling of flow/stress/fracture simulation by coupling fluid flow to soil mechanics. It was showed that shear failure occurs around the fracture face due to low effective normal stress, as illustrated schematically in Fig. 2-12.

In a coupled reservoir/stress/fracture model, Settari (1988) showed that the oil sands' fracturing process is controlled by fluid leak-off which is dominated by the mechanical behavior of the sand, such as shear failure at the fracture face. In addition, studies have shown that shear stress concentration at the fracture tip results in a plastic zone at the tip (Papanastasiou, 1997b; van Dam et al., 2000; Wu, 2006).

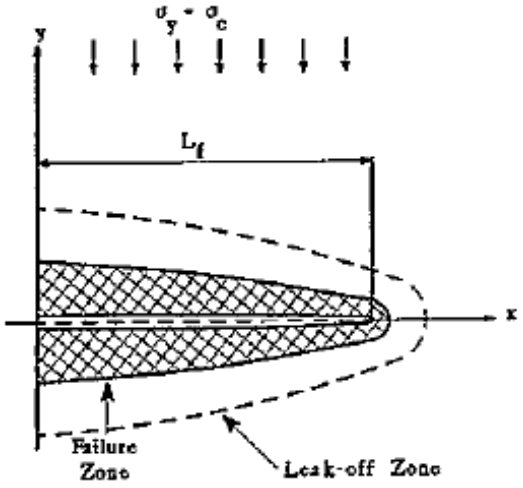

Fig. 2-12: Processes during fracturing of oil sands (Settari, 1988)

In early hydraulic fracture models, fracture equations were solved independently of the reservoir equations by using an overall coefficient for the leak-off (Settari et al., 1990). In late 1970's, another method was introduced in

which the fracture/reservoir equations were solved in a couple manner very similar to conventional reservoir simulation (Settari et al., 1990).

Settari et al. (1990) proposed partial coupling of the fracture and reservoir flow. Fracture equations were solved numerically during the propagation. A fracture grid was created dynamically independent of the reservoir grid. Leak-off was calculated for each element using an analytical/numerical model. Then, the average transmissibility (kh/μ) of the reservoir blocks containing the fracture were calculated and transferred to the reservoir model. The conventional reservoir model treated the fracture as a stationary fracture (Settari et al., 1990). Settari at al. (1992) showed that a dynamic fracture with multiphase flow can be simulated by dynamic enhancement of transmissibilities in the fracture plane.

A fracture model comprised of a geomechanical tool linked with a reservoir simulator can be an effective fracture modeling tool. In this model, the fracture is treated as the highly permeable part of the reservoir (Settari et al., 2002a; Settari et al., 2002b) and the fracture conductivity is combined with the permeability or transmissibility of the reservoir grid containing the fracture. Settari et al. (2002a) developed a 3D coupled fracture/reservoir/geomechanical model which simulates the fracture propagation during the fracturing job and the static fracture during the production. They used a dynamic transmissibility multiplier (the ratio of current permeability at the current pressure/stress to the original permeability under the original pressure/stress condition) in the fracture plane to simulate the fracture growth during the injection. This multiplier could be a function of pressure (for uncoupled modeling) or of effective stress (for coupled modeling).

Ji et al. (2004) presented modeling techniques for a fully coupled reservoir/fracture model of dynamic fracture propagation using a classic fracture model such as PKN or GdK. In their approach, fracture initiation (p_{fi}) and propagation pressure (p_{fp}) are calculated from the following equations:

$$p_{fi} = \sigma_{hi} + \frac{K_{IC}}{\sqrt{\pi L_{fi}}}, \quad \text{(2-2)}$$

$$p_{fp} = \sigma_h + \frac{K_{IC}}{\sqrt{\pi L_f}}, \quad \text{(2-3)}$$

where σ_{hi} is the initial minimum stress, K_{IC} is the critical stress intensity factor, L_{fi} is the initial fracture half-length and σ_h is the minimum in situ stress. Fracture length can be found by interpolating the grid pressures to find the position of the fracture tip. The fracture length, fracture maximum width and width distribution along the fracture can be calculated according to the GdK fracture model. The fracture width together with the pore pressure in the fractured element are used to calculate the fracture transmissibility. Then, the reservoir calculations are repeated to update the grid pressure. This cycle is repeated until convergence is attained for each time step.

In a 3D fully coupled flow-stress-fracture model developed by Ji et al. (2006; 2009), a finite element geomechanical model was coupled to a conventional finite difference reservoir simulator. In the older model, the stress/pressure-dependent dynamic transmissibility multiplier was introduced to consider the effect of fracturing on flow and stress-strain behavior. This multiplier changed significantly in the elements where fracturing occurred. Ji et al. (2006) used multipliers pre-computed in tables depending on either stress (in the coupled version) or pressure (in the uncoupled version) (Ji et al., 2009).

Ji et al. (2009) simulated fracture propagation implicitly by applying pressure on the fracture face. Fracture face displacements caused by the fracturing pressure are used to calculate the permeability multipliers (Ji et al., 2009). The reservoir and geomechanical/fracturing modules were coupled iteratively (Ji et al., 2009). The 3D planar fracture pressure and geometry were treated as dynamic boundary conditions in both the geomechanical and flow simulators, and the fracture was simulated as a highly permeable matrix. In the previous model (Ji et al., 2006), these multipliers were pre-computed as tables depending on either stress (in the coupled version) or pressure (in the uncoupled version) while in the new model (Ji et al., 2009), these multipliers were computed based on the fracture width (node displacement of the fracture face) from the geomechanical module. The equivalent permeability in the fracture plane (x and y direction in Fig. 2-13) was

assessed as a function of the fracture aperture based on cubic law and resulted in the following equations for the permeability multiplier (Ji et al., 2009):

$$in\ x\ direction: \boldsymbol{PMX_{mult}} = 1 + \frac{\boldsymbol{c_k}\overline{w}_f^{\,3}}{12\boldsymbol{k_x}\boldsymbol{\Delta y}}, \quad \text{(2-4)}$$

$$in\ z\ direction: \boldsymbol{PMZ_{mult}} = 1 + \frac{\boldsymbol{c_k}\overline{w}_f^{\,3}}{12\boldsymbol{k_z}\boldsymbol{\Delta x}}, \quad \text{(2-5)}$$

where Δx and Δz are the element (grid block) size in the x and y directions, respectively (see Fig. 2-13); the c_k coefficient is used to account for the factors decreasing fracture permeability such as fracture tortuosity, fracture face roughness and irregular shape of the channel; and $\overline{w}_f$ is the fracture width.

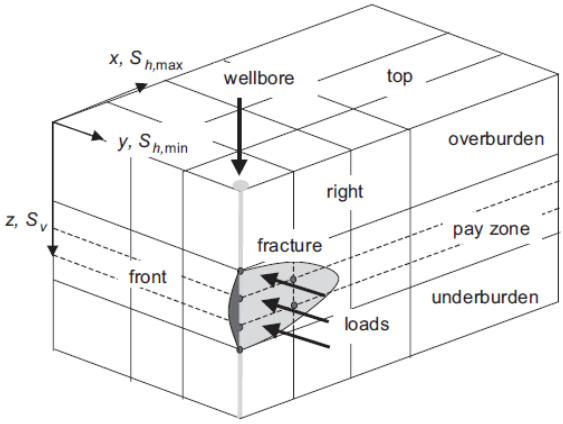

Fig. 2-13: Quarter layout of the fracture/reservoir model (Ji et al., 2009)

The matrix permeability is also updated according to the permeability relationship with stress/strain after calibration against laboratory tests or field data (Ji et al., 2009).

Assuming the fracture direction in an impermeable rock, Papanastasiou (1997a; 1997b; 1999) solved the continuity equation ($\partial w/\partial t + \partial q/\partial x = 0$, where w is the local fracture width and q is the flow rate) in conjunction with the lubrication theory (which relates the pressure gradient to the fracture width, for a Newtonian fluid of viscosity μ) and ignored the leak-off from the fracture into the rock matrix. van Dam et al. (2000) used a similar approach by solving the Poiseulle law and continuity equation. Studies have shown that that an elastoplastic (hardening) rock response would result in a shorter and wider

fracture and higher net pressure than would elastic solutions for fracture propagation (Papanastasiou, 1997a; Papanastasiou, 1999; van Dam et al., 2000).

2.6.1.2 Continuum-Discontinuum Approaches

The continuum-discontinuum group of hydraulic fracture models includes special types of elements like thin-layer solid elements or zero-thickness joint elements. To place these special types of elements in the model, it is necessary to know the fracture direction and location.

Xue et al. (2006) performed a coupled analysis of hydraulic fracturing using ABAQUS (based on the finite element method and cohesive elements using damage mechanics). Zhang et al. (2010) used ABAQUS to simulate a staged fracturing of a horizontal well in a thin pay zone. Their model included perforations, wellbore casing, cement, the pay zone, cap and base rocks, a micro-annulus fracture and a vertical transverse fracture. They found that the micro-annulus (see figure Fig. 2-14) fracture and the transverse fracture occurred simultaneously at early stages of the process and then the micro-annulus closed due to a higher stress concentration around the wellbore, but the transverse fracture propagated. It is worth noting that the micro-annulus fracture resembles multiple fractures discussed in laboratory experiments and field observations.

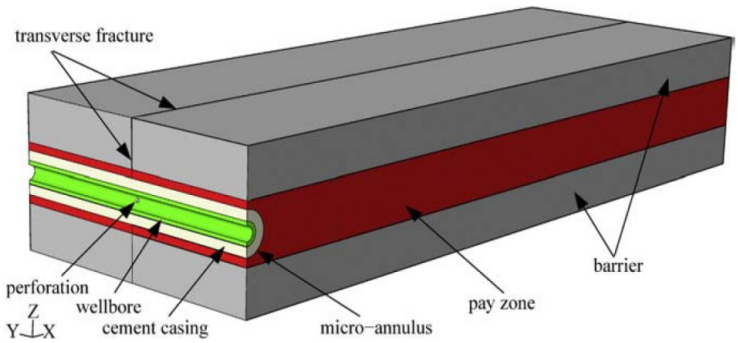

Fig. 2-14: Continuum-Discontinuum model by (Zhang et al., 2010)

Lian et al. (2006) simulated hydraulic fracturing using ABAQUS and found that permeability is more important in the fracture tip than in other places. Their study indicated that the void ratio of the medium reached the maximum value (in the model) at the fracture tip, resulting in a permeability increase. Similar results have been reported by other researchers (Khodaverdian and McElfresh, 2000;

Wu, 2006). This permeability enhancement may help the shearing process and increase the fracturing pressure.

2.6.2 Models without Prescribed Fracture Direction

The hydraulic fracture models that do not need any predetermined fracture direction are divided into two major groups: discontinuum and continuum models. In the discontinuum group, the discrete element method can simulate the rigid grains or deformable blocks and the interface between them. These types of models are impractical in terms of solution time and are incapable of simulating field-scale problems because of the large number of particles/blocks.

In continuum models, the fracture is smeared and the equivalent properties of the fracture and matrix, such as permeability and porosity, are assigned to the continuum mesh. This approach makes it possible to model fracture flow, matrix flow and the stress/strain effect on permeability in a fully or partially coupled manner. This method has been used to simulate fracturing jobs such as solid waste injection in soft rock reservoirs (Chin and Montgomery, 2004) and the fracturing of unconsolidated sands (Zhai and Sharma, 2005; Zhai, 2006; Xu, 2010).

2.6.2.1 Discontinuum Models (Discrete Element Models)

Cook et al. (2004) used a 2D DEM code, MIMES (Modeling Interacting Multibody Engineering Systems (Rege, 1996)), and extended it to fracture propagation during an experimental slurry injection in Berea Sandstone (loosely cemented sandstone). Their model consisted of a horizontal cross section of a 4 m by 4 m block with a 20 cm hole at its center. Inspired by the molecular model of a fluid, they used a circular source to pressurize the borehole.

Cook et al. (2004) showed that similar to their experiments, multiple fractures can occur when the two principal stresses are equal, leading to a higher storage capacity for the fractured medium, as shown in Fig. 2-15. In the case of different horizontal stresses, a distinct fracture occurs parallel to the direction of the maximum horizontal stress (Cook et al., 2004). Although this model can simulate the proper fracturing modes, it is limited because of its small size.

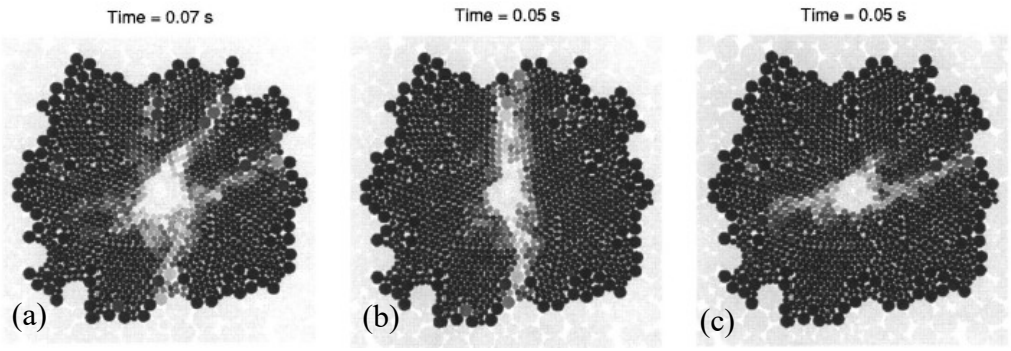

Fig. 2-15: Fracture pattern in DEM model by Cook et al. (2004); a) multiple fracturing in an isotropic stress condition, b and c) fracture perpendicular to the minimum stress at a stress ratio of 2:1 and 1:2 (Cook et al., 2004)

Gil (2005) and Gil and Roegiers (2006) developed a DEM model using PFC3D to determine the potential and importance of the shear failure mechanism and the effect of leak-off during hydraulic fracturing in poorly consolidated sandstones (Anter sandstone). Gil (2005) found that shear failure seems to be more important than tensile failure for these rocks. His model dimensions were H=4.6 m and L=W=3.4 m, including 1,537 particles simulating the sample at a depth of 3,048 m. Gil showed that low viscosity fluids under low differential stress (acting on samples) caused unstable crack propagation (fracture that reached model boundaries). The cracks appeared all around the wellbore and formed a cylindrical cloud around it. Conversely, high viscosity fluid (more than 500 cp) produced stable cracks regardless of the magnitude of differential pressure. The cracks were induced around the highest differential pressure area (near wellbore) without any preferential orientation.

At higher differential pressures (17 MPa), the effect of viscosity was marginal and the results of all the models were similar (Gil, 2005; Gil and Roegiers, 2006). The results show that for Anter Sandstone, shear failure is the dominant failure mechanism during hydraulic fracturing. That could explain why the field fracturing pressure is much larger than what is predicted for unconsolidated sands (Gil, 2005; Gil and Roegiers, 2006). Although the model is capable of capturing the discontinuous nature of the fractures, permeability/porosity change and failure modes, it can only be used for small-scale problems.

2.6.2.2 Continuum Models

2.6.2.2.1 Discrete Fracture Approach

The discrete fracture approach can be used to simulate induced fractures. In this approach, nodal grafting or the node-splitting technique (Pak, 1997) is implemented and an induced crack can pass through the boundaries of elements or inside elements.

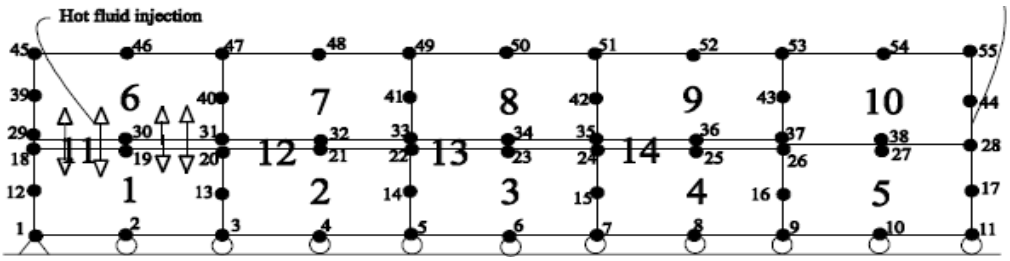

Fig. 2-16: Fracture model with node-splitting technique (Pak, 1997)

To allow the fracture propagation at element interfaces, a suitable shape function is added to the element interpolation functions. These additional shape functions can sometimes make the element incompatible and produce mesh locking (Pak, 1997). This method works well where the number of dominant fractures is limited.

Pak (1997; Pak and Chan, 2004) developed a 2D finite element thermo-hydro-mechanical numerical model (continuum discrete fracture model) of hydraulic fracturing in oil sands and utilized the model to simulate large-scale hydraulic fracturing experiments. In a finite element model with the node-splitting technique, double nodes with the same coordinates were placed in areas prone to cracking. When tensile or shear failure occurred, the double nodes split to two separate nodes. This method can propagate a fracture through the model. Pak (1997) used fracture elements to simulate fluid or heat flow inside the fracture such that when four of the fracture element's six nodes were split, the fracture scheme was activated and a finite value for permeability was assigned to the element. The results showed that a fracture can be initiated by tension, and that in the case of a highly porous reservoir with high permeability, a single planar fracture is unlikely to occur and the fracture pattern will appear in the form of a

fractured zone with a network of interconnected tiny fractures (Pak and Chan, 2004).

This model provides a basis for understanding the overall behavior of hydraulic fracturing in unconsolidated sand, but does not accurately capture the mechanical behavior (frictional sliding or opening) of shear/tensile fractures. Also, the permeability of a tensile fracture is not tied to its width.

2.6.2.2.2 Smeared Fracture Approach

In the smeared fracture approach, the medium, including the fractured and intact rock, is treated as a continuum, and the actual stresses and strains are averaged over a certain representative volume known as the crack band. In this approach, the fracture is simulated by altering the physical and mechanical properties of the elements that satisfy the fracturing criteria. The smeared crack model is expressed as a cracked material with equivalent anisotropic continuum properties that are degraded in the crack band (Klerck, 2000).

Whether to use the discrete or smeared fracture approach depends on the computational effectiveness of each (Bažant and Oh, 1983). The discrete approach involves some computational disadvantages. For instance, fracturing increases the number of nodes and changes the topological connectivity of the mesh, which creates significant challenges for automating the approach (Suidan and Schnobrich, 1973; Bažant and Oh, 1983). Even though the smeared fracture approach does not fully represent the physical nature of a crack, it is an alternative to the discrete fracture method, since it enables the simulation of fracture branching, fracture rotation and multiple shear and tensile fractures in un-predetermined directions.

In the smeared crack approach, the crack band is modeled by converting the isotropic elastic moduli of the matrix to an orthotropic one, including a reduction in the stiffness in the direction perpendicular to the fracture (Bažant and Oh, 1983). If a crack propagates in an arbitrary direction with respect to mesh lines or follows a curved path, it can be modeled as a zigzag crack band (see Fig. 2-17). The overall direction of this crack in the mesh approximates the actual crack

direction (Bažant and Oh, 1983), as shown in Fig. 2-17. The location of a fracture within the element cannot be captured in this approach. The smear fracture approach also does not account for the exact stress concentration at the fracture tip, since it averages the stresses over the crack band, which is smeared over the element(s) located at the tip.

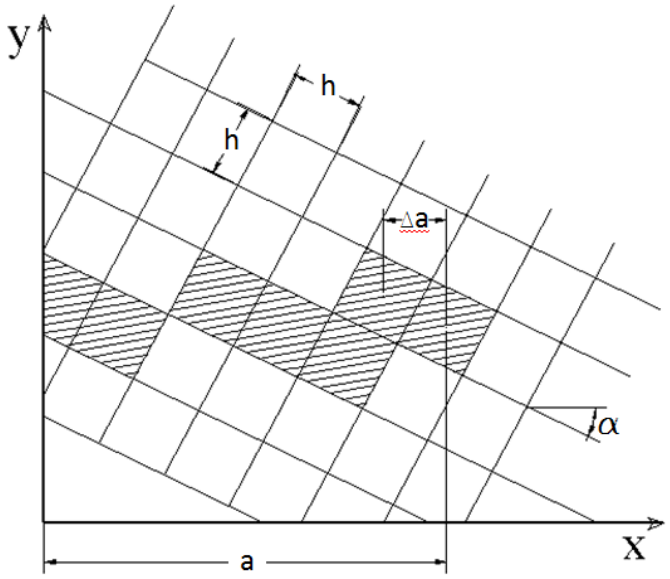

Fig. 2-17: Zigzag crack band with length "a" and overall direction of the crack (Bažant and Oh, 1983)

Researchers have proposed different methods to model a smeared crack fracture in concrete. The fixed crack model (Bažant and Oh, 1983), orthogonal fixed crack model (Klerck, 2000), rotating crack model (de Borst and Nauta, 1985) and stabilized rotating crack model (Bažant, 1984; de Borst and Nauta, 1985) have been proposed to consider single or multiple cracks in smeared crack modeling. A detailed review of these models can be found in Klerck (2000). The fixed crack model is overly stiff with induced shear stresses (shear response) and is unable to include the effective crack reorientation since the orientation of the crack band and the axes of orthotropy (of material behavior) are fixed at the onset of softening (Klerck, 2000). The orthogonal fixed crack model considers a new crack if it is orthogonal to the initial crack. These models need damage parameters to be defined according to the stress-strain behavior of the material in tension. Unlike the fixed crack models, the rotating crack model alleviates the excess

shear stress and is under-constrained and strictly valid for monotonic loading associated with the small rotations of principal axes. This model is also computationally expensive. The stabilized rotating crack models are capable of considering the loading history. These models also overcome the limitations of the fixed and rotating crack band models. The rotating crack models work well for large arbitrary rotations of crack bands due to dynamic loading, unloading or post-failure behavior (Klerck, 2000). However, these models use an LEFM approach which is not appropriate when large shearing and plastic zones enclose a tensile fracture.

The smeared fracture approach makes it possible to simulate the discrete nature of fractures, which is accomplished by reducing the stiffness of fractured elements, especially in tensile fractures. However, this approach requires modifying the permeability and porosity of the fractured element. Therefore, finding suitable formulae for the shear or tensile fracture permeability is of paramount importance. As will be shown later, the main difference between smeared hydraulic fracture models is how the shear/tensile-related permeability enhancement is calculated. Fracture permeability can be a function of effective stress, pore pressure, strain, porosity and saturation. In some of the existing hydraulic fracture models, the equivalent permeability of a fractured element is a function of effective stress or pore pressure while in others, it is calculated as a function of the displacement of the fractured elements.

In hydraulic fracturing of unconsolidated sand such as oil sand reservoirs in Alberta, a single fracture is unlikely to occur and the result of fracturing is a high porosity zone consisting of a network of micro-cracks (Pak, 1997; Xu et al., 2010). Continuum mechanics is suitable for modeling hydraulic fracturing in such formations (Xu et al., 2010). Fracturing in weak or unconsolidated sandstones occurs in the form of a zonal fracture rather than a planar fracture (Pak, 1997; Xu et al., 2010). A simulation must account for strong non-linearity arising from shear-induced dilation, tensile parting and variation of fluid mobility (Xu et al., 2010).

Using Drucker-Prager plasticity, Chin and Montgomery (2004) developed a 3D finite element model to simulate solid waste injection in unconsolidated sandstone reservoirs using the smeared fracture approach. They assumed that when pore pressure was larger than the minimum stress in any element, local confined fracturing would occur. An empirically estimated high permeability would then be assigned to that fracture element. In their model, matrix permeability was a function of mean effective stress as follows:

$$k = k_o.e^{-b(\sigma'_m - \sigma'_o)} \quad \text{(2-6)}$$

where k_o is the permeability at the reference effective mean stress (positive is compression) -usually the initial condition of laboratory test- and "b" is a parameter determined from experimental data for the specific reservoir.

Zhai and Sharma (2005) and Zhai (2006) developed an iteratively coupled 2D finite difference model for fracturing in unconsolidated sand. Porosity and permeability were empirical functions of volumetric strain and effective stress according to Eq. (2-7) and (2-8). Fig. 2-18 illustrates the permeability variation as a function of mean effective stress.

$$\phi = 1 - (1 - \phi_0) exp(-\varepsilon), \quad \text{(2-7)}$$

$$\frac{k_{ii}}{k_{iio}} = \frac{\left\{ ln\left[1 + \left(\sigma^* / \sigma'_{jk} \right)^2 \right] \right\}^m}{\left\{ ln\left[1 + \left(\sigma^* / \sigma'_{jko} \right)^2 \right] \right\}^m} \qquad (\text{i, j, k} = \text{r}, \theta, \text{z, respectively}), \quad \text{(2-8)}$$

where σ^* and m are coefficients that are determined from laboratory testing and σ'_{jk} is the net confining stress as follows:

$$\sigma'_{jk} = \frac{\sigma'_{jj} + \sigma'_{kk}}{2}, \quad \text{(2-9)}$$

Granular materials such as sandstone have been observed to show a dilative response due mainly to grains rolling over each other during the process of shear failure development, resulting in increased porosity and permeability. The permeability can be assessed using the equation below:

$$\frac{k_{ii}}{k_{iio}} = 1 + V\cos\alpha_i \quad \text{(2-10)}$$

In which $\cos\alpha_i$ is the unit vector perpendicular to the failure plane and V is a constant. The permeability variation versus effective stress is shown in Fig. 2-18.

Zhai and Sharma (2005) and Zhai (2006) concluded that in a normal faulting regime in unconsolidated sand, shear failure is the dominant or, likely, the sole fracturing mechanism. Tensile failure/fracture may occur at injection pressures exceeding the vertical stress (the max principal stress). For the strike-slip regime, shear failure was also concluded to be the dominant mechanism with tensile failure/fracture only occurring in the near wellbore region due to higher pore pressure (Zhai and Sharma, 2005).

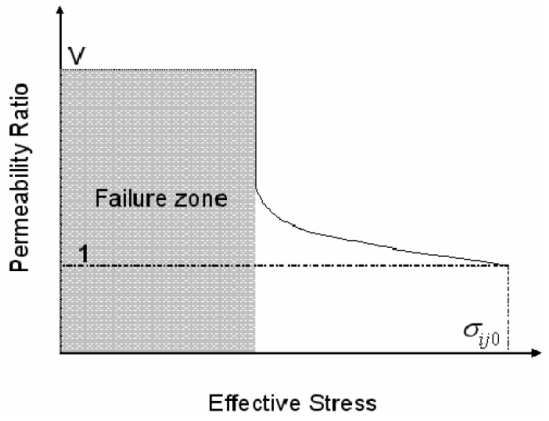

Fig. 2-18: Permeability change in the model before and after fracturing (Zhai and Sharma, 2005)

Xu et al. (2010) performed 3D fully coupled finite element simulation (smeared approach) of field-scale hydraulic fracturing in unconsolidated oil sand. In their model, the smeared fracture approach was used and permeability was a function of porosity (Kozeny-Carman equation) as well as saturation (relative permeability), as shown in Fig. 2-19.

$$S_w = \frac{(1-\phi)S_w^0\phi_0 + \phi - \phi_0}{\phi(1-\phi)} \quad \text{(2-11)}$$

$$k_a(\phi) = k_a^0\left(\frac{\phi}{\phi_0}\right)^c\left(\frac{1-\phi_0}{1-\phi}\right)^2 \quad \text{(2-12)}$$

$$\bar{k} = \frac{k_a k_{rw} \gamma_w}{\mu}, \quad \text{(2-13)}$$

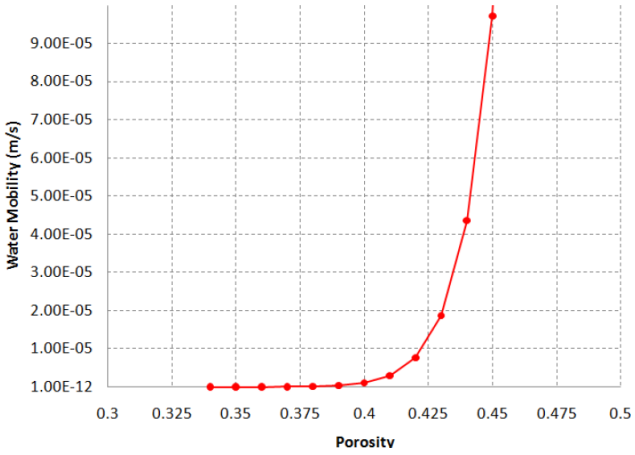

Fig. 2-19: Water permeability vs. porosity for absolute permeability of 3000 md, initial water saturation of 15% and initial porosity of 34% (Xu et al., 2010)

In order to simulate hydraulic fracturing in an unconsolidated sand reservoir, Xu (Xu, 2010; Xu and Wong, 2010) developed a 3D finite element method with an elastoplastic constitutive model using a strain-induced anisotropic full permeability model. In this hydraulic fracture model, stress level and stress path are considered in the permeability evolution. Xu and Wong (2010) used a non-associative Drucker-Prager model with isotropic strain hardening and softening and tension cut-off. To prevent a significant tensile strain in the elements that fail in tension, the element stiffness was set to a very low value (Xu and Wong, 2010). Xu and Wong used Eq. 2-14, which is slightly modified from the original model proposed by Wong (2003).

$$\begin{bmatrix} k_1 \\ k_2 \\ k_3 \end{bmatrix} = \begin{bmatrix} k_1^0 \\ k_2^0 \\ k_3^0 \end{bmatrix} \left\{ \begin{bmatrix} 1 \\ 1 \\ 1 \end{bmatrix} + \lambda \begin{bmatrix} a & b & b \\ b & a & b \\ b & b & a \end{bmatrix} \begin{bmatrix} \varepsilon_1 \\ \varepsilon_2 \\ \varepsilon_3 \end{bmatrix} \right\}, \quad \text{(2-14)}$$

in which k_i and k_i^0 are the principal values of induced permeability tensor and initial permeability tensor and ε_i are the principal values of strain tensor, a and b are material constants and λ is a permeability multiplier.

This multiplier relates a material's mechanical state to permeability and represents the connectivity of the microcracks in unconsolidated formations. By

combining the permeability multiplier with the mechanical behavior of the sand (Fig. 2-20), any change in the mechanical behavior can be coupled to the permeability matrix (Xu and Wong, 2010). This multiplier is related to the mechanical state as follows (Xu, 2010):

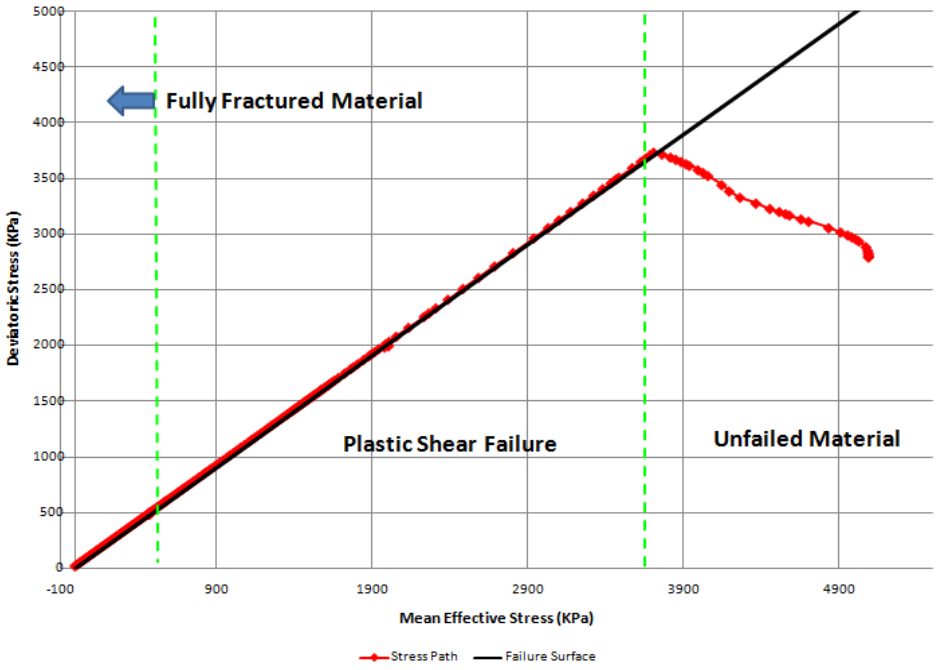

Fig. 2-20: Typical Stress path and matrix mechanical behavior (Xu and Wong, 2010)

$$a = \lambda a_0$$
$$b = \lambda b_0$$
$$\lambda = 0.5(1-h)\lambda_{min} + 0.5(1+h)\lambda_{max} \quad \text{.....} \quad \text{(2-15)}$$
$$h = \frac{\exp[m(\varepsilon^p - \xi)] - \exp[-m(\varepsilon^p - \xi)]}{\exp\left[m(\varepsilon^p - \xi)\right] + \exp[-m(\varepsilon^p - \xi)]}$$

where a_0 and b_0 are the initial values for a and b, λ_{min} and λ_{max} are the lower and upper bound for λ in the strain-induced permeability model, and ε^p is the equivalent plastic strain which is defined as:

$$\varepsilon^p = \int \sqrt{\dot{\varepsilon}_{ij}^p \dot{\varepsilon}_{ij}^p dt}\ , \quad \text{.....} \quad \text{(2-16)}$$

where ξ is the critical plastic strain beyond which a and b start to increase and m is a constant that controls the rate of change of a and b from their lower bound to upper bound. Fig. 2-21 illustrates how the permeability multiplier

changes with equivalent plastic strain. This permeability multiplier can be found by history-matching the field hydraulic fracturing data (Xu and Wong, 2010).

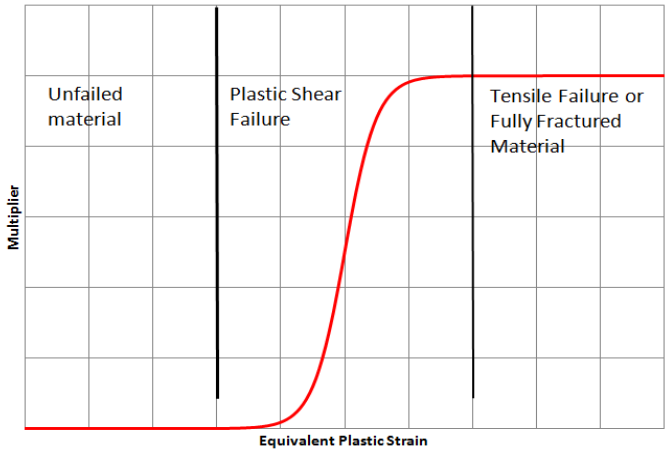

Fig. 2-21: Schematic of permeability multiplier as a function of equivalent plastic strain (Xu and Wong, 2010)

Xu (2010) and Xu and Wong (2010) showed that a high permeability zone (in which the predominate mode of failure is shear), resulting from fracturing, propagates out from an injection well similar to a tensile hydraulic fracture.

This model, however, does not adequately differentiate between the fluid flow behavior of shear and tensile fractures. In this model, equivalent plastic strain (and not the plastic tensile strain) controls the permeability change due to fracturing. The model works fine if shear failure occurs in a diffused form and is the main mechanism for fracturing. There is assumed to be no difference between the conductivity of a tensile fracture and a shear fracture, while the conductivity of a tensile fracture should be calculated according to a proper fracture flow law, such as the cubic law.

2.6.3 Assessment of the Existing Tools and Approaches

The major mechanisms and processes in the hydraulic fracturing of weak and unconsolidated sandstones mentioned previously must be considered in a numerical hydraulic fracturing model. Most of the current continuum-based numerical models for simulating hydraulic fracturing in weak or unconsolidated sandstones require a predetermined hydraulic fracture direction (Papanastasiou, 1997b; Lian et al., 2006; Xue et al., 2006; Ji et al., 2009; Zhang et al., 2010). Even

though some recent continuum models are adapted to capture fractures in general directions (Pak, 1997; Zhai, 2006; Xu, 2010), they lack a proper tensile fracture-flow law or do not simulate the development of shear bands and their interactions with the tensile fractures (Pak, 1997; Zhai, 2006; Xu and Wong, 2010).

Within the framework of continuum mechanics, the discrete fracture and the smeared fracture methods are the two approaches that have been extensively used to simulate hydraulic fractures. In the discrete fracture modes, interface/cohesive elements are used to simulate the fractures. Some restrictions, however, are of concern in these models: (1) the logic of these programs may break down if large numbers of interfaces are included in the simulation; (2) new contacts cannot be detected automatically; and (3) the models are based on small displacements and/or rotation (Nagel et al., 2011).

There is a lack of a hydraulic fracture model in which conductivity of a tensile fracture is calculated according to the governing fracture flow models (e.g. cubic law) and the direction of a tensile fracture is not predetermined.

2.7 Fracture Flow Formulation

This section presents a literature review on tensile and shear fracture flow to understand the proper governing mechanisms and equations in each fracture mode.

2.7.1 Tensile fracture flow equations

Assuming steady-state laminar flow of a Newtonian fluid between two parallel smooth plates (analogous to an ideal tensile fracture), the cubic law or parallel plate theory can be derived from the Navier-Stokes equations (Zimmerman and Bodvarsson, 1996; Waite et al., 1999; White, 2011). With the assumption of an incompressible fluid and no-slip boundary condition (meaning that the fluid velocity vector is equal to that of a solid at the solid-fluid boundary) (Zimmerman and Bodvarsson, 1996; Waite et al., 1999; White, 2011), the cubic law takes the form:

$$Q = C\bar{w}_f{}^3 \nabla h, \quad (2\text{-}17)$$

where Q is the flow rate, C is a constant that represents the geometry of the flow, $\bar{w}_f$ is the distance between the two plates (the fracture aperture), ∇ is the gradient operator and h is the hydraulic head.

For linear flow (Witherspoon et al., 1980; Zimmerman and Bodvarsson, 1996; Waite et al., 1999; White, 2011), C can be expressed as:

$$C = \frac{\rho g \bar{w}_f}{12\mu L}, \quad (2\text{-}18)$$

where $\bar{w}_f$ and L are the opening and length of the fracture, respectively, μ and ρ are the fluid density and viscosity, respectively, and g is the gravitational acceleration.

For radial flow (e.g., a horizontal fracture in a vertical well) (Witherspoon et al., 1980), C can be expressed as:

$$C = \left(\frac{2\pi}{\ln\left(r_e/r_w\right)}\right)\left(\frac{\rho g}{12\mu}\right), \quad (2\text{-}19)$$

where r_e and r_w are the outer boundary and wellbore radius, respectively.

Assuming that the wall shear stress, τ_w, in the fracture flow is constant, it can be normalized, resulting in the friction factor (White, 2011):

$$f = \frac{8\tau_w}{\rho v^2} = \frac{12\mu}{\rho v \bar{w}_f} = \frac{a}{N_{Re}}, \quad (2\text{-}20)$$

and Reynolds number:

$$N_{\mathrm{Re}} = \frac{\rho \upsilon D}{\mu}, \quad (2\text{-}21)$$

where v is fluid velocity and D is the half-aperture ($D = \bar{w}_f/2$). The constant, a, equals 96 (Witherspoon et al., 1980; Warpinski, 1985; Aydin, 2001; White, 2011). Chen et al. (2009) proposed Moody-type diagrams to find the friction coefficients of rough artificial fracture walls made of sand particles and cement.

Equation (2-20) is further modified to include the influence of fracture wall roughness (Witherspoon et al., 1980; Warpinski, 1985; Aydin, 2001) as follows:

$$f = \frac{a}{N_{Re}} F_{rough}, \quad \text{(2-22)}$$

In this equation, F_{rough} represents the relative roughness of the fracture walls (i.e., the ratio of the height of asperities to the fracture aperture). A value of larger than one for F_{rough} represents deviation from the ideal conditions assumed in deriving Eq. 2-20. Lomize (1951) proposed the following equations for the roughness of the fracture walls in laminar flow for $\varepsilon / \overline{w}_f > 0.065$:

$$F_{rough} = \left[1 + 17 \left(\frac{\varepsilon}{\overline{w}_f} \right)^{1.5} \right], \quad \text{(2-23)}$$

where ε is the height of asperities. Per Lomize's extensive study, the factor 17 makes F_{rough} strongly dependent on the relative roughness of the fracture walls. By performing similar experiments, Louis (1969) proposed a similar equation but a different coefficient. Huitt (1956), Parish (1963) and Aydin (2001) have also described different equations for F_{rough}, which are not mentioned here.

The cubic law, Eq. (1), is now modified to include the fracture wall roughness (Witherspoon et al., 1980; Aydin, 2001), as follows:

$$Q = \frac{C}{F_{rough}} \overline{w}_f{}^3 \nabla h, \quad \text{(2-24)}$$

Hydraulic conductivity of a fracture has been defined to be equivalent to the permeability parameter in Darcy's law for fluid flow in porous media (Zimmerman and Bodvarsson, 1996). The fracture conductivity can be related to the equivalent fracture permeability, as follows:

$$k_f = \frac{\overline{w}_f{}^2}{12 F_{rough}}, \quad \text{(2-25)}$$

where k_f is measured in square meters.

Oron and Berkowitz (1998) conducted experiments with water flow in fractures with wavy walls (sinusoidal representing large-scale roughness) at small Reynolds numbers and also performed simulations using lattice gas automata. They suggested that the aperture should be averaged over a certain fracture length. Waite et al. (1998; 1999) concluded that the tortuosity of the flow path and the aperture normal to the flow path should be considered in the cubic law equation. The tortuosity factor would appear in the denominator of Eq. 2-24 and would depend on the shape of the fracture configuration (sinusoidal in the Waite et al. study).

Modeling a fracture using a numerical method with the element size equal to the fracture thickness will result in a very fine mesh due to the typically small aperture size compared to the model size, rendering the solution of such engineering problems computationally impractical (Settari et al., 1990; Weill and Latil, 1992). It has been demonstrated that a fracture can be included in much larger elements, provided that an equivalent permeability of the element is determined using the average of the matrix permeability and the fracture conductivity (Settari et al., 1990; Weill and Latil, 1992; Ji, 2008). Weill and Latil (1992) reported some mesh size effect in using the smearing method in their simulations with element sizes of up to 10 m.

Based on the equivalent permeability of a fractured element, Ji (2008; Ji et al., 2009) used Eq. (2-26) to define a permeability multiplier (PM). A PM is a coefficient which, when multiplied by the matrix permeability, gives the fracture permeability. The PM of unity indicates fracture permeability equal to matrix permeability for the case where no tensile fracture has been detected.

$$PM = 1 + \frac{c_k \bar{w}_f^3}{12 k_m t}, \quad \text{(2-26)}$$

where c_k is the coefficient for deviation from ideal conditions due to the roughness of the fracture, $\bar{w}_f$ is the nodal tensile displacement, t is the element equivalent thickness in the direction of tensile stress, and k_m is the initial

permeability of the matrix. The element permeability in the direction of the tensile stress remains equal to the matrix permeability.

2.7.2 Transition from Laminar to Turbulent Flow in Fractures

Lomize (1951) and Louis (1969) found that the transition from laminar to turbulent flow occurs at the Reynolds number of 2400. Huitt (1956) proposed a value of 1800 to 4500, depending on the surface roughness. Chen et al. (2009) concluded that the critical Reynolds number for rough fracture walls made of sand particles and cement is between 650 and 700. Qian et al. (2005) observed fully turbulent flow at a Reynolds number of 333 to 1414 in their large scale laboratory experiments on a rough-wall single fracture at large pressure gradients. According to Zimmerman and Yeo (2000), this transition occurs at a Reynolds number of 10. Based on their experiments of water flow in rough fractures as well as numerical modeling, Nicholl et al. (1999) proposed the critical Reynolds number of one for a linear relationship between pressure gradient and flow rate, which is much smaller than the values proposed by the others.

2.7.3 Forchheimer Equation for Turbulent Flow in Fractures

Darcy's law does not adequately describe fluid flow with high flow velocities. A Forchheimer equation (Li and Engler, 2001) has been used for non-Darcian flow in porous media:

$$-\frac{dp}{dx} = \frac{\mu}{k}u + \beta\rho u^2 , \quad \text{(2-27)}$$

where u is fluid velocity, β is the non-Darcy coefficient, and μ and ρ are fluid viscosity and density, respectively. The non-linear term $\beta\rho u^2$ accounts for turbulence as well as inertial effects.

By performing laboratory experiments on fractures (1 m long and 0.25 m high) with apertures of four to nine millimeters at a Reynolds number of 12.2 to 86, Qian et al. (2011) showed that the flow in a single fracture is best described by the Forchheimer equation:

$$-\frac{dp}{dx}=\frac{1}{k_1}u+\frac{1}{k_2}\rho u^2, \quad (2\text{-}28)$$

Similar results were obtained by Qian et al. (2007) in their experiments on rough fractures with apertures of 1.0, 2.0 and 2.5 millimeters and a Reynolds number between 245 and 759.

However, the relationship between coefficients *k1* and *k2* with an aperture and roughness of fracture walls was not specified and would need to be studied. The results reported by Qian et al. (2011) showed that cubic law provides acceptable accuracy for low-flow velocities.

2.7.4 Izbash Equation (Power Law) for Fully Turbulent Flow in Fractures

Qian et al. (2005; 2007) performed large-scale laboratory experiments on fully turbulent water flow in a single fracture five m in long and 1.6 m wide. To simulate the roughness of the fracture walls, Qian et al. used mixtures of sand-cement with different sand particle PSDs of 1-2, 0.5-1 and 0.25 to 0.5 millimeters to create coarse, medium and fine roughness, respectively. Their experiments covered fluid velocity in the range of 0.1 to 0.95 m/s, apertures of one to six millimeters and Reynolds numbers of 245 to 1414. Qian (2005; 2007) showed that for fully turbulent flow in a single fracture, the coefficient of the linear term *(1/k1)* in a Forchheimer equation is small compared to that of the non-linear term *(1/k2)* and could be neglected. Therefore, the Forchheimer equation reduces to the Izbash equation (power-law) as follows (Qian et al., 2005; 2007):

$$-\frac{dp}{dx}=\frac{1}{k}u^2, \quad (2\text{-}29)$$

where k is a factor that represents the hydraulic conductivity of a fracture and is calculated as (Qian et al., 2005; 2007):

$$k=\frac{\bar{w}_f g}{f_w}, \quad (2\text{-}30)$$

which gives the following form of the Izbash equation for fully turbulent fluid flow in rough fractures:

$$u = \sqrt{\frac{\bar{w}_f g}{f_w}} \sqrt{\frac{dp}{dx}}, \quad \text{(2-31)}$$

where $\bar{w}_f$ is the aperture of the fracture, g is the gravitational acceleration, and f_w is determined from Moody's diagram (Qian et al., 2005).

2.7.5 Shear Failure/Fracture Flow

As discussed before, the permeability of a rock matrix may increase due to the dilative rock response in the shearing process. A few permeability correlations have accounted for shear-enhanced permeability; Kozeny-Carman (Das, 2008) and the models presented by Tortike and Ali (1993), Touhidi-Baghini (1998) and Wong (2003), which are discussed briefly below.

The Kozeny-Carman equation expresses absolute permeability as a function of porosity:

$$\frac{k}{k_0} = \left(\frac{\phi}{\phi_0}\right)^3 \frac{(1-\phi_0)^2}{(1+\phi)}, \quad \text{(2-32)}$$

where k and ϕ are permeability and porosity, respectively, and the subscript zero denotes the initial value.

Derived from Kozeny-Carman's model, Tortike's equation relates permeability to volumetric strain, ε_v (Tortike and Ali, 1993; Li and Chalaturnyk, 2006), as follows:

$$\frac{k}{k_0} = \frac{(1+\varepsilon_v/\phi_0)^3}{(1+\varepsilon_v)}, \quad \text{(2-33)}$$

Li and Chalaturnyk (2006) conclude that this equation is applicable to determine the modified absolute permeability during isotropic unloading if the initial absolute permeability is greater than 1 x 10^{-12} m^2 (about 1 Darcy).

Based on permeability measurements during triaxial testing, Touhidi-Baghini (1998) proposed Eq. (2-34) for the permeability enhancement of McMurray oil sands (unconsolidated sandstone) due to shear dilation. The main assumption in this model is that rock matrix permeability variation is negligible during the initial

elastic contraction before and at the beginning of shearing (see Fig. 2-22), and a major increase will occur during the shear dilation phase, as schematically illustrated in Fig. 2-22.

$$Ln\frac{k}{k_0}=\frac{B}{\phi_0}\varepsilon_v, \quad \text{(2-34)}$$

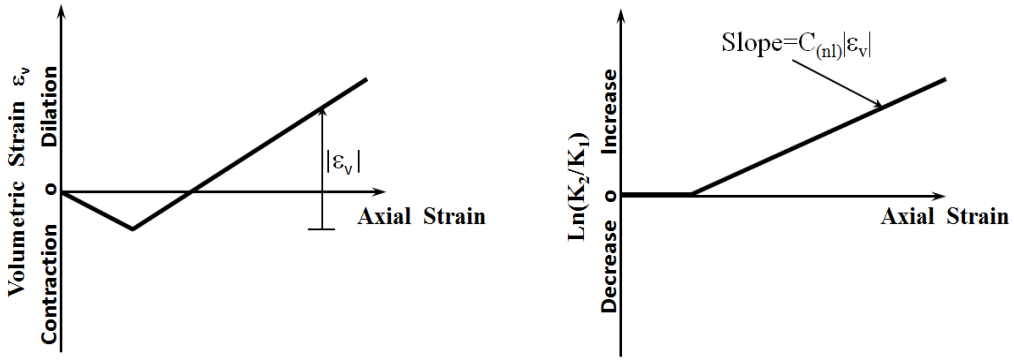

Fig. 2-22: Typical volumetric strain behavior and the corresponding absolute permeability variation (Touhidi-Baghini, 1998)

The B factor may not be the same for different directions. With B_h=2 and B_v=5, Touhidi-Baghini (1998) obtained a good agreement with the experimental results for core plugs taken in the directions parallel and normal to the bedding plane.

Based on experimental results, Wong (2003) proposed a strain-induced permeability model for deformable porous media in which the permeability is a linear function of strains. In this model, the principal permeability directions do not necessarily coincide with the principal strain directions. With the assumptions of isotropy and a linear relationship between permeabilities and strain components, only two constants are needed to characterize the new permeability (Wong, 2003).

$$\begin{aligned} k_1 &= k_1^{\,0} + a\left(\varepsilon_1+\varepsilon_3\right)+(b-a)\varepsilon_3 \\ k_3 &= k_3^{\,0} + \left(b-a\right)\varepsilon_1 + a\left(\varepsilon_1+\varepsilon_3\right) \end{aligned} \qquad for\ 2D\,(e.g.\ plane\ strain), \quad \text{(2-35)}$$

where k_1^0 and k_3^0 are the initial principal permeabilities, ε_1 and ε_2 are the principal strains, and a and b are calibration parameters. The constants a and $b-a$ characterize the permeability variation that resulted from both volumetric

and shear deformation, respectively. The larger value of a compared to $b-a$ implies that the permeability variation is primarily dominated by the porosity change, and the tortuosity effect is of secondary importance (Wong, 2003).

Dilatant behavior has been shown to be the main factor in permeability enhancement during the shearing process (Chalaturnyk, 1996; Touhidi-Baghini, 1998). Permeability enhancement due to shearing occurs during the dilative phase and levels off as the critical state is approached. Yuan and Harrison (2005) proposed a model for permeability enhancement caused by shear dilation by relating the permeability of the element to its volumetric strain. The main assumption in this model is that the degraded rock element with volume V can be considered as a unit containing two fractures in orthogonal directions with equal aperture, e, as illustrated schematically in Fig. 2-23. By applying the lubrication theory and relating apertures of the two fractures to the volumetric strain of the elements, Yuan and Harrison (2005) proposed the following relationship:

$$k = \frac{e^2 g}{12\mu} = \frac{Vg}{48\mu}\varepsilon_v^{\,2}, \quad \text{(2-36)}$$

Darcy's law for fluid flow in porous media is used to solve the flow in the intact matrix as well as the tensile fracture and shear failure/fracture:

$$q_i = -\frac{k_{ij}}{\mu}\frac{\partial}{\partial x_j}\left(P - \rho_f g_k x_k\right), \quad \text{(2-37)}$$

where q_i is the specific discharge vector, k_{ij} is the permeability, μ is the fluid viscosity, P is the fluid pressure, ρ_f is the mass density of the fluid and g_k, subscript j and k = 1, 2 are the two components of the gravity acceleration vector, and x_j and x_k are components of the coordinate vector.

2.7.6 Porosity Alteration

Rock porosity varies during deformation. Porosity is related to volumetric strain, which can be calculated using a geomechanical model, as follows (Touhidi-Baghini, 1998):

$$\phi = \frac{(\varepsilon_v + \phi_0)}{(1+\varepsilon_v)}, \quad \text{(2-38)}$$

where ϕ_0 and ϕ are the initial and current porosities, respectively, and ε_v is the volumetric strain.

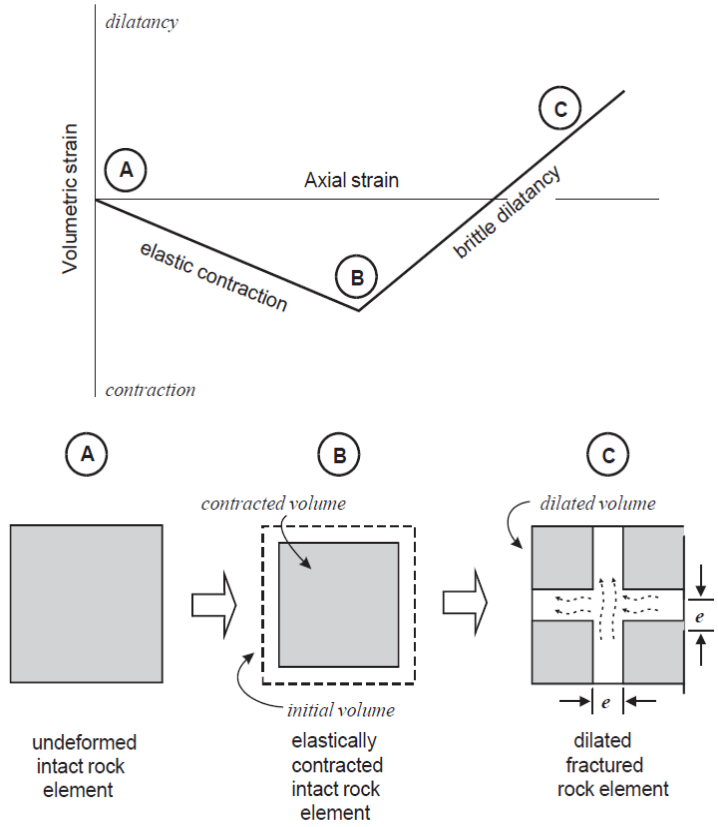

Fig. 2-23: Schematic representation of elastic compression and dilation during fracturing (Yuan and Harrison, 2005).

2.8 Summary

A review of the literature indicates the absence of a suitable hydraulic fracture model that (1) employs proper fracture flow equations (e.g., the cubic law), and (2) can capture the direction of a tensile fracture. Even though the smeared fracture approach does not fully represent the physical nature of a fracture, it is an alternative method to simulate tensile fractures and shear failure in un-predetermined directions.

A review of the existing hydraulic fracture models indicates that these models lack at least one important aspect of the hydraulic fracture processes. Either the

conductivity of the tensile fracture is not properly calculated or the direction of the tensile fracture is predetermined. In this research, the smeared fracture approach is employed. In this approach, a fracture is simulated by altering the physical and mechanical properties of the elements that satisfy the fracturing criteria.

To calculate the hydraulic conductivity of a fracture, a suitable fluid flow equation for tensile fracture flow has to be implemented in the smeared tensile fracture model. This conductivity can then be converted to the permeability parameter in Darcy's law to calculate fluid flow in the fractured porous medium.

To simulate shear failure in the smeared numerical model, a shear permeability function is required that can capture the nonlinear dependency of anisotropic permeability on volumetric strain. Tortike's, Kozeny-Carman's and Yuan and Harrison's equations assume isotropic permeability enhancement unlike Wong's and Touhidi-Baghini's models. The shear-enhanced permeability in Wong's model is a function of both shear and volumetric strain. Wong's model assumes a linear relationship between volumetric strain and enhanced permeability. However, Touhidi-Baghini (1998) showed that the absolute permeability of oil sands is a nonlinear function of the volumetric strain. Touhidi-Baghini's model in the form of Eq. (2-34) can be used to describe the shear permeability enhancement in hydraulic fracturing simulations. Porosity variation as a function of volumetric strain evolution (due to shearing and the dilation of unconsolidated and weakly consolidated sandstones) must also be considered a hydraulic fracture model.

Chapter 3: Smeared Hydraulic Fracture Model: Formulation and Model Verification

3.1 Introduction

This chapter presents the formulation of the smeared hydraulic fracture model used in this research. The calculation of the equivalent permeability of the shear- or tensile-fractured elements is the main challenge in the smeared fracture modeling approach. The formulation and methodology for a smeared tensile fracture used in this research are also discussed. This chapter presents the verification of the tensile fracture model against other models in the literature.

3.2 The smeared tensile fracture flow formulation

In this work, permeability of a tensile fracture is evaluated by using the permeability multiplier (PM) parameter as introduced in Eq. (2-26). The element permeability in the direction of the tensile stress remains equal to the matrix permeability.

Element tensile strain (the tensile strain accumulated after the tensile fracture occurred) can be directly used to calculate the element permeability. The term $\overline{w}_f/t$ in Eq. (2-26) represents the tensile strain (ε_T) in the direction normal to the fracture. Element thickness, t, is equal to the square root of the element area. Therefore, Eq. (2-26) can be written in the following form:

$$PM = 1 + \frac{c_k \overline{w}_f^2}{12 k_m} \varepsilon_T = 1 + \frac{c_k}{12 k_m} \varepsilon_T{}^3 t^2 \quad \text{(3-1)}$$

where ε_T is the tensile strain after the tensile fracture is detected in the model. This equation can be used for the laminar flow of a Newtonian fluid between two parallel smooth plates. In this chapter, the fracture flow remains laminar because of the small fluid velocity. Fracture walls are assumed to be smooth, which is an

assumption in deriving the cubic law for ideal conditions. Lomize (1951), Huitt (1956), Parish (1963) and Aydin (2001) proposed different equations to describe the surface roughness of fractures. These equations can be added to the cubic law to take into account the roughness of fracture walls. As opposed to a narrow fracture in hard rocks, wide tensile fractures are expected in unconsolidated and weakly consolidated sandstones, where fracture roughness has a small influence on fracture conductivity. A different formulation has to be found for shear failure, as this type of flow occurs inside a porous material, while tensile fracture flow takes place in an open conduit.

In the numerical model developed for this research, the permeability multiplier *PM* is calculated from Eq. (3-1) after a tensile fracture is detected in the element. This multiplier is applied to the permeability in the fracture direction, while the permeability in the direction normal to the fracture remains unchanged or follows the shear permeability formula (eq. 2-34) if shear failure has been detected in the elements. This orthotropic permeability tensor is then rotated back to the global coordinate system, resulting in the anisotropic permeability tensor for the fractured element.

3.3 Examination of mesh dependency

The post-peak behavior of weakly consolidated sandstone at low effective confining stress involves intense strain localization and softening (softening refers to a decrease in the material's load-bearing capacity). The shear strain-softening behavior of rock-type material at low effective confining stress (LECS) (Sulem et al., 1999; Bésuelle et al., 2000) and the localization in tension (Klerck, 2000) have been investigated extensively in the literature. These behaviors are expected to be the predominant modes of failure/fracture around injection points in hydraulic fracturing jobs in weakly consolidated sandstones. Degradation in the tensile/shear band in weakly consolidated sandstones is localized in a width which is equal to the characteristic length of the material and is a function of grain size (Crook et al., 2003).

Since the Mohr-Coulomb plasticity model with or without softening does not take into consideration the size effect, a regularization technique, called fracture energy regularization, is implemented. This technique ensures that the energy dissipated in the formation of new surfaces of fracture (e.g. fracture energy release rate) is mesh invariant and the size effect is captured in the formulation (Crook et al., 2003). This method is simple and straightforward to implement and can be used to regularize the energy dissipated in both mode I and mode II fractures (Cook et al., 2004).

To attain mesh independency of the localization in this model, the approach described by Crook et al. (2003) is implemented. The approach builds on the work done by Bažant and Oh (1983) and Pietruszczak and Mróz (1981) (for Mode II fracture) and Klerck (2000) (for Mode I fracture). It is based on the idea that the fracture energy release rate, defined as the energy dissipated in the formation of new fracture surfaces, is invariant in various numerical mesh sizes, as illustrated in Fig. 3-1.

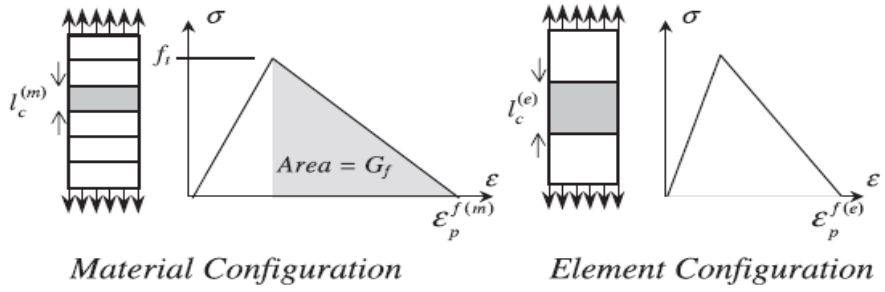

Fig. 3-1: Fracture energy dissipation (Crook et al., 2003)

The following two hypotheses are the basis for the fracture energy method (Nouri et al., 2009):

1. Bažant and Oh (1983) found that in strain-softening material, a sharp inter-element crack and a smeared crack give essentially the same energy release rate.
2. In standard strain-softening modeling techniques, deformations concentrate in narrow bands which collapse down in the smallest width

that can be resolved by the mesh. If the element size is selected equal to the band width, fracture energy can be estimated accurately.

For the element size larger than the shear band width, the fracture energy is kept constant by modifying the plastic shearing strain intensity by the following equation:

$$g^{p(e)} = g^{p(m)} \left[\frac{l_c^{(m)}}{l_c^{(e)}} \right]^n \quad \text{(3-2)}$$

where $l_c^{(m)}$ is the material characteristic length equivalent to the shear band thickness, $l_c^{(e)}$ is the element characteristic length defined as the diameter of the circle (sphere) having an area (volume in 3D) equal to the element under consideration, $g^{(e)}$ and $g^{(m)}$ are the inelastic fracturing strain (plastic shear strain for Mode II fracture and plastic tensile strain for Mode I fracture) of the material and element, respectively.

Finally, n is a material constant equal to 1, with the assumption of linear elastic fracture mechanics (LEFM), which is rational for a Mode I fracture of rock and concrete (Crook et al., 2003). Some rock types demonstrate a variable energy release rate when the fracture length changes (Bažant et al., 1993), which is illustrated by an R-curve (the material resistance to crack propagation (Anderson, 1991)). The behavior of these materials deviates from the assumption of LEFM and necessitates the parameter **n** to depart from 1.

Crook (2003) emphasizes that this localization limiter is only valid when $l_c^{(e)} \geq l_c^{(m)}$, meaning that the width of the localization band must be less than or equal to the element characteristic length which is usually the case in the field fracturing simulation.

The plastic shear strain, also called the equivalent plastic strain (EPS), is defined as (Itasca Consulting Group Inc., 2011):

$$g^p = \frac{1}{\sqrt{2}} \left[\left(\Delta e_1^{ps} - \Delta e_m^{ps} \right)^2 + \left(\Delta e_m^{ps} \right)^2 + \left(\Delta e_3^{ps} - \Delta e_m^{ps} \right)^2 \right]^{1/2} \quad \text{(3-3)}$$

where Δe_m^{ps} is the volumetric plastic shear strain increment, defined as:

$$\Delta e_m^{ps} = \frac{1}{3}\left(\Delta e_1^{ps} + \Delta e_3^{ps}\right), \quad \text{(3-4)}$$

and Δe_j^{ps}, (j=1, 2 and 3) are the principal plastic shear strain increments. Here Δe_2^{ps} is equal to zero for plane strain assumption. For tensile softening behavior, EPS will be equal to the plastic tensile strain increment, $\Delta \varepsilon_3^{pt}$.

Implementing this method in a numerical model does not require any modification of the standard numerical technique. To implement Eq. (3-2), a good estimation of the material characteristic length, $l_c^{(m)}$, or shear/tensile band thickness, is needed. Experiments have shown that the thickness of both tensile and shear bands can be in the order of the material's grain size. Vardoulakis and Sulem (1995) suggest a shear band thickness of 10 to 16 times the average grain size. Based on the literature, Desai (2001) concludes that for geological material, the width of a shear band is around 10 to 30 times the average grain diameter. Based on experimental observations, Wolf et al. (2003) suggest the band thickness is as much as 6 to 13 times the average grain size in granular materials. Bažant and Oh (1983) proposed a tensile band thickness of 3 times the aggregate sizes in concrete. If the average grain size of the weakly consolidated sandstone is known, it is possible to estimate an approximate material characteristic length.

3.4 Verification of the Smeared Tensile Hydraulic Fracture Model

In this section, the proposed smeared fracture approach is implemented and utilized in a numerical model based on the continuum mechanics assumption. The section presents the verification of the model against the numerical data reported by Papanastasiou (1997b), which is concerned with simulating hydraulic fracturing in an impermeable rock.

3.4.1 Numerical Model Description

The smeared fracture methodology was implemented in FLAC (Itasca Consulting Group Inc., 2011). The flow and mechanical calculation were

performed in FLAC using a sequentially coupled scheme. The hydraulic fracture was simulated in a plane-strain configuration, consistent with the work of Papanastasiou (1997b).

3.4.1.1 Material Properties

In his paper, Papanastasiou (1997b) considered three scenarios for the impermeable matrix: elastic with static modulus, elastic with dynamic modulus, and elastoplastic with cohesion-hardening. Verification results are presented here for all three cases.

The rock was assumed to undergo linear softening under tension before fracturing, a cohesive behavior (Barenblatt, 1962), as shown in Fig. 3-2, which was consistent with the model that Papanastasiou (1997b; Papanastasiou, 1999) used for the interface elements lying in the crack-growth direction. Fracture energy regularization was applied to this tensile model to reduce mesh dependency. A tensile strength of 0.5 MPa and a fracture toughness of 1.0 MPa$\sqrt{\text{m}}$ were considered for the material (1997b).

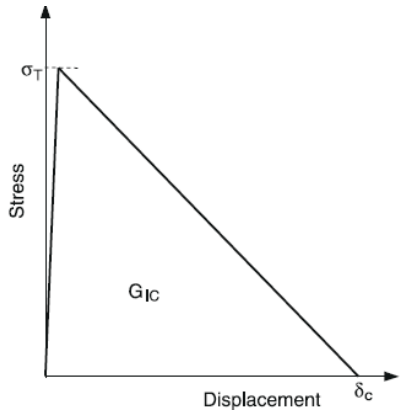

Fig. 3-2: Cohesive behavior of fracture (Papanastasiou, 1999)

The static and dynamic elastic modulus (E_{stat} and E_{dyn}) and Poisson's ratio were equal to 1.785, 16.200 GPa and 0.3, respectively. A friction angle of 28 degrees was considered, which was equal to the dilation angle for associated behavior. The initial uniaxial compressive strength was 4 MPa, and a strain-hardening behavior was considered in which the equivalent stress (uniaxial

compressive strength), σ^e, would increase with the accumulated plastic shear strain, ε_p (Papanastasiou, 1997b),

$$\sigma_e = \sigma_e^0 + h\varepsilon^p \quad \text{(Papanastasiou, 1997b),} \quad \textbf{(3-5)}$$

where **h** is called the linear hardening modulus, which is defined as:

$$h = \frac{E_{stat}}{1 - E_{stat}/E_{dyn}} \quad \text{(Papanastasiou, 1997b),} \quad \textbf{(3-6)}$$

The viscosity of the injecting fluid was 100 cp (10^{-7} MPa.sec). A very small permeability (10^{-15} md) was assigned to the matrix.

3.4.1.2 Model and Grid Size

The model height and width are 64 and 32 meters, respectively. Only one wing of the fracture was simulated in the model, as shown in Fig. 3-3. The model does not need to include an initial fracture (which was necessary in Papanastasiou's discrete fracture model). A uniform grid size of 20 m x 20 cm was used in the entire model except in an area of 4 m by 0.8 m around the injection point, as illustrated in Fig. 3-3. Three different grid sizes of 20 cm, 10 cm and 5 cm were used in this area to evaluate whether the results had a mesh dependency.

3.4.1.3 Initial and Boundary Conditions

All model boundaries were fixed against displacement in the normal direction. The maximum, intermediate and minimum in situ stresses of 14, 9 and 3.7 MPa were initialized in the model as shown in Fig. 3-3. Following the initialization of stresses, injection was applied at a constant rate of 0.0005 m^3/sec. Every grid point was checked for tensile fracture in each time step. The permeability multiplier was calculated for the failed elements using Eq. (3-1).

The stress/strain solution is achieved when the unbalanced-to-applied force ratio for all the gridpoints in the model becomes smaller than 0.001. The same tolerance was considered for the unbalanced fluid volume in the fluid flow analysis.

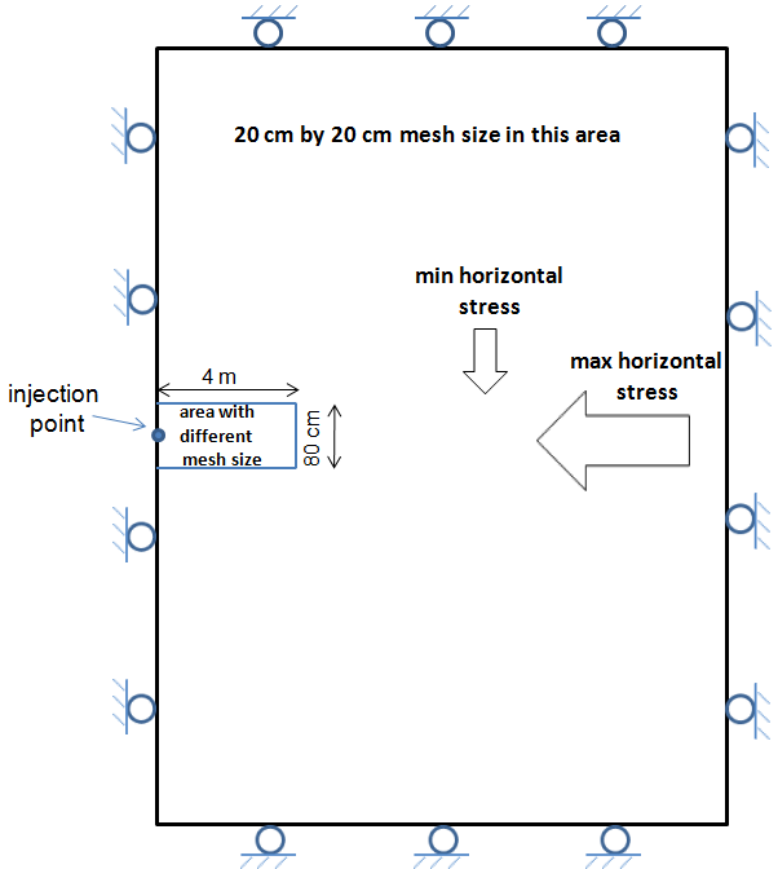

Fig. 3-3: Finite difference grid and boundary conditions

3.4.1.4 Numerical Modeling Results

Three different cases were considered for the verification purpose as used by Papanastasiou (1997b): elastic model with static modulus, elastic model with dynamic modulus, and elastoplastic model. Each case is analyzed using the three mesh sizes discussed in Section 3.4.1.2.

The fracture aperture in the developed smeared hydraulic fracture model is defined as the differential displacement of the two nodes containing a tensile fracture. Fig. 3-4 compares the fracture aperture profiles for the fracture length of 2.40 meters for both models. The elastic model with the static modulus shows a larger aperture along the entire fracture length. However, the model with the dynamic modulus results in a narrower fracture along part of the fracture. There is a reasonable agreement between the results of the proposed model and those of the Papanastasiou model (1997b).

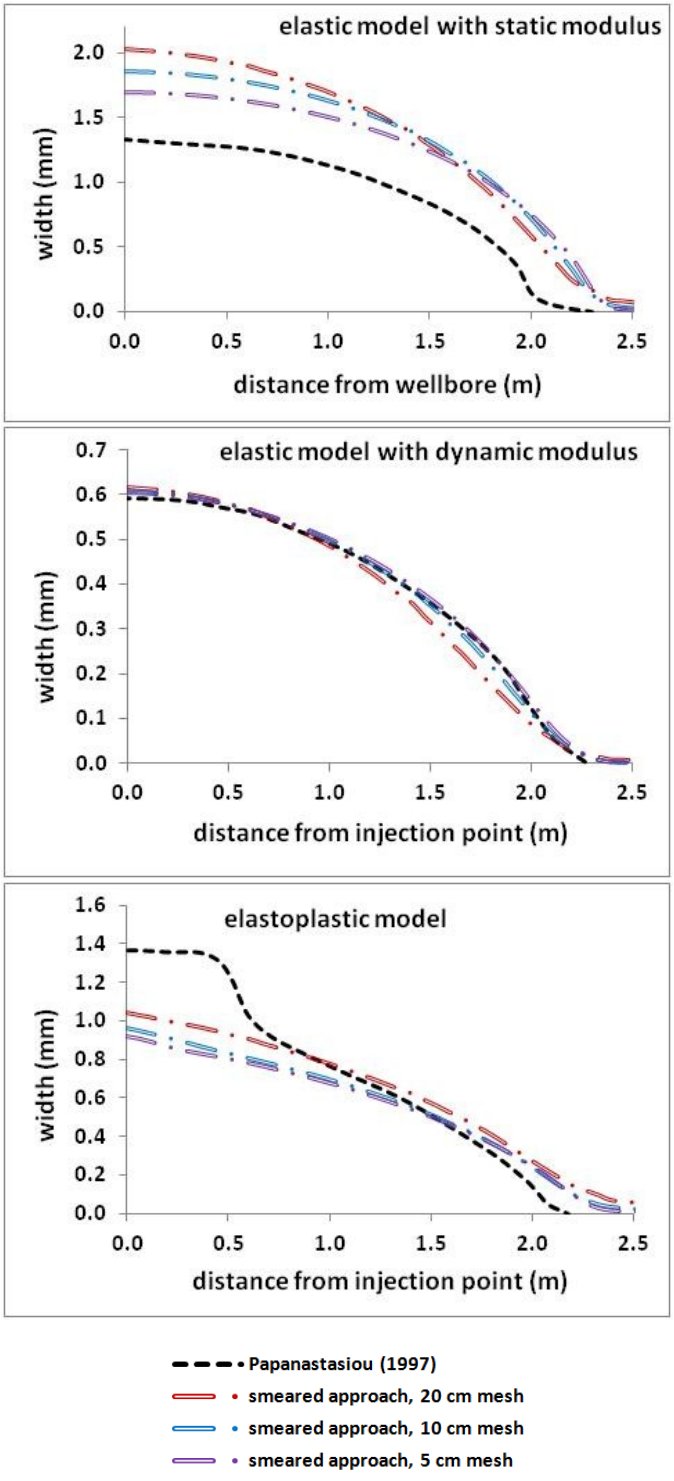

Fig. 3-4: Fracture aperture for the three validation cases

The elastoplastic model in Papanastasiou's work has a wider aperture near the injection point and a sharp drop in the aperture at 0.5 meters from the injection point followed by a mild aperture change to the fracture tip. The wide aperture

close to the injection point may be due to the initial 0.5 meter fracture used by Papanastasiou (1997b). Having an initial 0.5-meter-long fracture (without applying fluid pressure) prevents shearing and strain-hardening behavior in this area. This behavior is expected to occur when the fracture propagates from zero to 0.5 meters. The initial fracture length influences the fracture aperture profile near the injection point, while the aperture profile is correctly calculated in the propagation interval (Papanastasiou, 1997b). Papanastasiou (1997b) emphasizes that any comparison of the fracture profile should be done only within the propagation interval. Note that no initial fracture is used in the smeared hydraulic fracture model proposed in this research.

Despite using fracture energy regularization to resolve mesh dependency, some degree of mesh-size effect is still observed in the results. Part of this difference is due to the finite difference scheme used in FLAC (e.g., pore pressures are averaged at the center of the finite difference elements). Weill and Latil (1992) reported similar mesh dependencies due to the smearing of fracture permeability over coarse elements. Even though the results show some mesh dependency, reducing the mesh size shows a converging trend in the computational results. This convergence is more significant in the cases of the elastic model with the dynamic modulus and the elastoplastic model.

The net-pressure profiles inside the fracture are plotted in Fig. 3-5 where the fracture has propagated to 2.40 meters. Net pressure is defined as the fluid pressure inside the fracture minus the minimum in situ stress. The very narrow fracture aperture near the fracture tip induces a high-pressure drop in this area, which is more significant in the case of the elastic model with the dynamic modulus. The mesh dependency is still observed in the net-pressure profiles at the full propagation length. However, there is a good agreement between the results of the smeared fracture approach and the results of Papanastasiou's model (1997b). The smeared approach results tend to approach the results of Papanastasiou's model (1997b) when the mesh size is reduced.

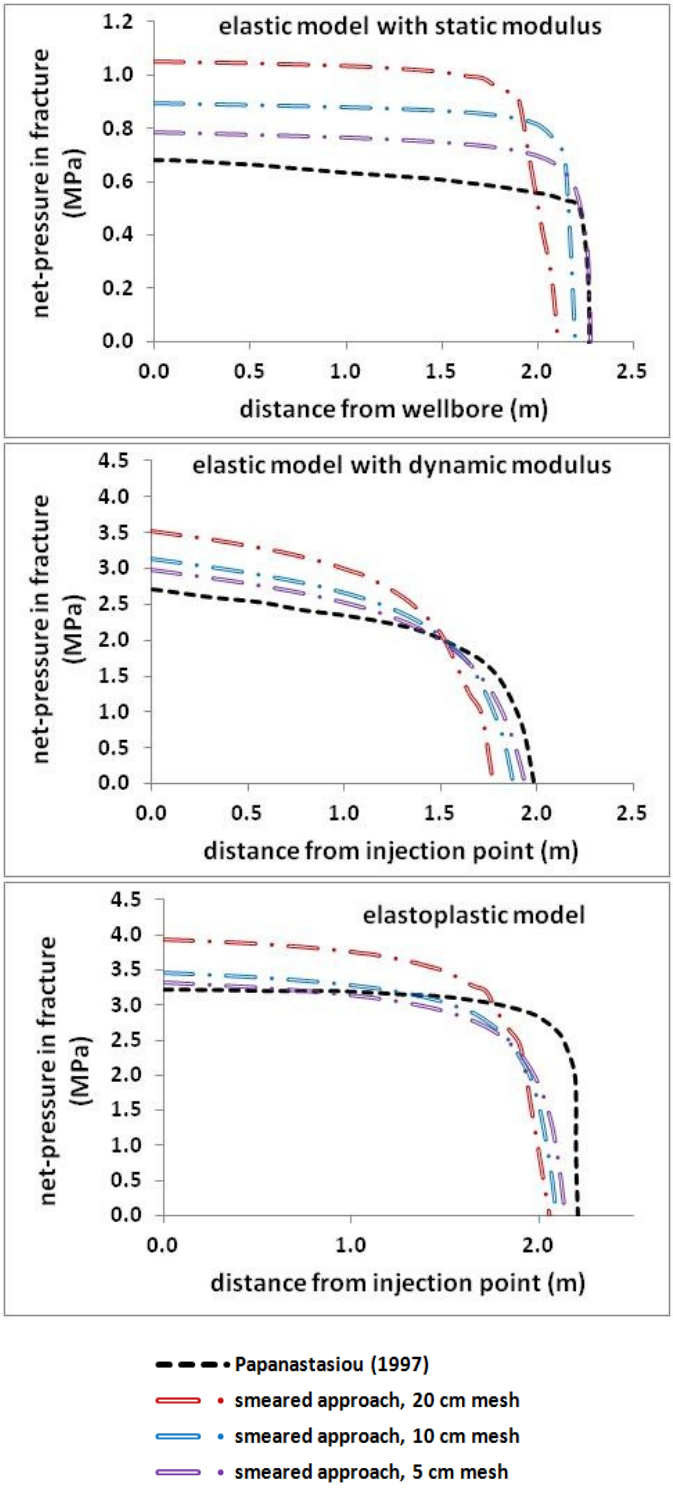

Fig. 3-5: Fracture net-pressure profile for the three validation cases

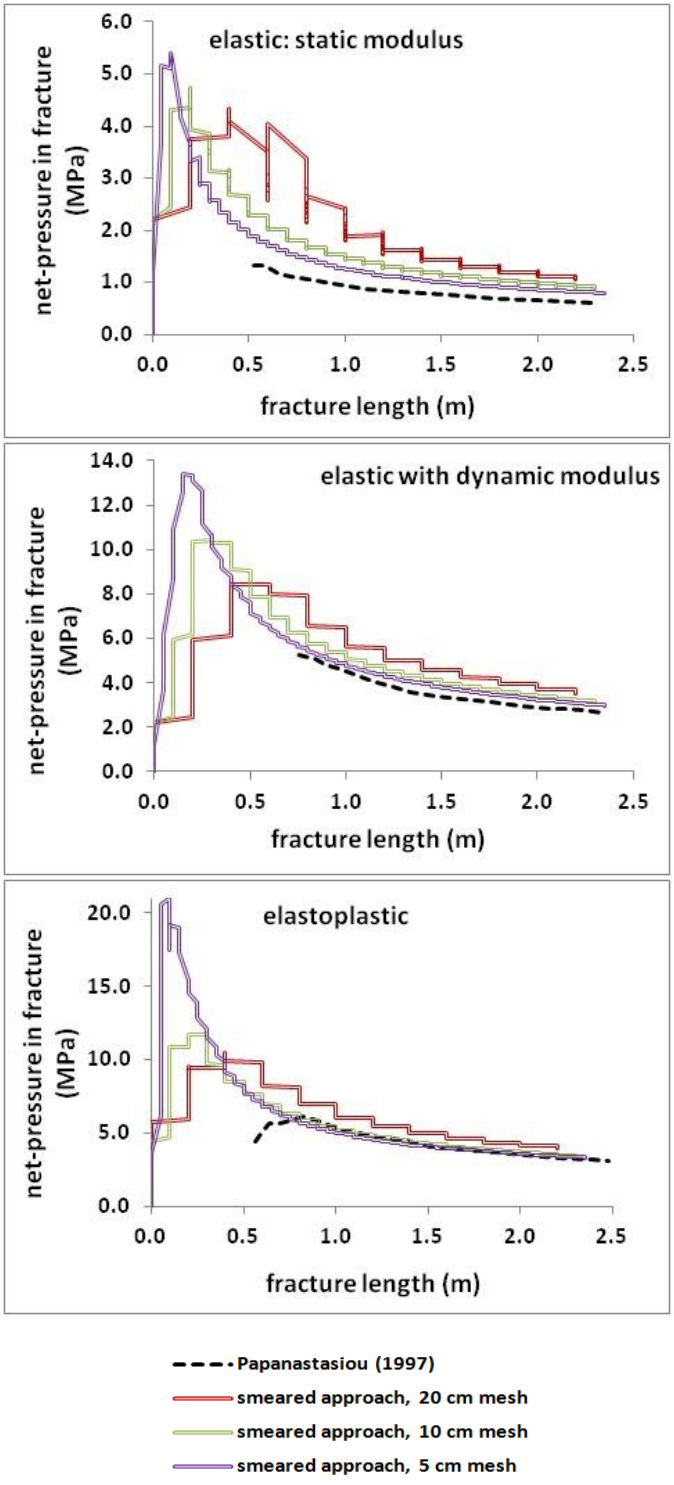

Fig. 3-6: Net pressure vs. fracture length for the three verification cases

For the three cases, fracture net pressure at the injection point versus fracture length is plotted in Fig. 3-6. The initiation-net pressures in the case of elastic models with both static and dynamic moduli are in the range of 2.45 to 3.70 MPa

for all three mesh sizes, while this value for the elastoplastic model lies in the range of 4.7 to 6.20 MPa. It can be concluded that the initiation pressure is significantly affected by the plastic behavior. This figure also shows that the predictions of the elastic model with the dynamic modulus are closer to those of the elastoplastic model; however, their mechanisms are different (Papanastasiou, 1997b). According to Papanastasiou (1997b), the large net pressure in the elastoplastic model is due to dissipated energy in the plastic zones. However, in the elastic model with the dynamic modulus, high net pressure is the result of a narrow aperture and a large pressure drop in this region.

For further propagation, the injection pressure reaches a maximum pressure in the range of 4.32 to 5.49 MPa for the static modulus case, and 8.34 to 13.34 MPa for the dynamic modulus case. These values for the elastoplastic model are 10.5 to 21 MPa. This indicates that the elastic modulus and elastoplastic behavior are determining factors for calculating breakdown pressure.

An inconsistency is seen in the graphs for the elastoplastic model where the fracture is between 0.5 to 0.75 m. Papanastasiou (1997b) had used a 0.5 meter initial fracture, while in our model, there is no need to devise an initial fracture. The inconsistency in the elastoplastic model appears to originate from the existence of this initial fracture, preventing plastic deformation and shear hardening at the initiating stage. Still, a reasonable agreement is observed in the results, especially for the small-size mesh.

In order to evaluate the effectiveness of the adopted regularization method, the results of the elastic model with the dynamic modulus, as well as those of the elastoplastic model, are compared with their un-regularized solutions. Even though the regularization has had little influence on the fracture aperture compared to the corresponding un-regularized cases (Fig. 3-7), it has affected the net fracturing pressure by about 0.5 MPa for all three mesh sizes, as shown in Fig. 3-8. It is clear that regularizing the fracturing energy is effective and produces results that are closer to those presented by Papanastasiou (1997b). The same trend is observed in both the elastic and elastoplastic models for all mesh sizes.

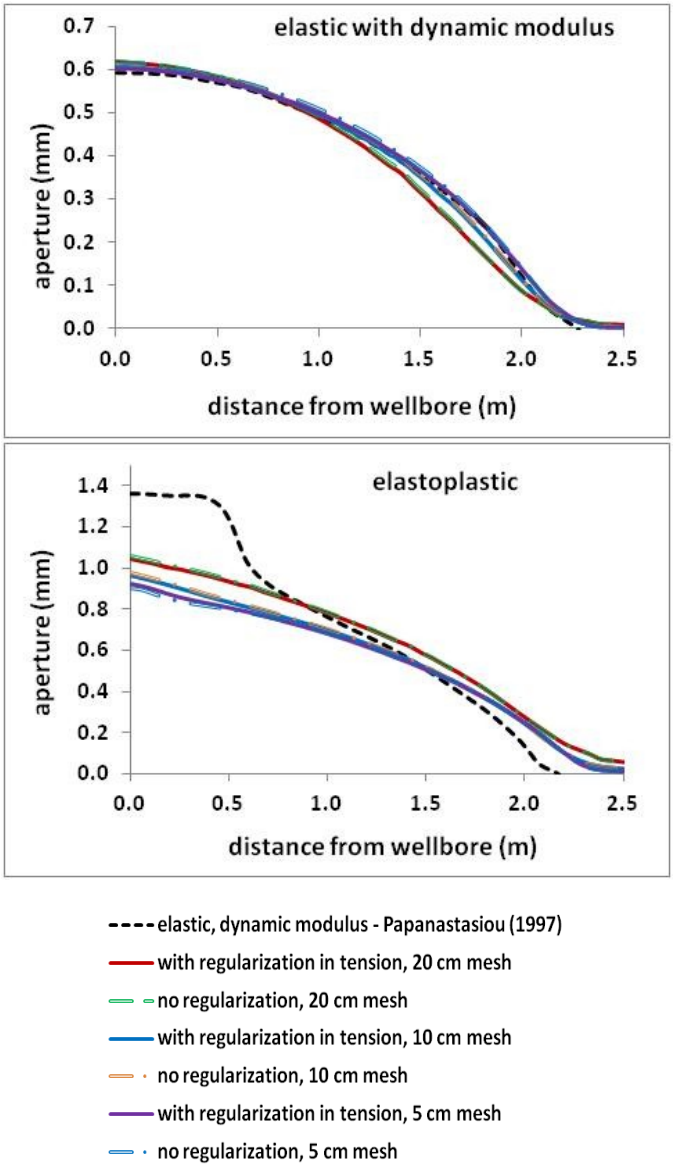

Fig. 3-7: Comparison of the fracture aperture for the regularized and un-regularized static models with the dynamic modulus as well as for the elastoplastic model

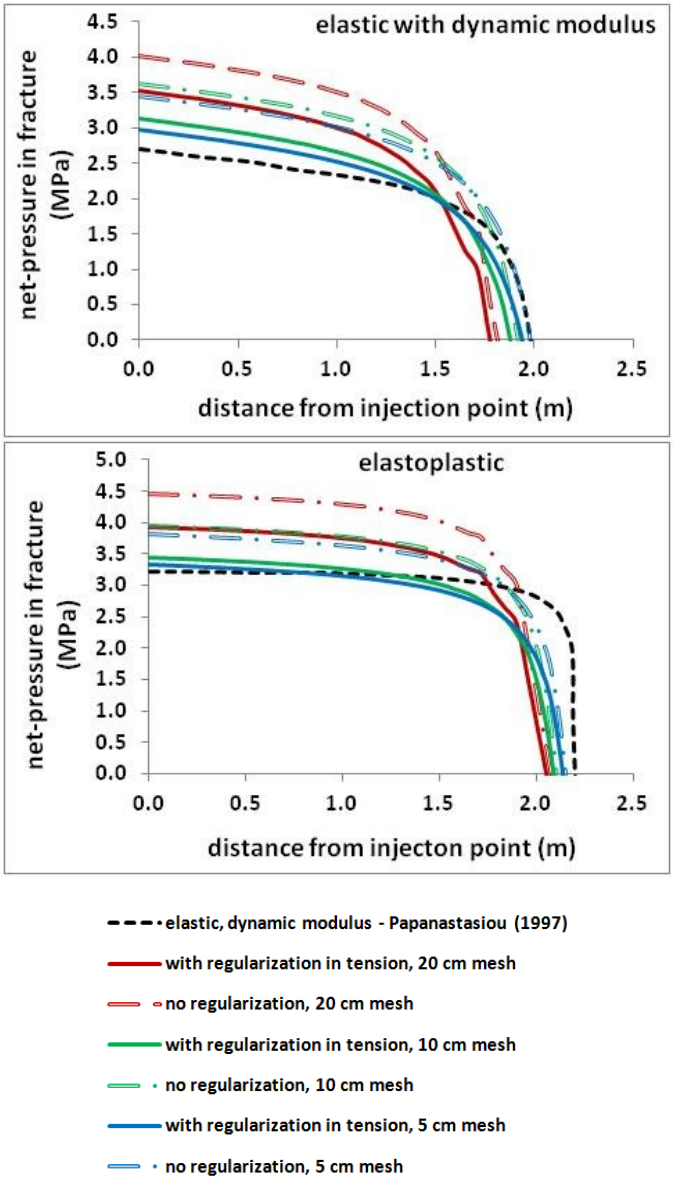

Fig. 3-8: Comparison of the net-pressure profile for the regularized and un-regularized static models with the dynamic modulus as well as for the elastoplastic model

3.5 Sensitivity Analysis

In this section, a sensitivity analysis is performed with respect to some parameters including the viscosity of the injecting fluid, tensile strength and the dilation angle of the rock to evaluate the influence of these parameters on the fracturing response of the rock. The elastoplastic model with a 20-cm mesh, 28-degres dilation angle, 0.5-MPa tensile strength and 100-cp fluid viscosity was

selected as the base case. Only one parameter was changed at a time in the sensitivity analysis.

3.5.1 Dilation Angle

Three dilation angles were selected for comparison: 0, 14 and 28 degrees. The latter is the base case discussed in the previous sections. The results of the fracture aperture as well as the net fracturing pressure (both at full fracture propagation) are illustrated in Fig. 3-9 and Fig. 3-10.

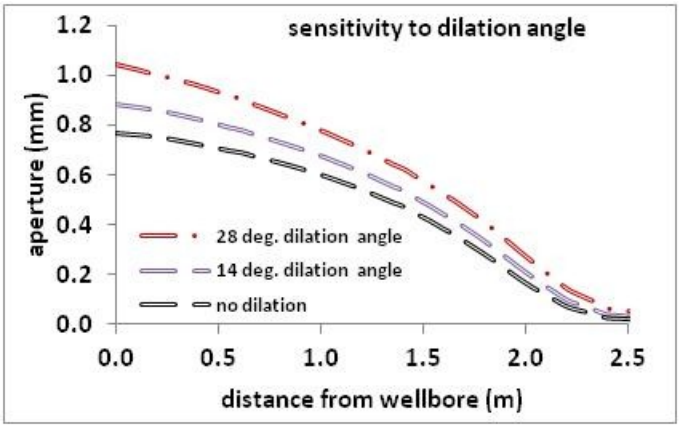

Fig. 3-9: Fracture aperture, sensitivity to the dilation angle of the rock in the elastoplastic model

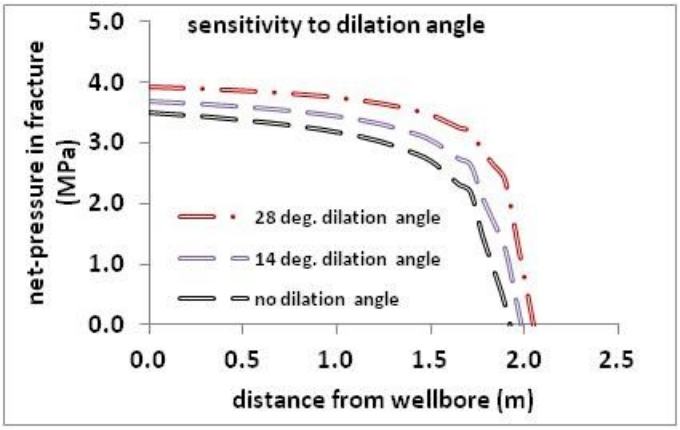

Fig. 3-10: Net-pressure at full propagation, sensitivity to the dilation angle of the rock in the elastoplastic model

In these figures, the wider fracture corresponds to the larger dilation since dilation increases the volume of the sheared rock and eventually the local stresses around the fracture. Consequently, larger pressure is needed at the fracture tip for further propagation. Such larger pressure leads to a wider aperture. Fig. 3-10

shows that maximum net pressure for the 28-degree dilation rock is almost 0.5 MPa more than that for the non-dilative rock (dilation angle of zero).

The shear (plastic) zones of the three cases are illustrated in Fig. 3-11. The model with the larger dilation angle (dilation of 28 deg.) shows a larger sheared zone. A larger shear zone results in more enhancements in the magnitudes of local stresses and therefore larger fracture propagation pressure.

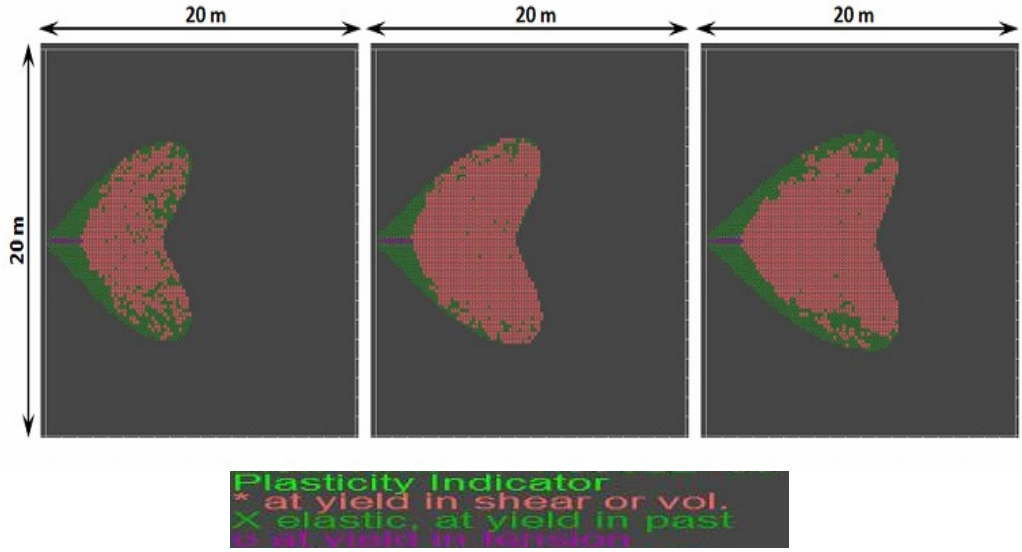

Fig. 3-11: Comparison of tensile and shear zones in the three dilation angle cases

3.5.2 Tensile Strength

Fig. 3-12 and Fig. 3-13 illustrate the fracture aperture and net-pressure profile for four different tensile strengths. Note that the apertures associated with the tensile strength of 0 and 0.5 MPa overlapping and the corresponding net pressures at the final propagation length are only 0.13 MPa different for these two cases. The maximum net pressure variation is 0.2 MPa, corresponding to the tensile strength variation from 1.0 to 1.5 MPa. It is argued that there is more shearing involved in the case of the higher tensile strength, which requires higher fluid pressure to be built up to induce the fracture. Higher pressure causes a larger shear zone which in turn increases stresses locally around the injection point as well as the fracture.

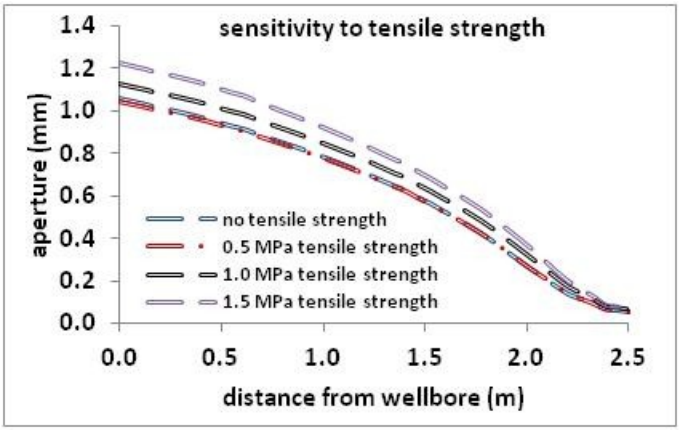

Fig. 3-12: Fracture aperture, sensitivity to tensile strength of the rock in the elastoplastic model

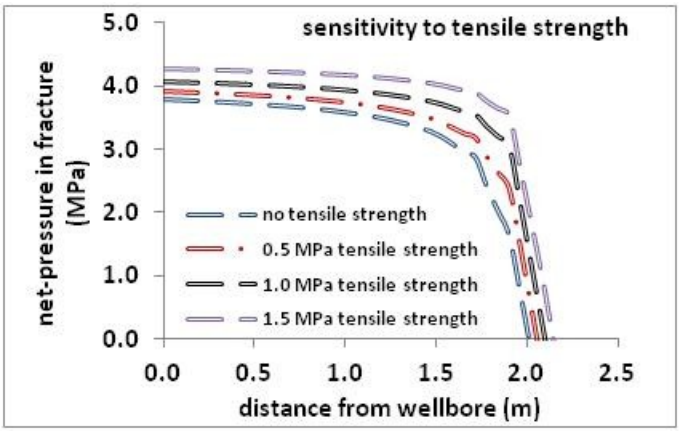

Fig. 3-13: Net pressure at full propagation, sensitivity to tensile strength of the rock in the elastoplastic model

3.5.3 Fluid Viscosity

Fig. 3-14 demonstrates the fracture aperture for the three fluid viscosities used for the sensitivity analysis. The fracture aperture is the same for fluid viscosities of 1 and 10 cp. However, the 100-cp fluid creates a wider fracture. This result is expected since larger pressure is needed for injecting a more viscous fluid and the larger pressure in turn results in a wider fracture. As shown in Fig. 3-15, the maximum net pressure for the two lower viscosities is only 0.2 MPa different while this difference for the two higher viscosity cases is 0.8 MPa. The pressure drop inside the fracture (near the tip area) is larger for the more viscous fluid.

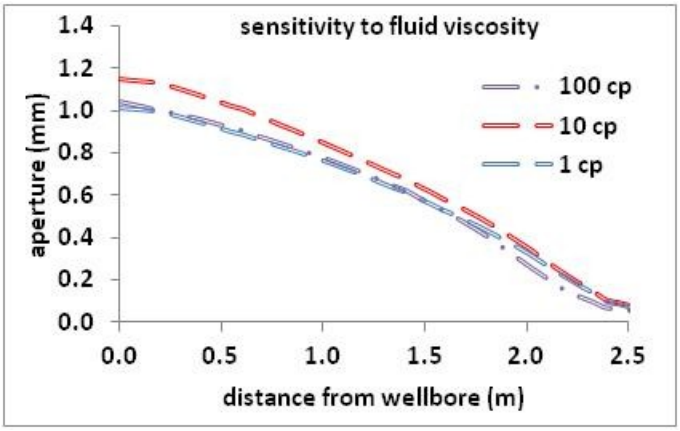

Fig. 3-14: Fracture aperture, sensitivity to fluid viscosity in the elastoplastic model

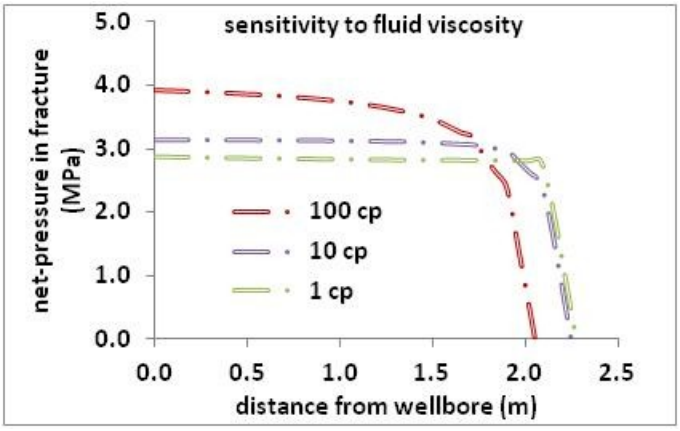

Fig. 3-15: Net-pressure at full propagation, sensitivity to fluid viscosity in the elastoplastic model

3.6 Summary and Conclusion

The smeared fracture approach was employed to develop a hydraulic fracture model. The modeling scheme was verified against published numerical results for tensile fracture. The results indicate that the smeared fracture approach can properly simulate the tensile hydraulic fracturing process.

The fracture energy regularization method was applied to ensure that the energy dissipated during fracture propagation was mesh-size independent. Despite that, some mesh dependency was still observed. There are several possible explanations: the need for different mesh sizes to have different volumes of fluid to increase the pressure to the fracturing level; the finite difference scheme employed in FLAC; and the truncation error in the calculations. An examination

of the fracture energy regularization method showed that when used in the numerical continuum model, it could reduce the computations' mesh-dependency.

For the specific material properties, the results indicated that larger dilation necessitated a larger injection pressure, which in turn led to a wider fracture. Further, the fracturing pressure was only modestly sensitive to the tensile strength of the rock and the viscosity of the injecting fluid.

Chapter 4: Smeared Modeling of Hydraulic Fracturing in Cohesionless Sand: Validation against Laboratory Experiments

This chapter presents the validation of the developed model against a large-scale hydraulic fracturing experiment performed on a highly permeable cohesionless sand (Golder Associates Ltd., 1992; Pak, 1997).

Both matrix and fracture flow are considered in this model. Tensile and shear failure and their fluid flow are simulated. To capture the permeability evolution, the cubic law and Touhidi-Baghini's shear-permeability equation are used to model flow in a tensile fracture and shear failure, respectively. In addition, the fracture energy regularization method is used to reduce the mesh size-dependency of the energy dissipated during fracture propagation.

4.1 The Hydraulic Fracture Experiments

Between April 1990 and July 1994, Golder Associates Ltd. carried out three phases of what? with the objective of better understanding the mechanisms involved in hydraulic fracturing initiation and propagation in uncemented oil sands (Pak, 1997). The project was funded jointly by the Canada Center for Mineral and Energy Technology (CANMET), Alberta Oil Sands Technology and Research Authority (AOSTRA), Shell Canada Ltd., Esso Resources Canada Ltd., Imperial Oil Resources Canada Ltd., Mobile Oil Canada, Japan Canada Oil Sands Ltd. (Phase 3) and Golder Associates Ltd.

According to Golder (Golder Associates Ltd., 1992) and Pak (Pak, 1997), the laboratory testing was designed to determine the effect of the fluid injection rate on fracture propagation. As schematically depicted in Fig. 4-1, a large-scale triaxial stress chamber capable of containing samples one meter high and 1.4 meters in diameter was utilized for the experiments. Quartz sand was used to construct the sand pack sample. Invert liquid sugar was used as the host fluid and injecting fluid. It was dyed for injection to distinguish it from the host fluid after

the sample was excavated at the end of the test. A steel pipe (outer diameter = 33.5 mm, inner diameter = 25.4 mm) was used as the injection well and was perforated at mid-sample height over an interval of 50 millimeters in eight rows of 3.5-mm diameter holes. In these experiments, the lateral and axial (vertical) stresses could be applied independently (Pak, 1997).

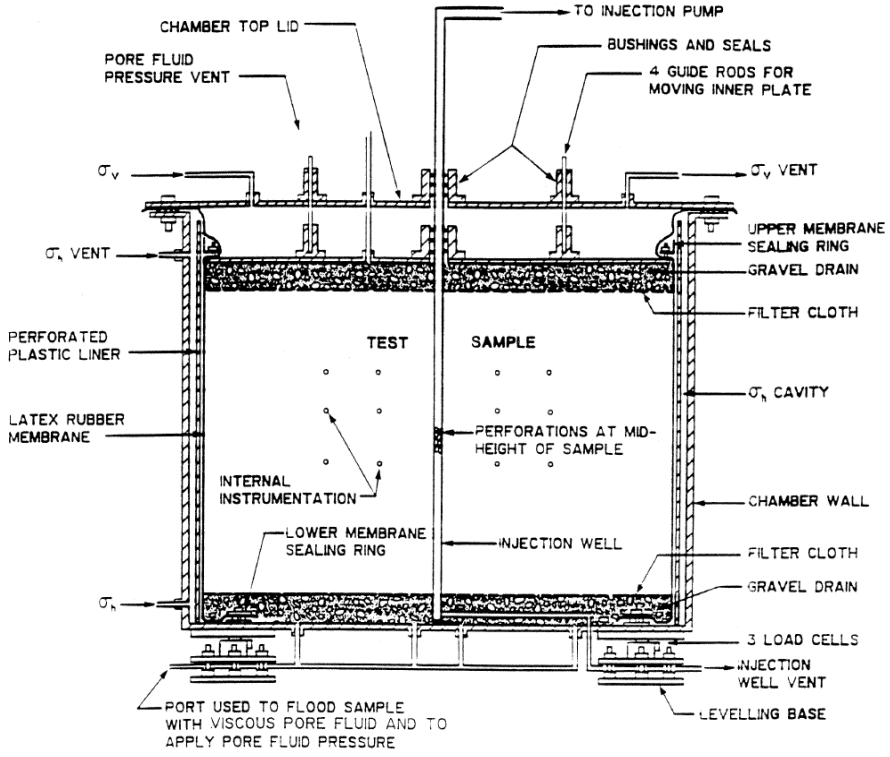

Fig. 4-1: Schematic cross section of the large-scale triaxial chamber used for a hydraulic fracture experiment (Pak, 1997)

4.1.1 Sand Pack Material

According to Golder (Golder Associates Ltd., 1992), Lane Mountain quartz sand was used for laboratory experiments. The quartz sand behaved similar to oil sands in terms of high dilatancy and post-peak softening in triaxial compression tests at low effective confining stress. Small-scale laboratory testing provided flow and mechanical characteristics of the sand. The average grain diameter (D_{50}) of Lane Mountain sand was 0.07 mm, and its absolute permeability was 4.48 x 10^{-12} m^2. The invert liquid sugar had a viscosity of 1.6 Pa.sec, which could be reduced by adding water (adding 5% water reduced the viscosity to 1.49 Pa.sec).

In addition to being the injection fluid, invert liquid sugar was also used as the saturating fluid, resulting in a single-phase flow (Pak, 1997).

4.1.2 Testing Procedure

To study the effect of the fluid injection rate on fracture propagation, fluid injection rates were changed from 0.4 to 200 ml/sec, and 200 ml of fluid was injected in 8.3 sec (injection rate of 30 ml/sec) (Pak, 1997).

First, the injection liner was installed, and the instrumentations for measuring sand deformation and pore pressure variations were suspended at a distance of one quarter of the sample radius from the wellbore at three specific levels in the sample: 100 and 250 millimeters above the injection level (levels 1 and 2, respectively) and 100 millimeters below (Level 3). At each monitoring level, two piezometers were installed at different angular positions: 90-1 and 270-1 at Level 1; 120-2 and 300-2 at Level 2; and 60-3 and 240-3 at Level 3 (the first number indicates the angular position, and the second number represents the monitoring level). Fig. 4-2 illustrates the layout of the instruments. The samples were prepared by pluviating dry sand from a hopper (with a diameter equal to that of the sample for the one-dimensional pluviation condition) right above the chamber (Pak, 1997).

Lateral and axial stresses of 600 and 400 kPa, respectively, were applied on the sample. The top and bottom of the chamber were connected to a pump, allowing a constant pore pressure of 200 kPa to ensure the full saturation of the sample (Pak, 1997).

At the end of the tests, the sample was excavated in horizontal lifts (in 1.5 to 3.0 cm intervals), and the locations of the dye on the surface were marked with black strings. A photograph of the excavated surface was taken with a camera located right above the sample. By repeating this procedure for each excavation and by digitizing the photographs, a 3D fracture pattern was prepared (Pak, 1997).

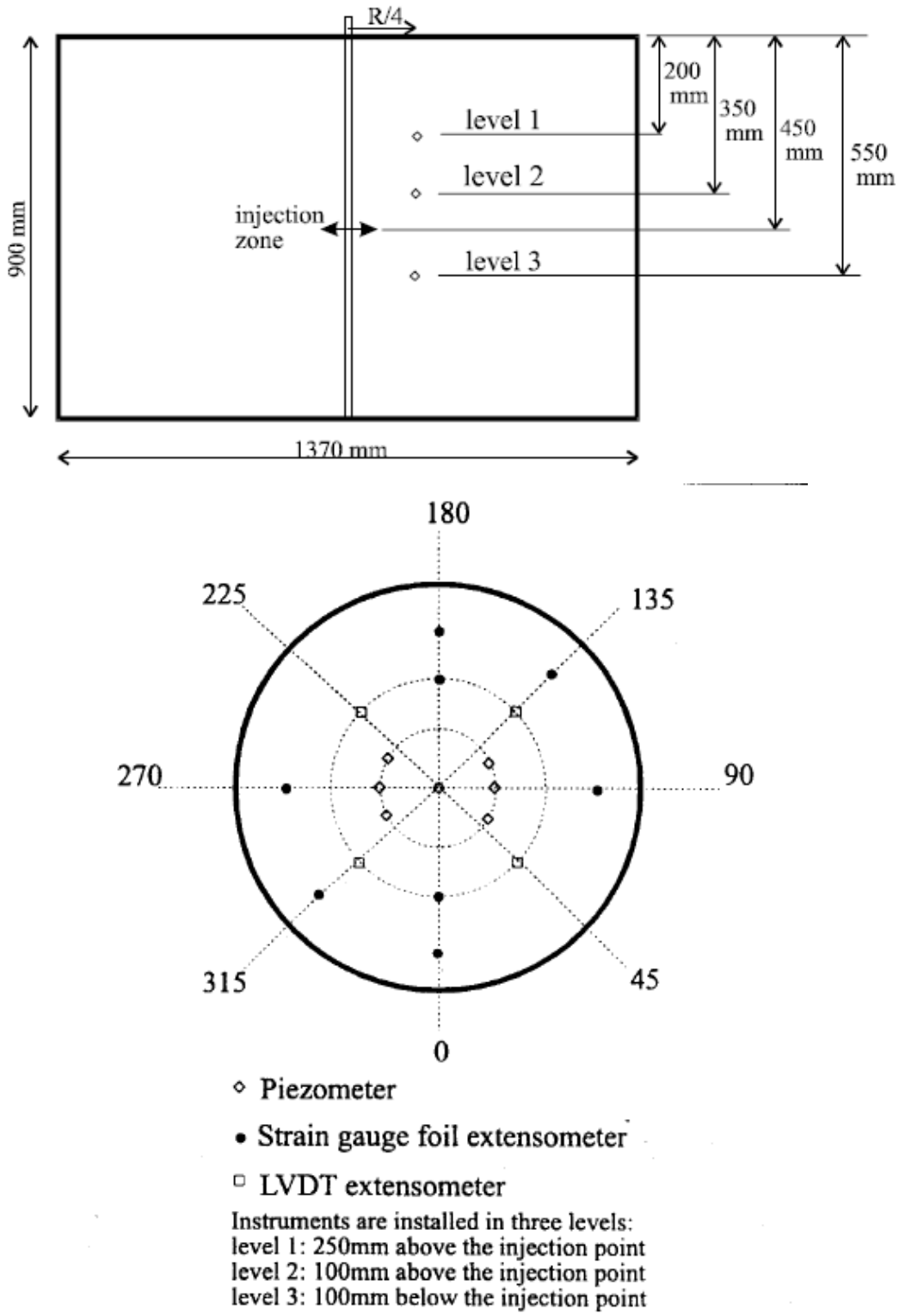

Fig. 4-2: Location of the piezometers for test No. 4 of Phase II of the experiments (Pak, 1997)

4.1.3 Results of the experiments

The experimental results showed evidence of shear failure in the sample for all injection rates, while no dominant fracture plane was observed. The dye pattern shown in Fig. 4-3 and the observed fractures indicated sand dilation in the sample. The dilation and the expansion constrained by the surrounding material caused a large increase in the local effective stresses. Consequently, the large injection pressure (which was much larger than the initial confining stress) was balanced by large local stresses in the sand matrix and prevented the development of tensile fractures (Pak, 1997).

Pore pressure measurements are presented in the following sections together with the numerical results. The deformation data were not available in the report.

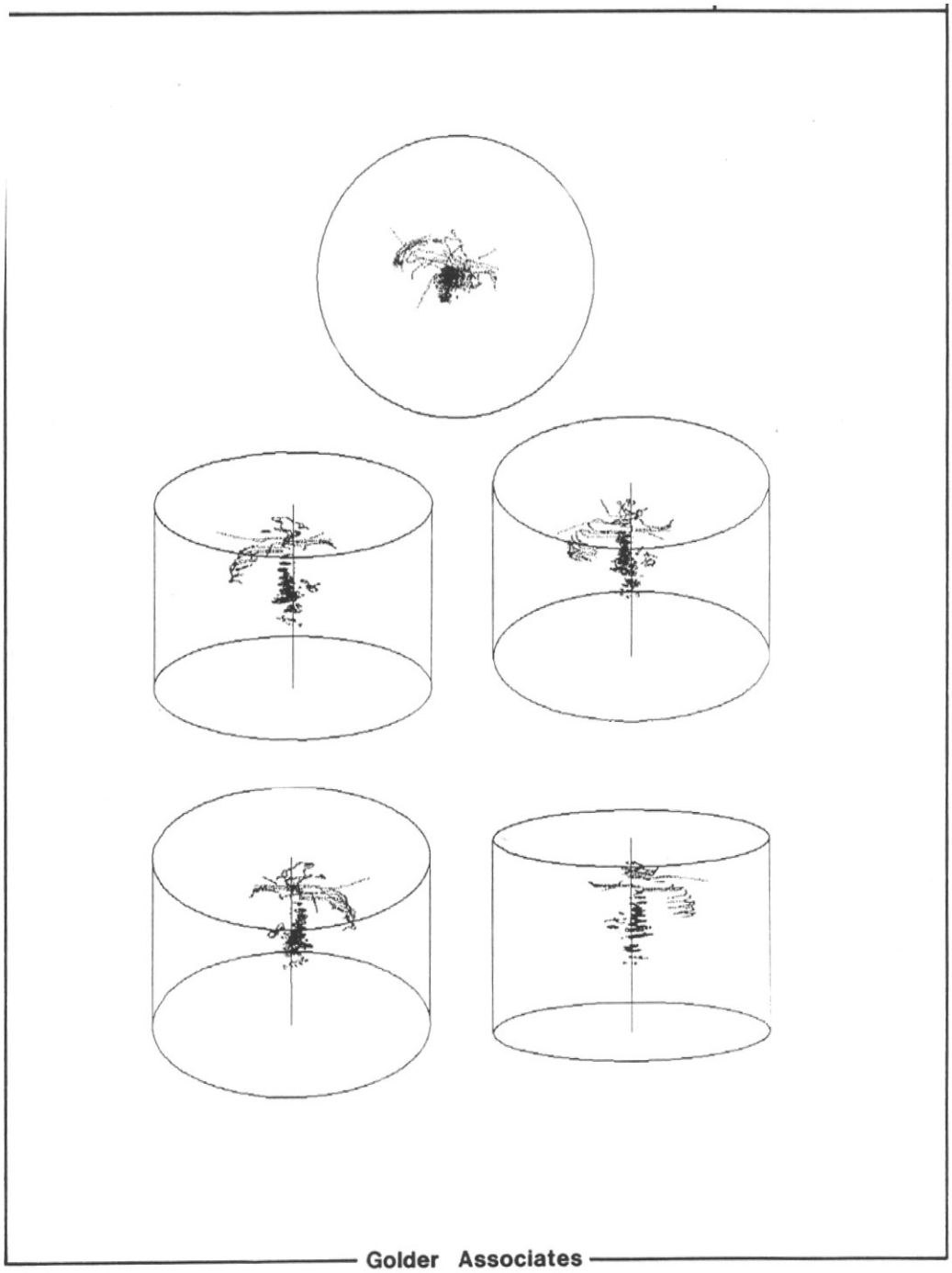

Fig. 4-3: Pattern of fluorescent dye in the sample (Pak, 1997)

4.2 Model Formulation

4.2.1 Material Constitutive Model

A linear Mohr-Coulomb model combined with strain softening was implemented in the model. The yield surfaces can be expressed in the following form (Nouri et al., 2009; Jafarpour et al., 2012).

$$F = T - (q + P)\mu = 0, \quad (4\text{-}1)$$

where P is the mean effective stress, and T is the square root of the second invariant of the deviatoric stress tensor in an axisymmetric state of stress (as in a triaxial compression experiment).

4.2.2 Smeared Tensile Fracture Flow Model

For fluid flow in a smeared tensile fracture, a slightly modified version of the procedure proposed by Ji (2008) and Ji et al. (2009) was used by implementing the tensile strain of the fractured element instead of the fracture aperture (Taghipoor et al., 2013), as shown below.

$$PM = 1 + \frac{1}{12 F_{rough} k_m} \varepsilon_T{}^3 t^2, \quad (4\text{-}2)$$

where ε_T is the tensile strain in the element, t is the equivalent element thickness in the direction of tensile strain, F_{rough} is fracture wall roughness coefficient, and k_m is the matrix permeability.

In the numerical model developed for this chapter, the permeability multiplier PM is calculated when a tensile fracture is detected in an element. This multiplier is applied to the permeability in the fracture direction, while the permeability in the direction normal to the fracture remains unchanged or follows the shear permeability criteria (described in the following section) if shear failure has been detected. This orthotropic permeability tensor is then rotated back to the global coordinate system, resulting in the anisotropic permeability tensor for the fractured element.

4.2.3 Smeared Shear Failure Flow Model

Touhidi-Baghini's model with different B values in horizontal and vertical directions is used to describe the shear permeability enhancement in the developed hydraulic fracture model in this chapter.

$$Ln\frac{k}{k_0}=\frac{B}{\phi_0}\varepsilon_v, \quad \text{(4-3)}$$

where k and k_0 are the evolved and initial permeabilities of an element, ε_v is the volumetric strain and B is the rate at which permeability evolves as a function of the volumetric strain variance.

Touhidi-Baghini's model was further validated against permeability measurements in triaxial compression tests of a weakly consolidated sandstone in the elastic compression range. These results are in Appendix A.

4.2.4 Fluid Flow Model

Darcy's law for fluid flow in porous media is used to solve the flow in the intact matrix as well as a tensile fracture and shear failure:

$$q_i=-\frac{k_{ij}}{\mu}\frac{\partial}{\partial x_j}\left(P-\rho_f g_k x_k\right), \quad \text{(4-4)}$$

where q_i is the specific discharge vector, k_{ij} is the permeability, μ is the fluid viscosity, P is the fluid pressure, ρ_f is the mass density of the fluid, g_k (k = 1 and 2) are the two components of the gravity acceleration vector (i, j = 1 and 2 are indices for two dimensional analysis).

In the developed model, porosity, permeability and pore pressure are the variables that are exchanged between the flow and the geomechanics module in a sequentially coupled manner. For each time step, the fluid flow module sends the calculated pore pressures to the geomechanics module. In the geomechanics module, pore pressures are updated and the corresponding stresses/deformations are calculated. Porosities and permeabilities are then updated based on the updated strains (the cubic law for tensile fracture permeability and Touhidi-Baghini equation for shear permeability), which are then sent back to the fluid

flow module. This process continues until solutions converge for the time step. Tensile fracture width is a solution-dependent parameter and is calculated and updated in each time step based on nodal displacements. Fracture energy regularization (described previously in Chapter 3) is also implemented to reduce the mesh-size impact.

4.3 Numerical Model Specification

FLAC software (Itasca Consulting Group Inc., 2011) was used to simulate the experiment. The flow and the stress-strain solutions were fully coupled in FLAC. The sample was cylindrical, the wellbore was at the center of the sample, the vertical stress was applied uniformly to the top boundary, and the confining stress was also uniformly applied to the surrounding surface of the sample. As such, the hydraulic fracture experiment was simulated in an axisymmetric configuration with the axis of the wellbore as the line of symmetry.

4.3.1 Model and grid size

Fig. 4-2 shows the axisymmetric model section with the sample dimensions. As illustrated in Fig. 4-4, a non-uniform grid was used for the numerical meshing. Three different grid sizes (9.5, 11 and 12.5 mm) were used in the perforation area to evaluate possible mesh dependency of the results. The model with the finest mesh is considered the base case to study how sensitive the numerical results are to some of the input parameters.

4.3.2 Initial and Boundary Condition

Normal stresses of 600 and 400 kPa were applied to the horizontal and vertical boundaries, respectively, in equilibrium with the same amounts of initial stresses. The bottom boundary and the left boundary (the liner) were fixed against displacement in the normal direction, as depicted in Fig. 4-2.

The injection was applied to the perforation interval at a constant injection rate of 30 ml/sec. Every element was checked for tensile fracturing and shear failure during the solution. New permeability of tensile and shear failure in the corresponding blocks was calculated using Eq. (3-1) and (2-34), respectively.

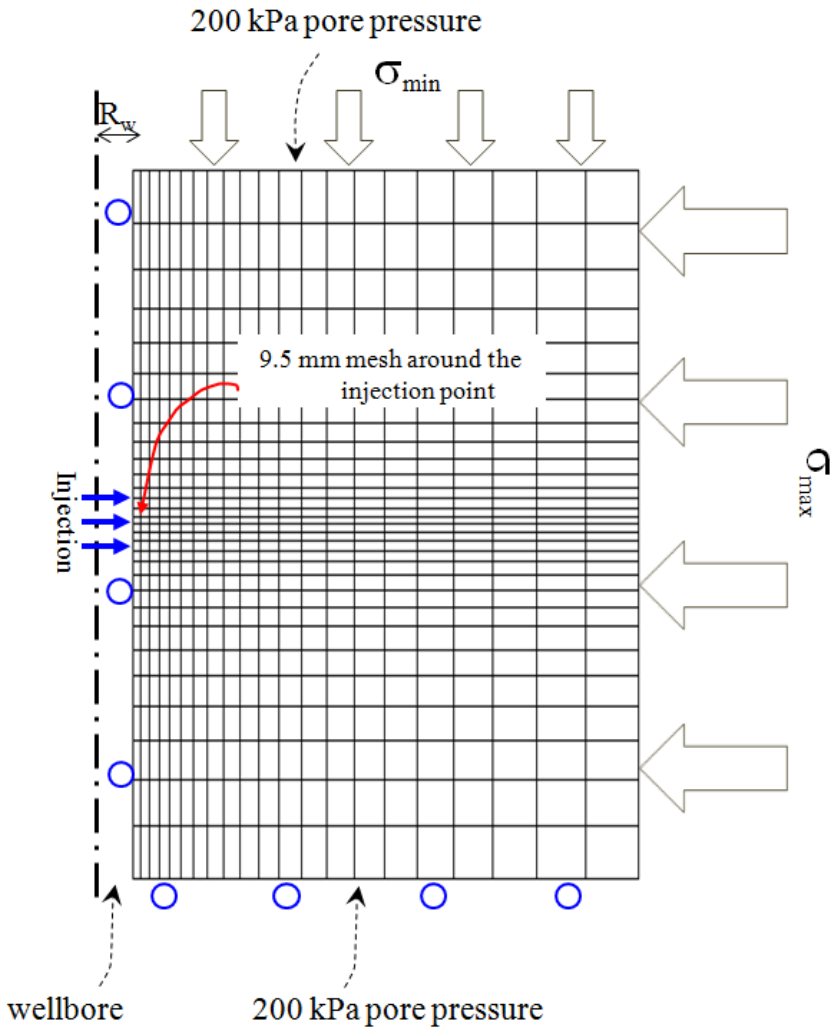

Fig. 4-4: Finite difference mesh and the boundary conditions

4.3.3 Material properties

All material properties in this section were obtained from Golder (Golder Associates Ltd., 1992) and Pak (Pak, 1997). The initial porosity and the absolute permeability of the sample were 0.48 and 4.48 x 10^{-12} m^2 (4.54 Darcies), respectively. Fluid compressibility was 0.3 x 10^{-5} kPa^{-1}. The elastic modulus and the Poisson ratio were measured as 41.05 MPa and 0.25, respectively. The sample was cohesionless with no tensile strength. Based on drained triaxial tests performed on dense Lane Mountain sand, the internal friction angle of the sand was 38^o at peak strength, which reduced linearly to 30^o with the accumulation of the equivalent plastic strain. The dilation angle was also reported to be 38 degrees at peak strength, dropping linearly to zero (assumption) at full degradation

(Golder Associates Ltd., 1992). The variations of the friction and dilation angles with plastic shearing strain are illustrated in Fig. 4-5.

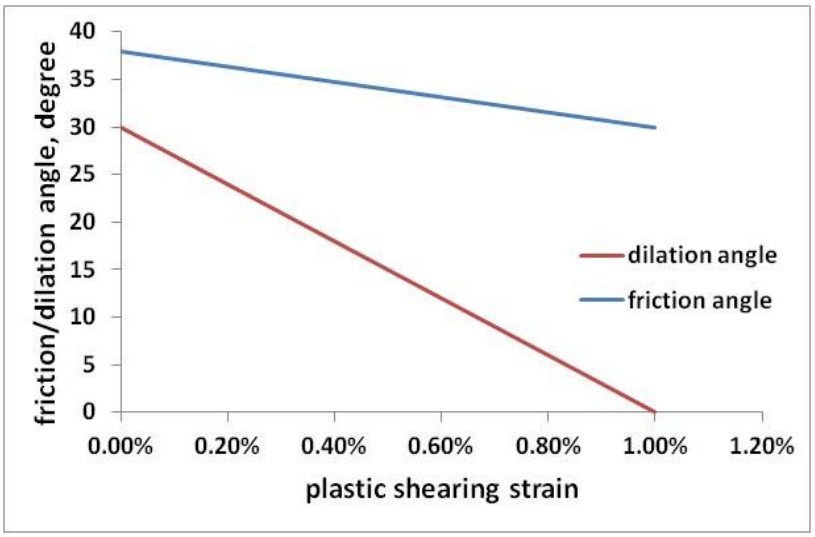

Fig. 4-5: Variation of the friction and dilation angles with shearing plastic strain

4.4 Validation Results

In this section, the numerical results are compared with the experiments. This is done by comparing the numerical pore pressures at the monitoring points with the pressures measured in the experiment. The sheared zone will also be qualitatively compared.

4.4.1 Calibration of the B Values

Different values were used for the B parameter, Eq. 2-34, in different directions to obtain a value that best matched the experiment.

Fig. 4-6 demonstrates the pore pressure at the injection point for several trials for B values in the vertical and horizontal directions. As can be seen, the best match corresponds to $B_h = 45$ and $B_v = 25$. A reasonable match is obtained for the pore pressure response at this point, and the differences could be associated with the general non-symmetric geometry of the shear fractures in the sample (Fig. 4-3) versus the symmetric geometry of shear failure in the numerical model.

The purpose of the developed hydraulic fracture model is to approximate discrete fractures with a smeared approach. The smeared approach may not

provide the flow mechanism in micro scale (grain size) but it is accurate in the element scale (an element here includes a cluster of grains) as elements are the smallest units for calculations. The discrepancies in some results (mainly in Fig. 4-9) could also be related to the heterogeneity of the sample, which forces failure to begin to form from natural defects. However, the developed model assumes a homogeneous material. In this case, a fracture is simulated as a diffused failure zone (symmetric around the axis of the specimen) in the numerical model.

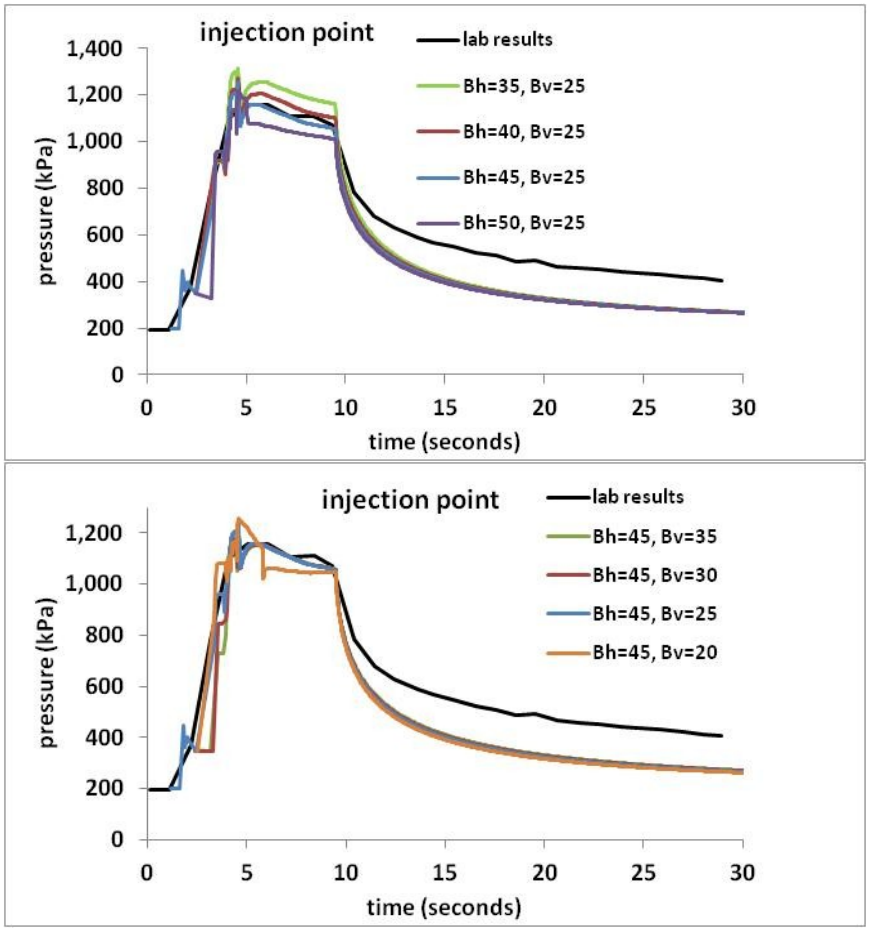

Fig. 4-6: Comparison of the calculated and measured pore pressure at the injection point

Fig. 4-7 shows a reasonable match between the measured and the calculated pressure response at Monitoring Point 90-1. The pressure profile of Point 270-1, however, is quite different than that of Point 90-1, indicating asymmetric responses at Level 1. This can be attributed to the asymmetric shear fracture development in the sample during the injection process, as is evident in Fig. 4-3.

It is likely that a shear band crossed the piezometer at 270-1 and increased the pore pressure at that point. Since the numerical model in an axisymmetric configuration did not make it possible to capture the asymmetric shear bands, the pore pressure at Point 270-1 was assessed to be the same as at Point 90-1. The pore pressure at Level 1 was insensitive to variations in parameters B_h and B_v, which could be related to the upward development of the shear fractures, which will be discussed later.

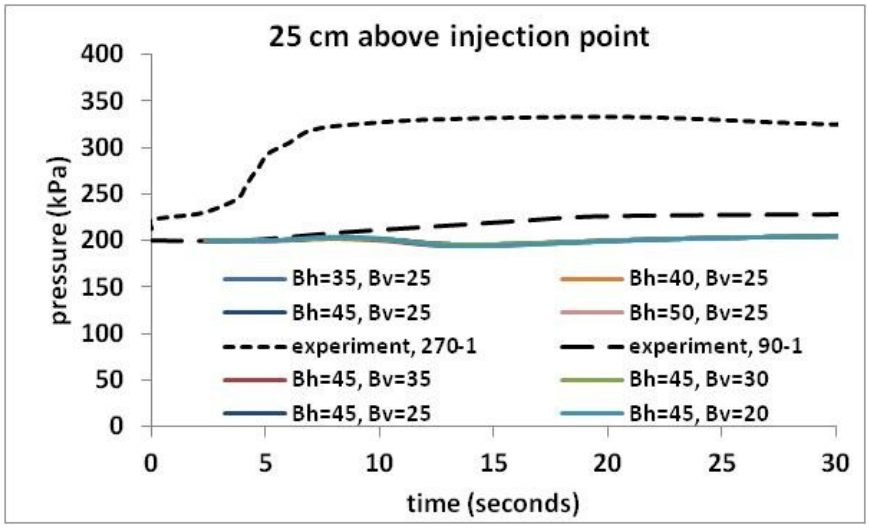

Fig. 4-7: Comparison of the calculated and measured pore pressure for the upper monitoring level (Level 1)

Fig. 4-8 shows a reasonable match between the measured and calculated pressures at different angular positions of Level 2. The pore pressure at this monitoring level is not influenced by variations in B_h and B_v. It is believed that the main reason for this is the upward trend of the shear failure zone and the localization of shear strains, which will be shown in Fig. 4-10.

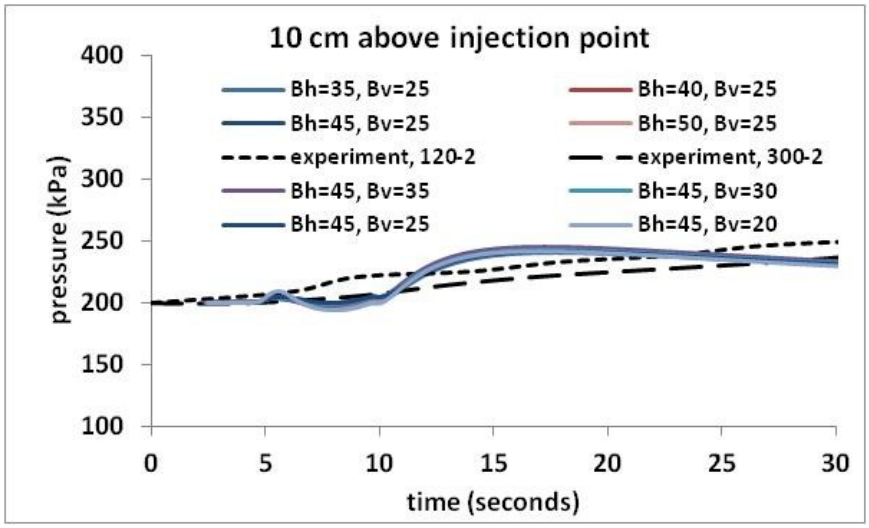

Fig. 4-8: Comparison of the calculated and measured pore pressure for the mid-monitoring level (Level 2)

Fig. 4-9 compares pore pressures monitored at Level 3. In the numerical model, the pressure drops to a low value of 150 kPa and then rises rapidly, followed by a slight decrease. As will be shown later, the mesh size is the major contributor in this response, as fewer fluctuations are obtained for the finer mesh.

The variation in the B_h parameter barely affected the results, while a high sensitivity to the B_v magnitude is evident at this monitoring level. The smaller B_v value (B_v = 20) not only reduced the fluctuation of the pore pressure, but also brought the pressure response closer to the measurements during the shut-in period.

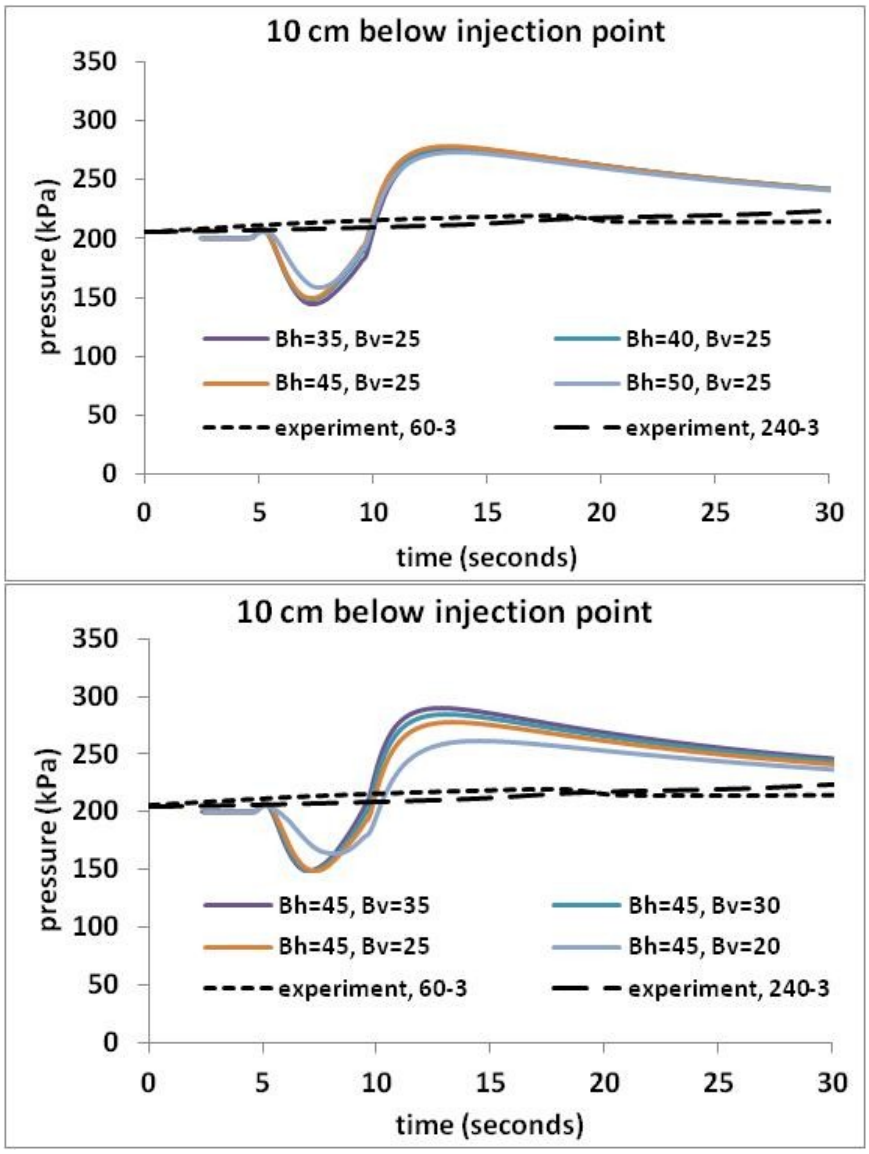

Fig. 4-9: Comparison of the calculated and measured pore pressures for the lower monitoring level (Level 3)

4.4.2 Shear and Tensile Failure Zones

As the sample does not have any tensile strength, a (diffused) tensile failure is more expected than a localized tensile fracture. Fig. 4-10 indicates a very small tensile-failure zone (less than 2 cm) near the perforations with B_h = 45 and B_v = 25. Tensile failure zones of the same size were also obtained for other B_h and B_v values. In the final report of the experimental study, it was concluded that there was no evidence of a single dominant tensile parting or closely spaced distribution of fractures primarily normal to the initial minimum principal stress in any of the

fracture experiments (Pak, 1997). Permeability evolution due to shearing and the diffusion of pore pressure into the sample, low shear strength and the dilative behavior of the material are believed to be the main reasons that it was not possible to generate tensile fractures (Pak, 1997).

The shear failure zone and the plastic shear strains in Fig. 4-10 are almost evenly distributed around the injection point, but tend to move upward after some propagation into the sample. As a result, pore pressure diffusion tends to occur faster at the higher monitoring levels than at the lower ones.

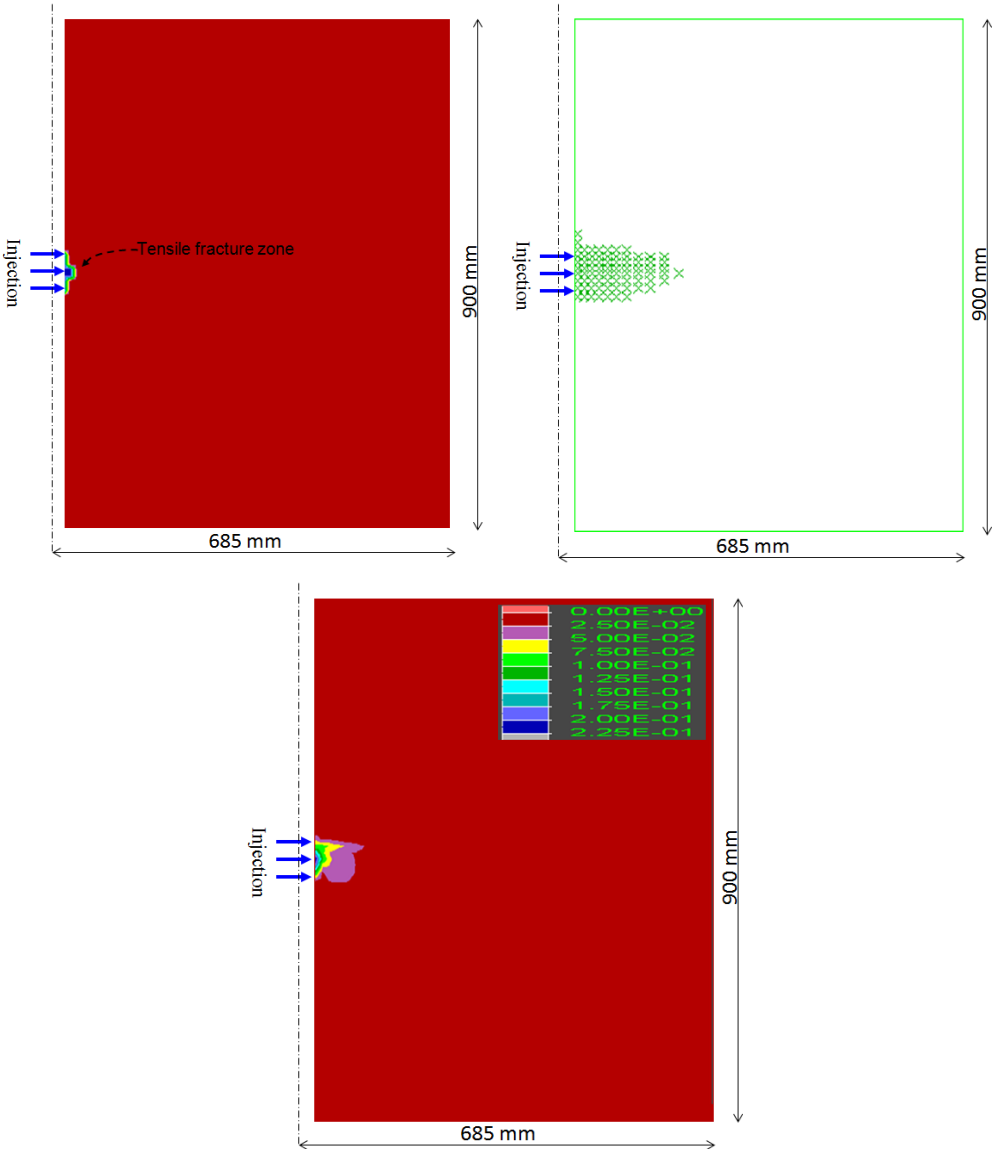

Fig. 4-10: The shear failure zone (top right), plastic shear strains (bottom) and the size of the tensile failure zone (top left) in the numerical model

It should be explained that the real flow boundary condition (in the experiment) at the injection interval is initially symmetric and eventually becomes asymmetrical. At the beginning of the experiment, the most likely asymmetrical parameter is the heterogeneity of the sample. Once injection starts, this natural heterogeneity forces more fluid flow through larger (more permeable) pores (at grain scale). Similarly, pore pressure builds up more quickly in tighter (less permeable) spots, causing fracture to begin from these points. As we don't have any information on the heterogeneity of the sample (and also it is out of the scope of the research), a homogeneous sample was assumed in the numerical model. In addition, fluid was injected over the perforation interval. In this case, there was no natural bias in permeability, and diffused failure was a more reasonable expectation.

Touhidi-Baghini's model, in the form of Eq. (2-34), was established based on flow experiments conducted during triaxial tests on cylindrical samples. Eq. (2-34) represents the overall permeability of the whole sample while being sheared (a defused shear zone including a discrete shear fracture embedded in a cylindrical sample). This shear permeability model (and other similar models) does not address a local permeability enhancement of localized shear fractures. Therefore, the equation is well-suited to the diffused failure and the associated permeability enhancements simulated here using the developed hydraulic fracture model.

4.4.3 Mesh size effect

Three mesh sizes of 9.5, 11 and 12.5 millimeters were used to simulate the hydraulic fracture experiment. The results for the three mesh sizes are illustrated in Fig. 4-11. Despite applying fracture energy regularization to the model, the pore pressure at the mid and lower monitoring levels was significantly affected by the selected mesh size. However, the results converge towards the experimental measurements for the finer mesh. The observed mesh dependency creates a need to examine the effectiveness of the fracture energy regularization method implemented here.

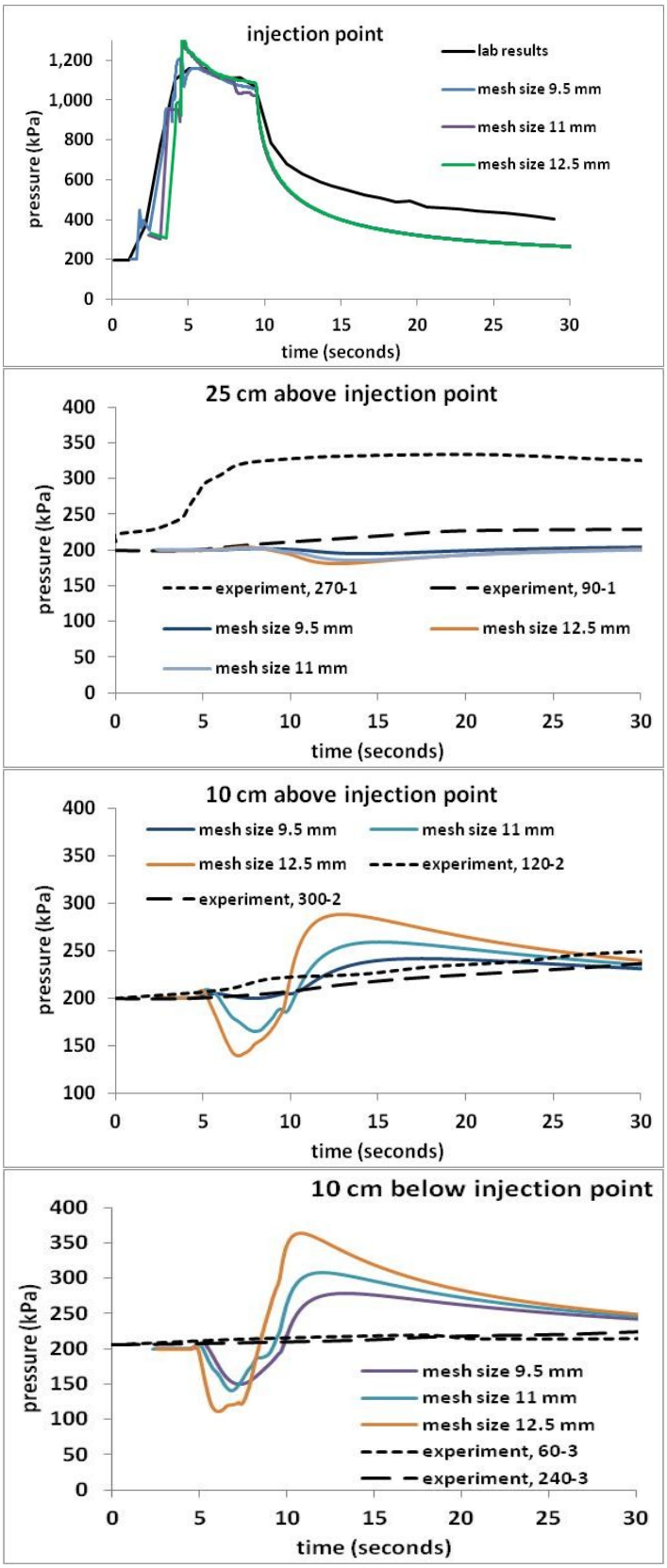

Fig. 4-11: Mesh sensitivity of the results

To evaluate the effectiveness of the fracture energy regularization method, the base model has been solved without regularization. As shown in Fig. 4-12, the application of the regularization method caused smaller pore pressure to build up at the injection point during the injection period, which is closer to the experimental results. However, no considerable influence was observed on the pore pressures calculated for all the monitoring points. Fig. 4-13 compares the degraded zone for the two models. This figure demonstrates a much larger degradation zone for the regularized model (larger than one-third of the diameter of the cylindrical sample), which is closer to the experimental outcome (Fig. 4-3) compared to that of the un-regularized model (which is limited to a very small zone surrounding the injection point).

It is therefore concluded that the observed mesh dependency in the results could possibly be due to the explicit finite difference scheme used in FLAC (e.g., pore pressure is averaged at the center of the finite difference elements). Similar mesh dependency had been described in the previous chapter in tensile fracture simulations in impermeable rock with the strain softening behavior under tension.

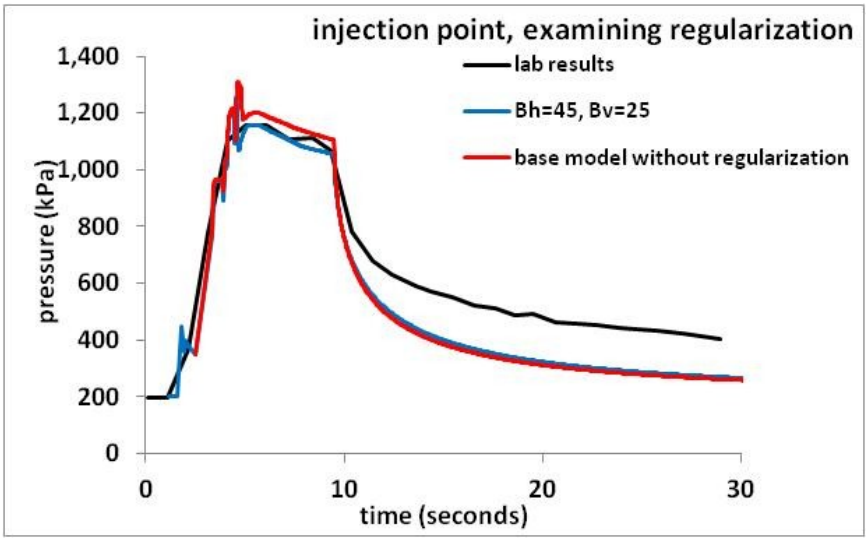

Fig. 4-12: Evaluating the effectiveness of fracture energy regularization

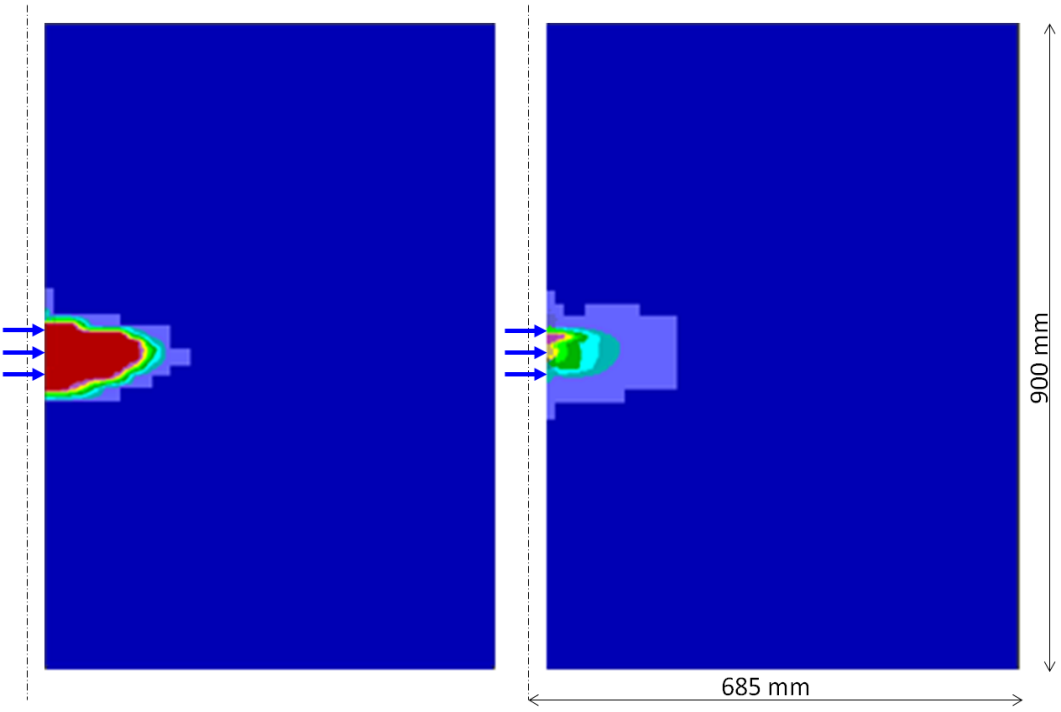

Fig. 4-13: Comparison of the degraded zone with and without fracture energy regularization. The red colour shows the fully degraded material

4.5 Summary and Conclusion

The smeared hydraulic fracture model developed in this research was validated against a hydraulic fracturing experiment in cohesionless sand. Reasonable agreement was obtained with the experimental results, especially during the injection period. The size of the tensile fracture zone was very limited, and it was found that permeability evolution due to shear dilation was the main contributing factor in the flow response.

Despite using the fracture energy regularization method, some mesh dependency was observed in the calculated pressures.

The fracturing pressure was found to be more than three times the initial minimum principal stress applied to the sample. One reason could be the high permeability and low shear strength of the material, which would cause the poroelasticity effects and dilative behavior to have a significant impact.

It is concluded that the smeared fracture approach can properly simulate the hydraulic fracturing process in cohesionless sands. This approach also makes it possible to simulate related mechanisms and processes such as shear failure and shear permeability evolution, which are involved in hydraulic fracturing.

Chapter 5: A Numerical Investigation of the Hydraulic Fracturing Mechanism in Oil Sands

5.1 Introduction

This chapter presents a numerical investigation of hydraulic fracturing in oil sands during cold water injection, taking into consideration aspects of both geomechanics and reservoir fluid flow. The smeared fracture approach was adopted to simulate tensile fractures and shear failure in the oil sands. Major features of this model include modeling poroelasticity and plasticity, matrix flow, shear failure and tensile fracturing with concomitant permeability enhancement (Touhidi-Baghini's shear permeability and the cubic law, respectively), saturation-dependent permeability, stress-dependent stiffness and gradual degradation of oil sands due to dilatant shear deformation.

The constitutive model used in the hydraulic fracture simulations is calibrated against a series of laboratory triaxial experiments. The hydraulic fracture model is also calibrated against a series of well tests to obtain representative reservoir petrophysical characteristics. The calibrated model is next utilized to simulate hydraulic fracturing in the oil sands using cold water injection. A series of sensitivity analyses is conducted to evaluate the sensitivity of the model to the numerical mesh size. Further sensitivity analyses are also performed with respect to reservoir and geomechanical parameters including apparent tensile strength and cohesion of the oil sands, magnitude of the minimum and maximum principal stress, absolute permeability and elastic modulus of the oil sands, ramp-up time and the calibration parameter in the shear permeability equation (B parameter), all of which are done to clarify the influence of these parameters on the fracturing response.

5.2 Model Formulation

5.2.1 Material Constitutive Model

A bilinear Mohr-Coulomb shear model combined with strain hardening/softening is implemented in the model to describe the shear strength of the material. The yield surfaces can be expressed in the following form (Nouri et al., 2009; Jafarpour et al., 2012):

$$F = T - (q + P)\mu = 0, \quad \text{(5-1)}$$

where P is the mean effective stress, and T is the square root of the second invariant of the deviatoric stress tensor in an axisymmetric state of stress (as in a triaxial compression experiment). P and T are defined as:

$$P = (\sigma'_z + 2\sigma'_r)/3, \quad \text{(5-2)}$$

$$T = |\sigma'_z - \sigma'_r|/\sqrt{3}, \quad \text{(5-3)}$$

and μ is the friction coefficient which is equal to tan(ϕ_σ). This parameter is related to the friction angle (ϕ_a) in the following form:

$$\tan\phi_\sigma = \frac{2\sqrt{3}Sin\phi_a}{3 - Sin\phi_a}, \quad \text{(5-4)}$$

This model has been calibrated against triaxial experiments. Further description of the model parameters and detailed calibration process is provided in Appendix B.

A cohesive constitutive model (Barenblatt, 1962) is used to calculate the tensile strength of the material. The rock is assumed to undergo linear softening under tension before fracturing (Fig. 5-1).

5.2.2 Smeared Tensile Fracture Flow Model

For fluid flow in a smeared tensile fracture, a slightly modified version of the procedure proposed by Ji (2008) and Ji et al. (2009) is used by implementing the tensile strain of the fractured element, Eq. (3-1), instead of the fracture aperture, as shown below.

$$PM = 1 + \frac{1}{12 F_{rough} k_m} \varepsilon_T{}^3 t^2 , \quad \text{(5-5)}$$

where ε_T is the tensile strain in the element, t is the equivalent element thickness in the direction of the tensile strain, F_{rough} is fracture wall roughness and k_m is matrix permeability.

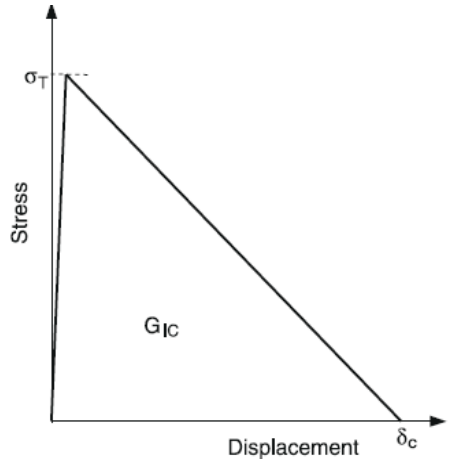

Fig. 5-1: Cohesive behavior of fracture (Papanastasiou, 1999)

Once a tensile fracture is detected in an element in any time step in the model, the permeability multiplier *PM* is calculated using the cubic law for the smeared fracture. This multiplier is applied to the permeability in the fracture direction, while the permeability in the direction normal to the fracture remains unchanged or follows the shear permeability criteria (which will be described in the following section) if shear failure has been detected. This orthotropic permeability tensor is then rotated back to the global coordinate system, resulting in the anisotropic permeability tensor for the fractured element.

5.2.3 Smeared Shear Failure Flow Model

Touhidi-Baghini's model in the form of Eq. (5-6) with different *B* values in horizontal and vertical directions is used to describe the shear permeability enhancement in the developed hydraulic fracture model in this chapter.

$$Ln \frac{k}{k_0} = \frac{B}{\phi_0} \varepsilon_v , \quad \text{(5-6)}$$

where k and k_0 are the evolved and initial permeability of the element, respectively, ε_v is volumetric strain and B is the rate at which permeability evolves as a function of volumetric strain variance.

Touhidi-Baghini's model was further validated against permeability measurements in triaxial compression tests of a weakly consolidated sandstone in the elastic compression range. This calibration can be found in Appendix A.

5.2.4 Fluid Flow Model

Darcy's law for fluid flow in porous media is used to solve the flow in the intact matrix, tensile fractures and shear failure:

$$q_i = -\frac{k_{ij}}{\mu}\frac{\partial}{\partial x_j}\left(P - \rho_f g_k x_k\right), \quad \text{(5-7)}$$

where q_i is the specific discharge vector, k_{ij} is the permeability, μ is the fluid viscosity, P is the fluid pressure, ρ_f is the mass density of the fluid, g_k, k = 1, 2, are the two components of the gravity acceleration vector and i, j = 1, 2 are indexes for two-dimensional analysis.

5.2.5 Porosity Change

Porosity is related to volumetric strain, which can be calculated using a geomechanical model, as follows (Touhidi-Baghini, 1998):

$$\phi = \frac{\left(\varepsilon_v + \phi_0\right)}{\left(1 + \varepsilon_v\right)}, \quad \text{(5-8)}$$

where ϕ_0 and ϕ are the initial and current porosities, respectively, and ε_v is the volumetric strain.

Flow analysis was carried out by building a flow model using a point-distributed grid. The solution can be obtained by applying the initial reservoir pressure, assigning no flow at the symmetry boundary but a prescribed injection flow rate at the wellbore and designating a pressure boundary for the rest of the reservoir boundaries.

Like the approach described in the previous chapter, an element is considered as tensile fractured if the tensile strength (σ_T) of the element has degraded completely. The permeability of an element which undergoes tensile fracturing is calculated using the permeability multiplier.

The width of the tensile fracture is a solution-dependent parameter and is calculated and updated in each time step based on nodal displacements. Fracture energy regularization (described in Chapter 3) is also implemented to reduce the mesh-size impact. The permeability multiplier is applied to change the permeability in the fracture direction, while the permeability in the orthogonal direction remains unchanged or follows the shear permeability criterion if the element has experienced plastic shearing. The orthotropic permeability tensor is then transformed back to the global coordinate system resulting in an anisotropic permeability tensor for the fractured element.

5.3 Iterative coupling scheme

The calculation process to simulate hydraulic fracturing in this work consists of coupling the FLAC2D finite difference program (Itasca Consulting Group Inc., 2011) as the geomechanics module and an in-house 2D finite difference fluid flow module written in MATLAB. The two modules are coupled iteratively based on a procedure described by Tran et al. (2004). The model solves for the pore pressures, deformations, stresses, stress-dependent stiffness, fracture initiation and propagation, porosity and permeability variations, and equivalent fracture permeability in the rock.

In the iterative coupling scheme, the parameters calculated in the geomechanical module (e.g., porosities and permeabilities) and the reservoir variables (e.g., pore pressures) are solved separately in their respective modules, and the solutions are iterated for each time step until convergence is obtained for all the variables. Convergence criteria are satisfied when the maximum error calculated for all the variables, including pore pressures, porosity and principal permeabilities, is simultaneously less than the error margin (2%).

Porosities, permeabilities and pore pressures are the variables that are exchanged between the fluid flow module and the geomechanics module using a coupling scheme written in MATLAB. The fluid flow module sends the calculated pore pressures to the geomechanics module. At this time, FLAC2D updates the pore pressures, calculates the corresponding stresses and deformations and updates the porosities and permeabilities, which are then sent to the fluid flow module. Next, the fluid flow module calculates new pore pressures based on the updated porosities and permeabilities and sends them back to FLAC2D. This process is repeated iteratively for each time step until the convergence criteria are satisfied. It should be noted that convergence on porosity means convergence on the volumetric strain, which in turn requires convergence on the principal strains in the geomechanics module (calculated based on the pore pressures). The iterative coupling scheme of the developed hydraulic fracture model is illustrated in Fig. 5-2.

5.4 Improving numerical stability

The fracture permeability is a third-degree function of the fracture aperture based on the cubic law. A sudden increase of the permeability from the matrix permeability to the fracture permeability may result in numerical instability in the solution process. This problem surfaced in this research and was also documented by Ji (2008). Ji (2008) used a scheme that ramped the fracture permeability at each iteration, which improved the numerical stability and allowed the solution to converge.

The scheme proposed by Ji (2008) is adopted here for calculating both the fracture and matrix permeability. In this scheme, the un-modified permeabilities of a tensile fracture and shear failure are calculated for the current iteration *v*. If the solution does not converge, the permeabilities at iteration *v+1* are modified by using the permeability in iteration *v* (k_i^v) and the un-modified permeability at the current iteration (k_i) according to Eq. (5-9). The calculations are repeated during the iteration process until the maximum errors are less than the specified tolerances (2%) for all of the coupling variables simultaneously.

$$k_i^{v+1} = mod\_fac.k_i + \left(1 - mod\_fac\right).k_i^v \quad \text{(5-9)}$$

where *mod_fac* is the modifying factor, k_i is the principal permeability in direction *i*, and *v* is the previous iteration. A smaller modification factor improves the numerical stability at the cost of increasing the model run time.

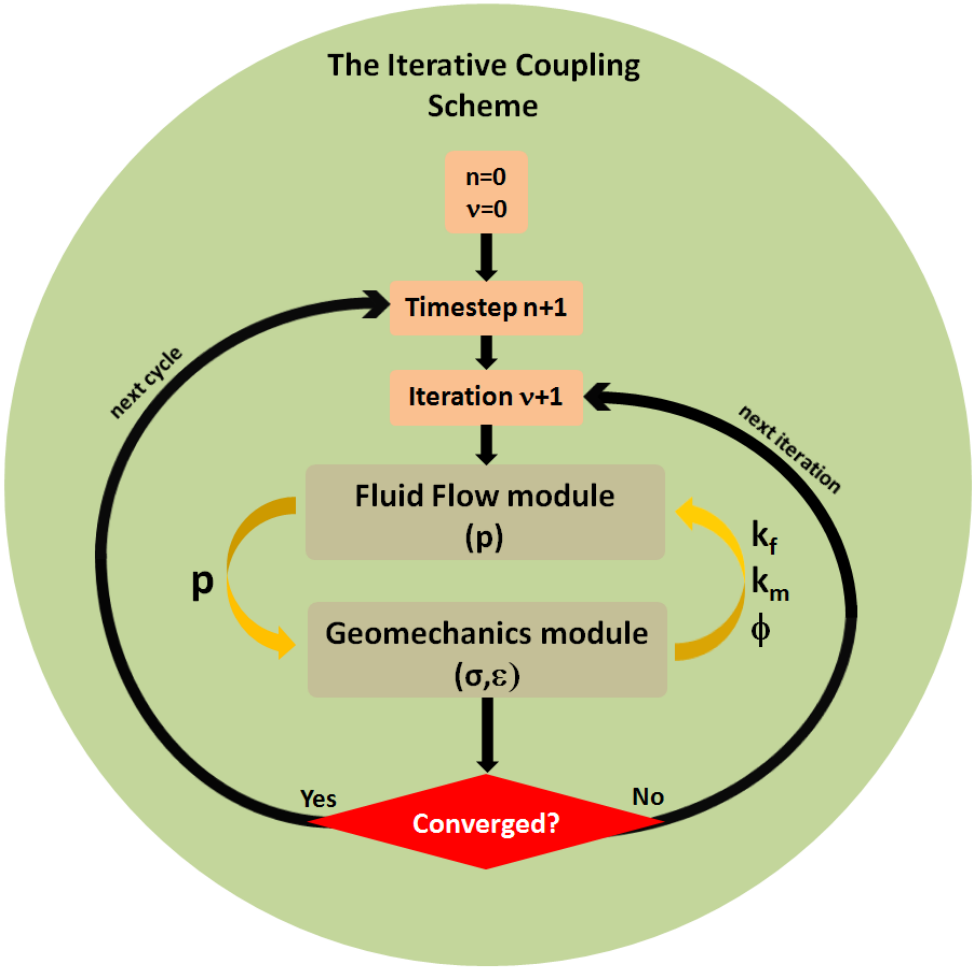

Fig. 5-2:The iterative coupling scheme in the developed hydraulic fracture model. The fluid flow module calculates pore pressures (p). Then the pressures are mapped onto the geomechanics grid. The geomechanics module calculates the stress and strains (σ and ε). Based on the strains (the primary variables), the secondary variables (i.e., the volumetric strains (ε_v) and tensile strains (ε_T)) are calculated. Using these secondary variables, the connecting variables (i.e., porosity (ϕ) as well as the sheared matrix permeability and tensile fracture permeabilities (k_m and k_f)) are calculated and mapped onto the fluid flow grid. In this way, pore pressures, porosity and permeabilities are exchanged between the modules in the iterations.

5.5 Simulation of the Well Tests

The proposed model was used to simulate a series of well tests conducted at the Burnt Lake project (Xu, 2010). The project is located about 300 km northeast of Edmonton (Yeung and Adamson, 1991; Yeung, 1995). Cyclic steam stimulation was first proposed as the oil recovery scheme for this project to produce crude bitumen from the Clearwater formation in the Cold Lake oil sands deposit. Due to low heavy oil prices in the late 1980s, the project was suspended in 1989 and alternative lower-cost recovery methods were studied (Yeung and Adamson, 1991; Yeung, 1995).

The geology of the reservoir and the three well tests carried out in well 01-14-67-03W4 (Xu, 2010) are discussed below.

5.5.1 Reservoir Geology

Yeung (1995) and Xu (2010) provide some information on the geology of the project site, which is summarized here. The target zone of this project was in Clearwater B sand with a thickness of 20 to 30 meters. No gas cap was detected in the logs. In addition, no bottom water was detected except at the extreme northeast corner of the lease property. Clearwater B sand is a fine-grained and unconsolidated sand consisting of 20% quartz, 20% feldspar and 60% rock fragments. Smectite, Illite, Chlorite and Kaolinite comprise about 10 to 20 % of the bulk volume.

The overlying layer is water-bearing Clearwater A sand, which is separated from Clearwater B by 4 to 5 meters of shale. Underlying the reservoir is shaly Clearwater C, which is very fine sand with interlayers of silt. Clearwater B and C are separated with a three-meter shale layer (Yeung, 1995).

The developed model simulates a horizontal plane at the perforated mid-interval and includes only one type of material (the Clearwater sand). The model can capture a potential vertical fracture. Further model details and boundary conditions are described in Section 5.6.

5.5.2 Description of the Well Tests

Three well tests were performed in a cased well in the Burnt Lake project. The well tests were performed in a 178- millimeters diameter wellbore which was perforated in a five-meter interval in the middle of the pay zone (Clearwater B). The tests were conducted at different injection rates. The highest pressure was exercised in Test 3 and the lowest in Test 1. For each test, water was injected into the oil sand formation for a specific period, and the well was then shut in until the bottomhole pressure returned to the static level. The bottomhole pressure was recorded during the test (Xu, 2010). The bottomhole pressures and flow rates for all three well tests are shown in Fig. 5-3.

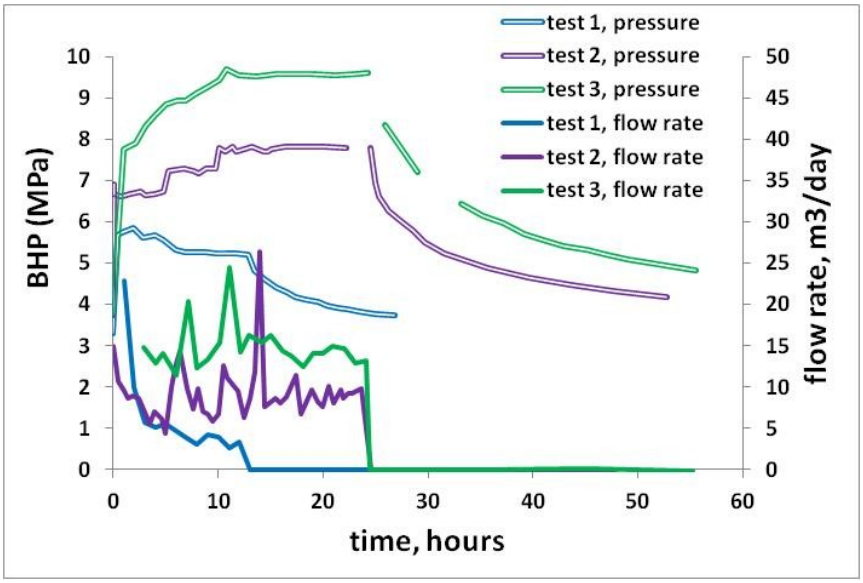

Fig. 5-3: Results of well tests in oil sands in Burnt Lake project (Xu, 2010)

5.6 Description of Numerical Model

To model the well tests, the bottomhole injection rate was used as a boundary condition. The injection flow rate was adjusted in the model in every time step to match the calculated bottomhole pressure with the measurements in the tests. The calculated flow rate was then compared with the measured values to evaluate the model.

5.6.1 Model and Grid Size

As the wellbore is vertical and the pay zone is 25 meters thick extended horizontally, the assumption of plane strain would be reasonable. In this case, it is assumed that stresses and strains are uniform along the vertical axis and the strain component in the vertical direction is negligible. For this reason, a 2D plane strain model is considered in the middle of the pay zone and is stretched horizontally perpendicular to the well. Only half of the reservoir is simulated in the model due to symmetry.

The model consists of a wellbore in a 500-meter by 250-meter half-symmetry geometry as shown in Fig. 5-4. The grid for the plane strain geomechanical model consists of a uniform 1x1-m^2 grid in the area around the injection point with gradually coarser mesh closer to the far field boundaries. The flow model consists of a uniform 1x1-m^2 grid.

5.6.2 Initial and Boundary Conditions

For the geomechanical model, the normal displacements were fixed along the symmetry line. Maximum horizontal stress was applied on the right boundary, and minimum horizontal stress was applied on the top and bottom boundaries of the model as shown in Fig. 5-4. The maximum (σ_v), intermediate (σ_H) and minimum (σ_h) in situ stresses were 10.35, 8.28 and 7.2 MPa, respectively, and the initial reservoir pressure was 3.3 MPa.

For the flow model, the injection rate was applied from the middle of the left boundary (the symmetry axis). The left boundary, except for the injection point, was considered as a no-flow boundary, and all other boundaries were constant pressure boundaries with pressure equal to the initial reservoir pressure.

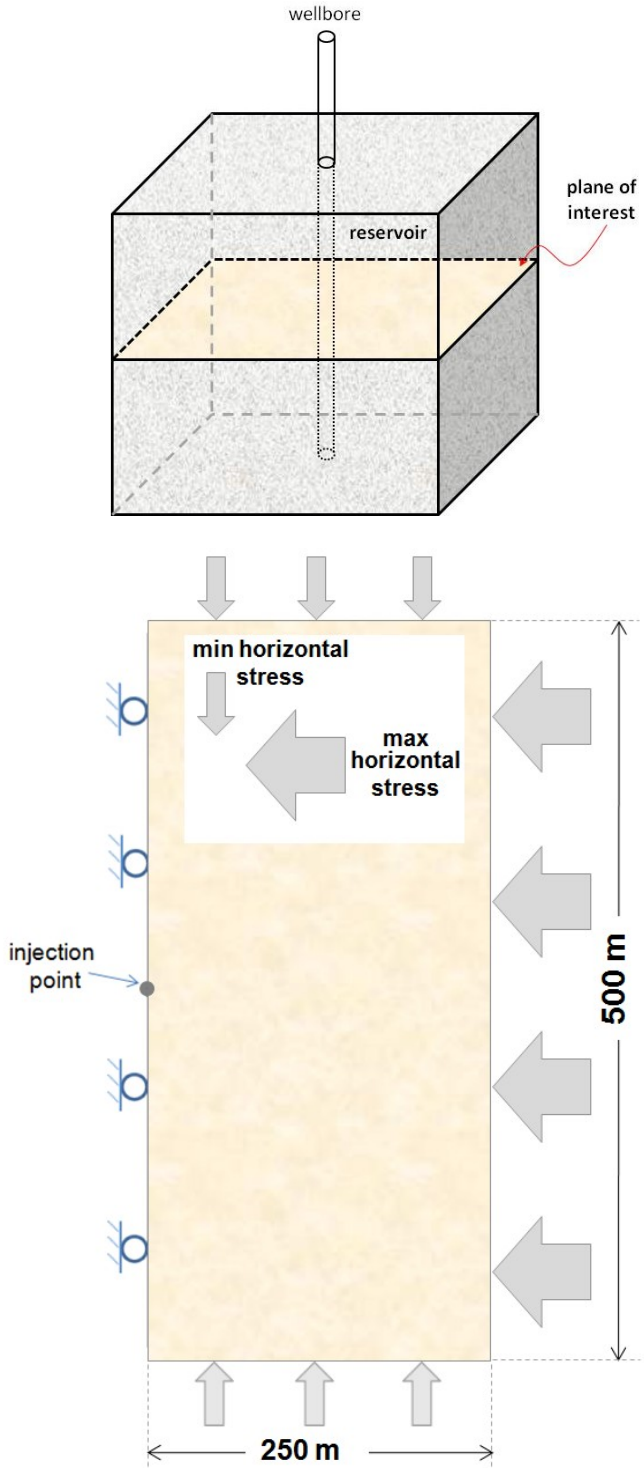

Fig. 5-4: The finite difference model and the boundary conditions of the geomechanical plane-strain model

5.6.3 Reservoir Fluid Properties

Different values have been reported for the bitumen viscosity in this field: 40,000 (Yeung and Adamson, 1991; Yeung, 1995), 300,000 cp (Xu, 2010), and more than 80,000 cp (Kisman and Yeung, 1995) at reservoir conditions. Considering such high viscosities, assuming single-phase water flow (immobile bitumen) would be reasonable for a 24-hour test.

5.6.4 Oil Sands Properties

5.6.4.1 Geomechanical Model and Calibration

A bilinear Mohr-Coulomb model combined with strain hardening/softening was calibrated against a series of triaxial compression tests on Cold Lake oil sands (Wong et al., 1993). The tests were carried out at temperatures ranging from 20 to 300^{o}C and effective confining stresses ranging from 1 to 18 MPa. The procedure proposed by Nouri et al. (2009) and Jafarpour et al. (2012) was followed to calibrate the constitutive model for the numerical simulations. The calibration process can be found in Appendix B. The average grain size (D_{50}) of the Cold Lake oil sands is 0.08 millimeters (Dusseault, 2001), which is used in fracture energy regularization to reduce mesh dependency of the numerical results.

The calibrated parameters were used in a series of simulations by FLAC2D to verify the numerical match of the stress-strain results with the triaxial testing data. Fig. 5-5 shows the variation of the cohesion, friction angle and dilation angle for Cold Lake oil sands versus the equivalent plastic strain at both low and high effective confining stress. The results of these simulations are shown in Fig. 5-6. A typical shear band captured during the simulation at low confining pressure is also shown in this figure.

Plewes (1987) reported the results of Brazilian and unconfined direct tensile tests on cylindrical specimens of rich Athabasca oil sands at a room temperature of 18.5 ^{o}C. The tensile strength of the rich oil sands was reported to be in the range of 8.1-17.1 kPa, based on the Brazilian tests, and 2.1-6.2 kPa, based on direct tensile test. Plewes (1987) related the apparent tensile strength to the high

viscosity of the bitumen at a low temperature and/or negative pore pressure developed during the testing. This tensile strength may be higher at the in situ initial temperature of 12 ^{o}C. A tensile strength of 100 kPa was assumed in the simulations. Also a sensitivity analysis was conducted with respect to this parameter to study its impact on the fracturing behavior of the reservoir.

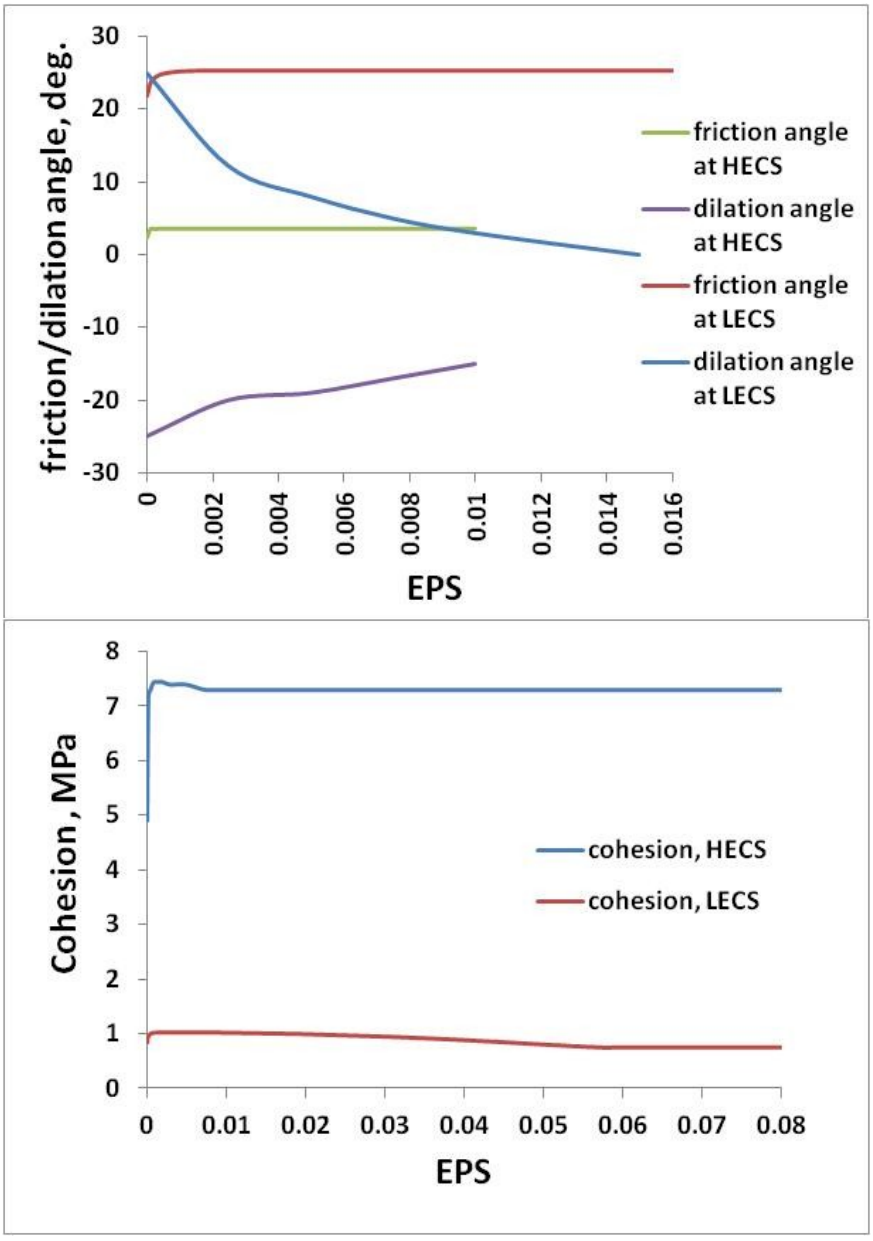

Fig. 5-5: Cohesion, friction and dilation angles of Cold Lake oil sand samples as a function of the equivalent plastic strain at low and high effective confining stresses

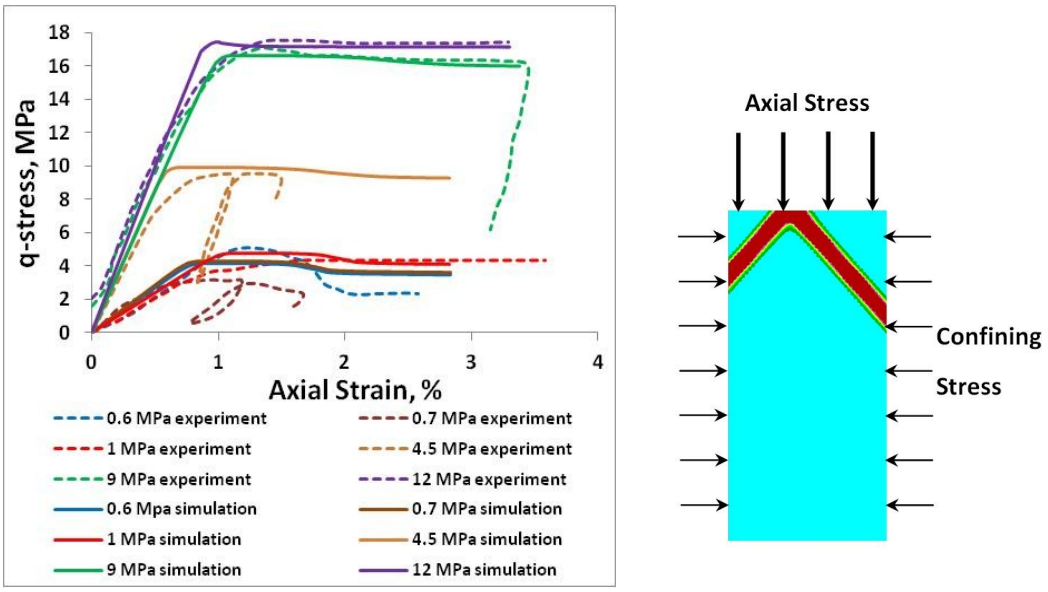

Fig. 5-6: Simulation results for the triaxial compression tests performed by Wong et al. (1993). Left: The stress-strain plots for the entire test. Right: A typical shear band captured during the lowest effective stress test. The unloading and loading cycles are neglected.

5.6.4.2 Permeability of Oil Sands

The reservoir had a porosity and initial oil saturation of 33% and 70%, respectively, with absolute permeabilities of 0.5 to 2.5 Darcies (Xu, 2010).

Touhidi-Baghini (1998) developed his shear permeability model based on McMurray oil sands as well as reconstituted specimens. It was expected that the B values proposed by Touhidi-Baghini would be reasonably valid to describe the behavior of Cold Lake oil sands during shearing. Touhidi-Baghini's model with the proposed B values was used to simulate shear-induced permeability in the hydraulic fracture model developed here. A sensitivity analysis was later conducted with respect to the B parameter to investigate its impact on the numerical results.

The effective permeability of the reservoir to water was calculated using the standard Horner plot (Hannan and Nzekwu, 1992), which describes a linear relationship between reservoir transmissibility (kh/μ) and Horner time, $(t_{inj} + \Delta t)/\Delta t$.

From the semi-log straight line, the slope of the line was calculated and used to calculate transmissibility using the following equation:

$$\frac{Kh}{\mu} = \frac{cQB}{m}, \quad \text{(5-10)}$$

where kh/μ is formation transmissibility, K is effective permeability, h is effective reservoir thickness, μ is reservoir viscosity, Q is the fluid injection rate, B is the formation volume factor, m is the Horner semi-log straight line slope and c is a constant.

The semi-log Horner plots for the three well tests are plotted in Fig. 5-7. The Horner semi-log straight line slopes for the well tests were 1300, 2900 and 4300 kPa/cycle. Assuming a 25-meter reservoir height and average flow rates of 4, 9.9 and 15 m^3/day, effective permeabilities of 0.264, 0.293 and 0.30 md were calculated, respectively, for well tests 1, 2 and 3.

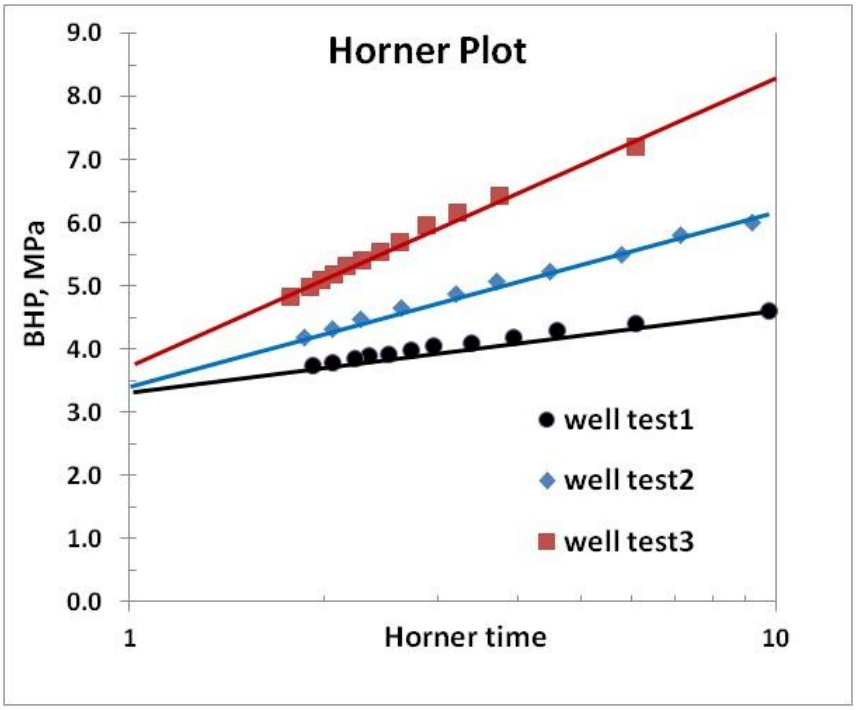

Fig. 5-7: Horner plot of the three well tests

5.6.4.3 Summary of Oil Sands Properties

The material properties used in the base-case simulation are summarized in Table 5-1. These properties represent the best estimates based on the limited data in hand. For those parameters that were not available, the values were selected from analogue data supplemented by sensitivity studies as will be described in the next sections.

Table 5-1: Summary of the input material properties used in the base case numerical model

Parameter	Value	Parameter	Value
Maximum principal stress (MPa)[+]	10.35	Tensile strength[---] (MPa)	0.1
Intermediate principal stress (MPa)[+]	8.28	Initial cohesion at LECS[*] (MPa)	0.85
Minimum principal stress (MPa)[+]	7.2	Initial cohesion at HECS[*] (MPa)	4.9
Reservoir pressure (MPa)[+]	3.4	Initial friction angle at LECS[**] (deg.)	21.28
Initial water saturation (%)[+]	30	Initial friction angle at HECS[***] (deg.)	3.45
Elastic modulus (MPa)[+++]	Variable	Initial dilation angle at LECS[**] (deg.)	25
Poisson ratio (Wong et al., 1993)	Variable	Initial dilation angle at HECS[***] (deg.)	-24.5
Absolute permeability[-]	300 md	Porosity (%) (Yeung and Adamson, 1991)	34
B_h and B_H parameters[--]	2 and 5		

+ Xu (2010), ++ Assessed from laboratory experiments on Cold Lake oil sands performed by Wong et al. (1993), - Found by sensitivity analysis and history matching, -- From calibrations against experimental data for McMurray oil sands by Touhidi-Baghini (1998), --- Assumed, * See Fig. 5-5 for variations; calculated from laboratory experiments on Cold Lake oil sands performed by Wong et al. (1993), ** At Low Effective Confining Stress (LECS); calculated from triaxial data for Cold Lake oil sands (Clearwater formation) performed by Wong et al. (1993) (see Fig. 5-5 for variations), *** At High Effective Confining Stress (HECS); calculated from triaxial data for Cold Lake oil sands (Clearwater formation) performed by Wong et al. (1993) (see Fig. 5-5 for variations)

5.6.5 Single-Phase versus Two-Phase Flow Calculations

It is assumed that bitumen is immobile during the well tests due to its high viscosity at low reservoir temperature (12°C) during water injection. With little bitumen flow during the injection, it is reasonable to assume a constant bitumen volume in the pores of the rock. Therefore, any expansion in the pore volume (volumetric expansion of the rock) is assumed to be filled only with water, as schematically shown in Fig. 5-8. This assumption makes it possible to calculate the water saturation and assessment of relative permeability during the injection without having to perform a two-phase flow analysis.

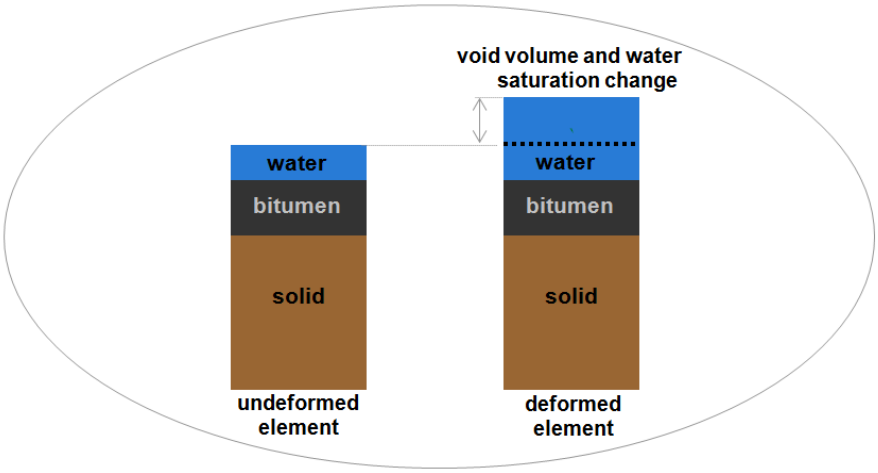

Fig. 5-8: Schematic of void and water volume saturation due to volumetric straining

Based on this assumption, the new saturation of water is calculated as follows:

$$s_w + s_b = 1 \quad \text{(5-11)}$$

$$V_w + V_b = V_v \quad \text{(5-12)}$$

where s_w and s_b are the water and bitumen saturations, respectively, and V_w, V_b and V_v are the volumes of water, bitumen and the void space, respectively.

Assuming constant bitumen volume in the voids:

$$dV_w = dV_v \quad \text{(5-13)}$$

Based on the definition of porosity, ϕ ,

$$V_v = \phi V_t \quad \text{(5-14)}$$

$$dV_v = \Delta V_v = \phi \Delta V_t + V_{to} \Delta\phi = \phi\left(\Delta\varepsilon_v V_{to}\right) + V_{to}\Delta\phi = V_{to}\left(\phi\Delta\varepsilon_v + \Delta\phi\right) \quad \text{(5-15)}$$

where V_t represents the total volume of the element under consideration and subscript "o" refers to the initial value of the variables.

$$s_w = \frac{V_w}{V_v} = \frac{V_{wo} + dV_w}{V_{vo} + dV_v} = \frac{V_{wo} + dV_v}{V_{vo} + dV_v} \quad \text{(5-16)}$$

After some manipulations, Eq. (5-16) becomes:

$$s_w = \frac{s_{wo}\phi_o V_{to} + V_{to}\left(\phi_o\Delta\varepsilon_v + \Delta\phi\right)}{\phi_o V_{to} + V_{to}\left(\phi_o\Delta\varepsilon_v + \Delta\phi\right)} \quad \text{(5-17)}$$

$$s_w = \frac{s_{wo}\phi_o + \phi_o\Delta\varepsilon_v + \Delta\phi}{\phi_o + \phi_o\Delta\varepsilon_v + \Delta\phi} \quad \text{(5-18)}$$

Eq. (5-18) relates the new water saturation to the variation of porosity and volumetric strain. Once the new water saturation is calculated, the new relative permeability to water is obtained from the relative permeability graph.

Equation (5-18) relates the water saturation to oil sand's porosity and volumetric strain variations. Once the current water saturation is calculated, the current relative permeability to water is obtained from the relative permeability relationship. The relative permeability data proposed for the mid-layer of Burnt Lake oil sands (Kisman and Yeung, 1995) was used in the simulations.

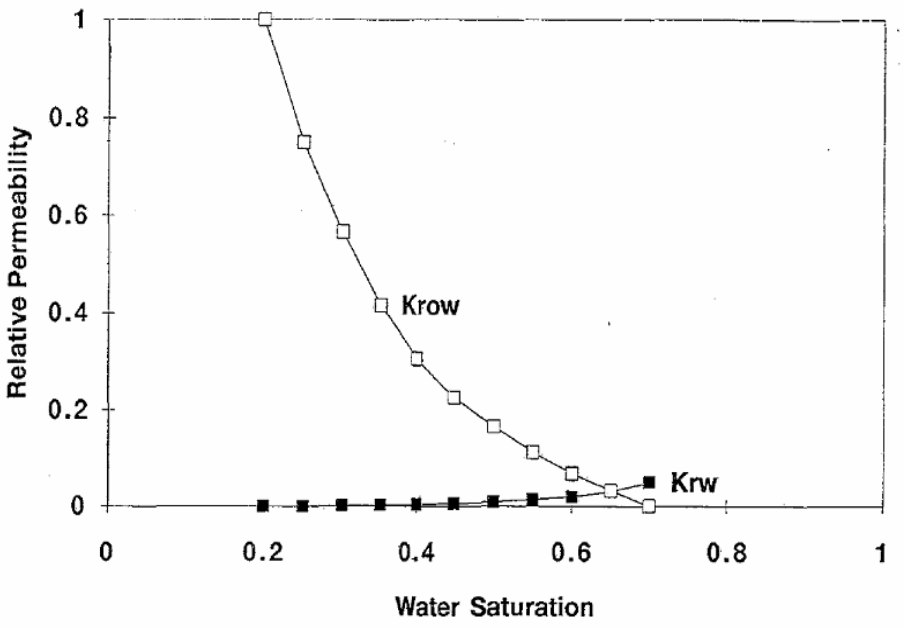

Fig. 5-9: Relative permeability curve used in the model (Kisman and Yeung, 1995)

5.7 Numerical Model Results

In this section, the simulation results are compared with the measurements from the well tests. It was previously mentioned that a wide range of 500 to 2500 md was reported for the absolute permeability of the reservoir (Xu, 2010). To find a unique value, absolute permeability was varied in different runs to match the numerical results with the field measurements while keeping the same mesh size in all the simulations. Mesh sensitivity of the numerical results was also evaluated. The results are discussed in the following sections. Later, a hydraulic fracture simulation was conducted using larger flow rates than those applied during the well tests to assess the initiation and propagation of a tensile fracture in the oil sands.

5.7.1 The Base Numerical Model

5.7.1.1 Absolute Permeability

Assuming an initial water saturation of 28.8%, the well tests were simulated using the absolute permeabilities of 500 and 2,500 md as reported for the field experiments (Xu, 2010). However, no information was reported about how these

permeability measurements were obtained. As the simulations yielded different results than the measurements, a sensitivity analysis was conducted with respect to the absolute permeability value. Four absolute permeabilities of 200, 300, 500 and 1000 md were used in simulations. It was found that an absolute permeability of 300 md resulted in the best match with the field measurements for the base mesh (Fig. 5-10). This absolute permeability is, however, lower than the reported range (500 to 2,500 md). There are two possible explanations for this: first, the existence of interbedded shale layers and carbonate-cemented beds with up to 0.5 m thickness (Yeung, 1995; Xu, 2010), and also a Chlorite/Berthierine clay rim around the sand grains (Yeung, 1995) at some depth in Clearwater B could reduce the absolute permeability of the reservoir. The absolute permeability of 300 md was chosen for the base case analysis and was used for the rest of the research.

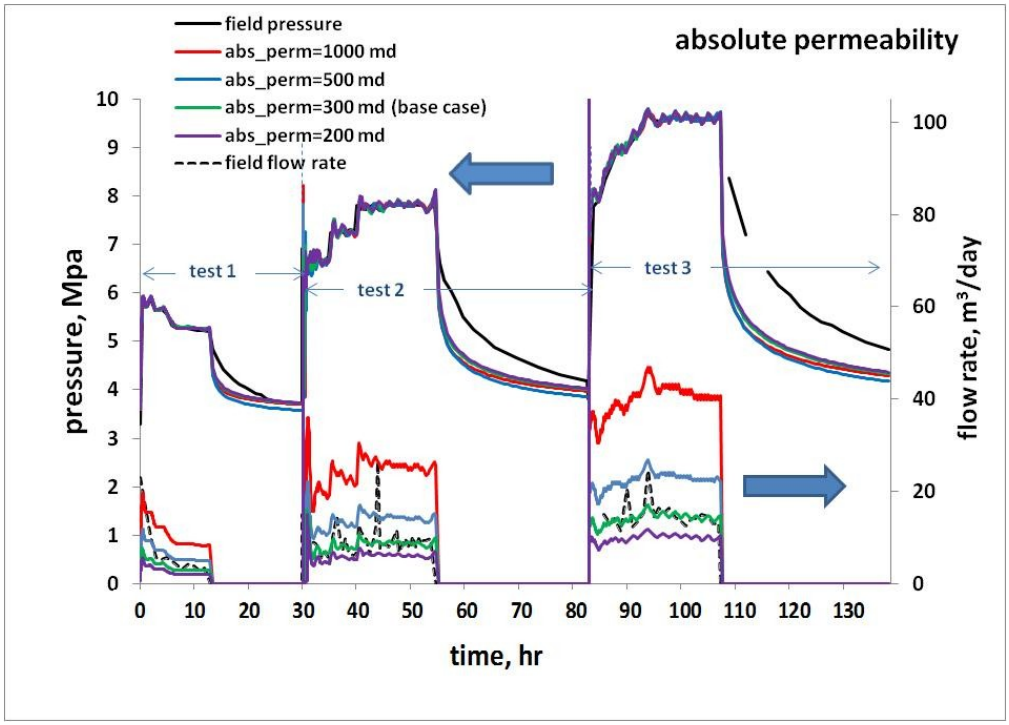

Fig. 5-10: Impact of absolute permeability on numerical results

5.7.1.2 Examining Mesh Size Effect

To evaluate the influence of mesh size, three mesh sizes were examined in this research. The fracture energy regularization method was also used to reduce the mesh-size dependency that originates from strain softening.

The results of the mesh dependency analysis are plotted in Fig. 5-11. The figure shows that despite the application of fracture energy regularization, some degree of mesh dependency affected the simulations even in the simulation results of Well Test 1, which had the lowest injection pressure. As shown, the results became more mesh-dependent for Well Test 3 compared to Test 1, which could be a function of the larger shearing plastic deformations occurring during Well Test 3, as will be shown later. Another contributing factor in the observed mesh dependency could be the dependence of porosity, saturation and permeability on deformations. A small mesh dependency in the calculated strains can magnify the variations of porosity, saturation and permeability. It can also eventually magnify the variations of the strains again.

A mesh size of 1 meter x 1 meter was selected for the base case analysis.

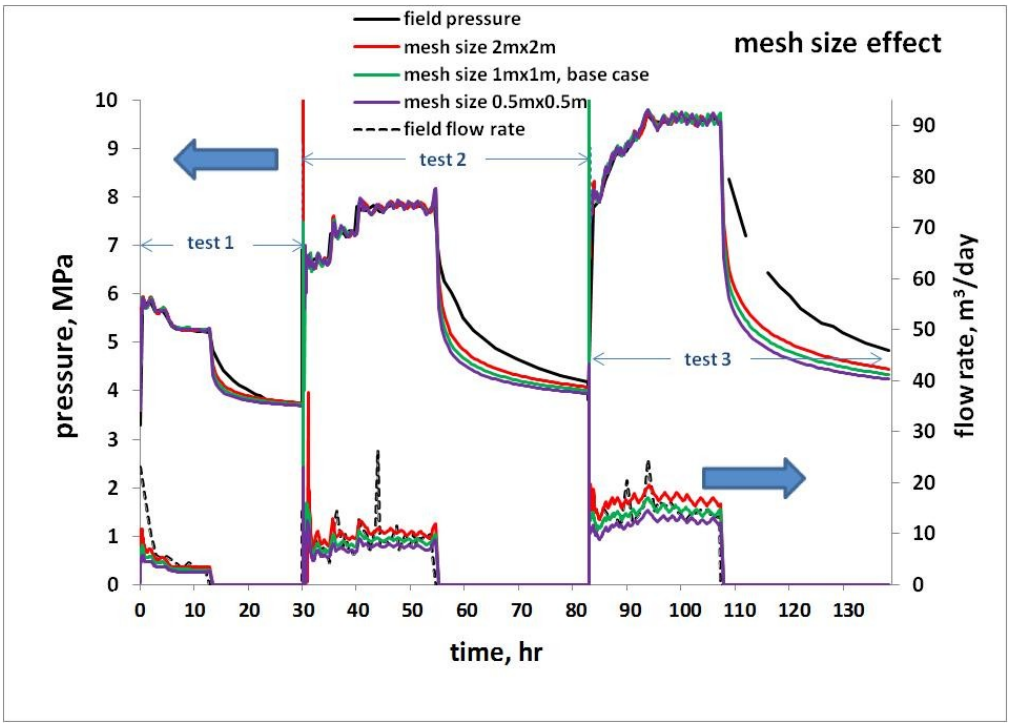

Fig. 5-11: Mesh size effect

Fig. 5-11 shows that there is a stronger mesh dependency at higher pressures. The fracture energy regularization has been proven to highly reduce or even eliminate mesh dependency when the stress-strain analysis is performed (Pietruszczak and Mróz, 1981; Bažant and Oh, 1983; Klerck, 2000; Crook et al.,

2003; Nouri et al., 2009; Jafarpour et al., 2012). Chapters 3 and 4 provided evidence that the fracture energy regularization method can reduce but not eliminate mesh dependency in a coupled deformation-fluid flow analysis, where fluid flow parameters are tied to the numerical stress/strain calculations in each time step. Mesh dependency has also been observed in the flow simulation of a fractured reservoir using the smeared approach (Weill and Latil, 1992).

The simulation results of the base case model (with 300 md permeability) are shown in Fig. 5-12. As shown later in this section, the numerical results do not indicate any tensile hydraulic fractures during the three well tests. Xu (2010) reported similar findings in his 3D numerical simulations of the same well tests using a strain-induced anisotropic shear permeability model (Wong, 2003). Xu (2010) showed that all the deformations during the well tests were either elastic (in Test 1) or shear dilative (in Tests 2 and 3). Similarly in this research, it was found that a hydraulically induced dilated zone formed in the oil sands in Well Tests 2 and 3.

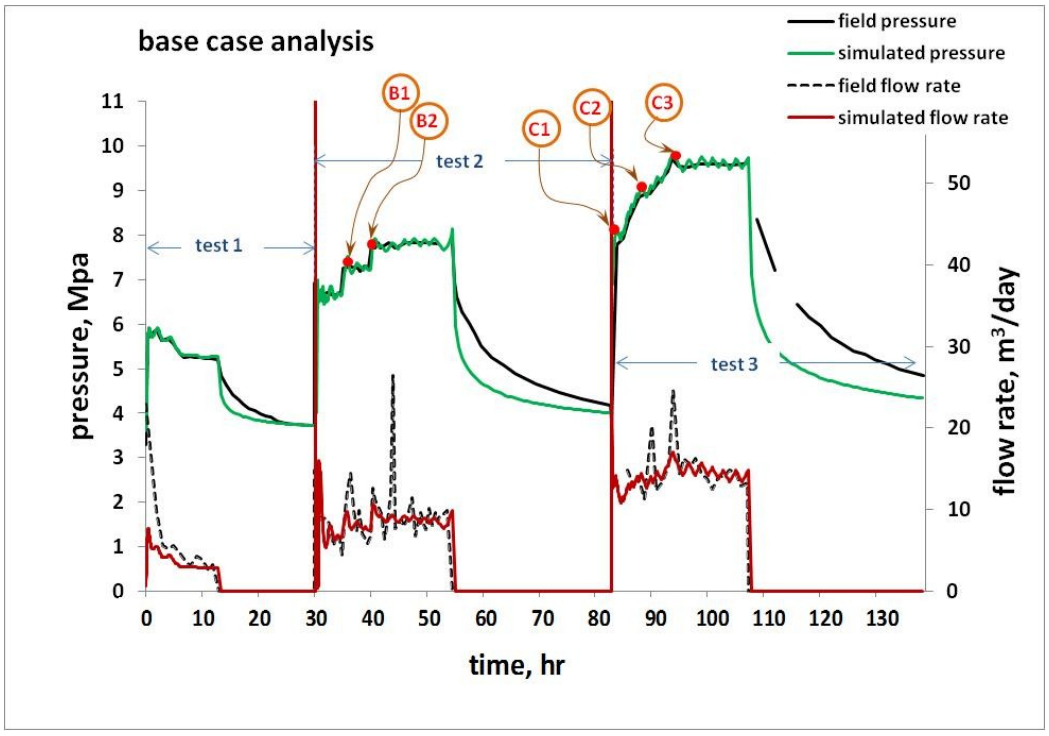

Fig. 5-12: Simulation results of the base-case model

Fig. 5-13 illustrates the stress path of an element near the injection point in Well Test 3 from the simulation results of Xu (2010). Based on the stress path, Xu (2010) detected oil sand shearing but did not observe tensile fracturing in Test 3.

Fig. 5-14 shows the stress path of the wellbore element for the base case model. The stress path in Well Test 1 does not intersect the shear failure envelope. It indicates that due to low injection pressures in Well Test 1, the reservoir response is predominantly elastic, similar to the results obtained by Xu (2010). After the shut-in, effective stresses bounce back and the stress path returns to the original stress state.

Fig. 5-14 shows the stress path of the wellbore element for the base case model. The stress path in Well Test 1 does not intersect the shear failure envelope. It indicates that due to low injection pressures in Well Test 1, the reservoir response is predominantly elastic, similar to the results obtained by Xu (2010). After the shut-in, effective stresses bounce back and the stress path returns to the original stress state.

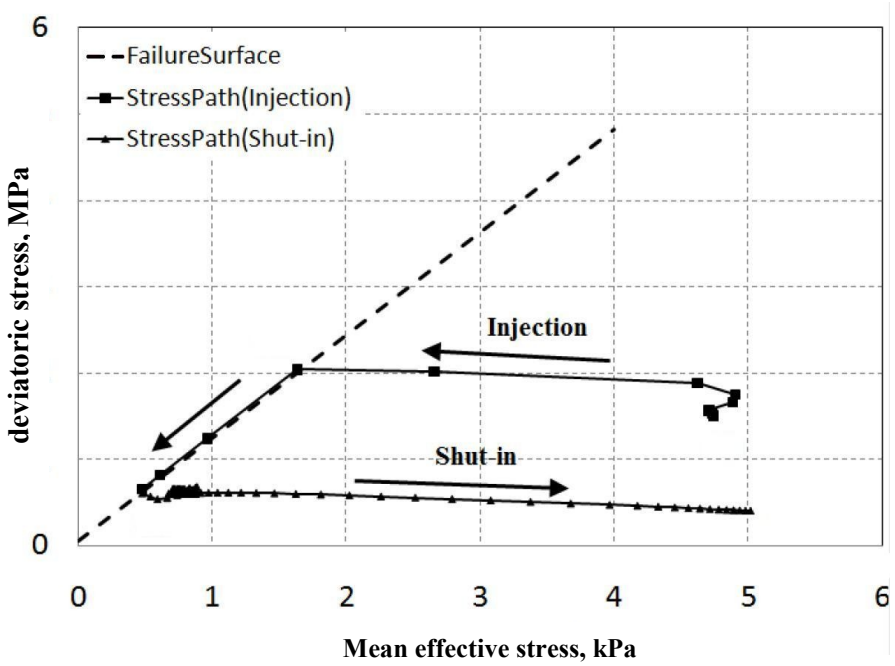

Fig. 5-13: Stress path of Well Test 3 in the 3D numerical analysis conducted by Xu (2010) using the strain-induced anisotropic shear permeability model (Wong, 2003)

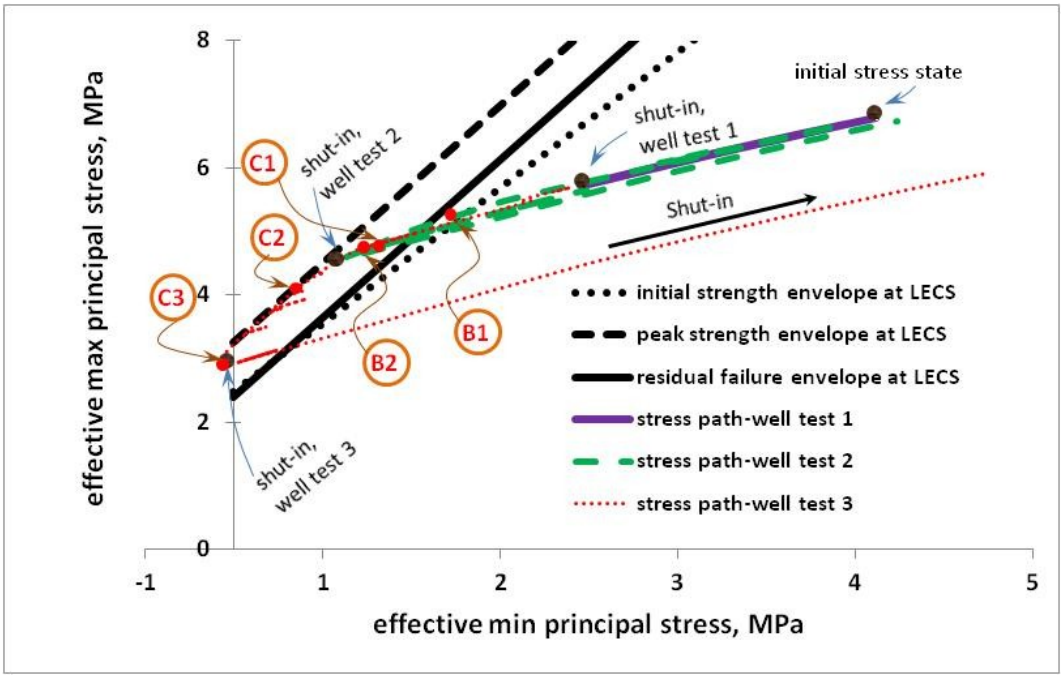

Fig. 5-14: Stress path at the wellbore in the simulated well tests

As confirmed by the stress path, the drop in the bottomhole pressure (BHP) at the early stages of Well Test 1 (Fig. 5-12) is caused by the reduced injection rate, not by the development of a hydraulic fracture (either shear or tensile). In late stages of injection in Test 1 (Fig. 5-12), the flow rate is nearly constant, resulting in a constant bottomhole pressure.

As per Fig. 5-12, a continued increase in the bottomhole pressure in Well Test 2 causes the stress path to intersect with the initial yield envelope at Point B1 at an injection pressure of 7.5 MPa and further advancement of the stress path beyond the initial yield envelope to Point B2 at a pressure of 7.9 MPa. However, the stress path does not reach the peak-strength envelope (see Fig. 5-14). The material is still in the strain-hardening stage during Test 2. After shut-in, the stresses bounce back elastically in a path close to the injection path. No tensile fracturing is detected numerically during this test. This is consistent with the numerical results reported by Xu (2010).

In Well Pest 3, pressure quickly reaches point C1 (8.1 MPa pressure). The stress path approaches the peak strength at the pressure of 9.0 MPa, shown by Point C2 in Fig. 5-14. The stress path then moves on to the peak shear envelope

towards Point C3 (9.75 MPa pressure), the highest pressure experienced in this set of well tests. Maintaining the pressure at 9.75 MPa does not result in a tensile fracture, nor further shearing. The oil sand does not show strain softening in Well Test 3 as the stress path stays at the peak strength until the injection is shut in. After the shut-in, the material experiences stress rebound in a path nearly parallel to the path during the injection. The paths do not match due to the plastic deformation. Simulations indicate no tensile fracturing in Test 3 despite the development of a shear yield zone. Xu (2010) reported similar numerical results, as shown in Fig. 5-13.

The simulation results indicate no tensile fracture in any of the three well tests, despite the bottomhole pressure of 9.75 MPa in Well Test 3, which is larger than the two initial horizontal stresses (7.2 MPa and 8.28 MPa) but lower than the vertical stress (10.35 MPa).

5.7.2 Fracture Initiation and Propagation Pressure

The simulations so far indicated that no tensile hydraulic fractures developed during the well tests. To investigate the initiation and propagation of a tensile fracture in the reservoir, a hydraulic fracture simulation was carried out using a higher flow rate of 40 m^3/day for a duration of 13 hours. The results in the form of bottomhole pressure and fracture length are plotted in Fig. 5-15. The figure shows several cycles of fracture closure and reopening during the injection period. The figure also indicates a breakdown pressure of 10.1 MPa, which is close to the maximum in situ stress (i.e., the vertical stress). The propagation pressure is approximately equal to 8.8 MPa, resulting in a 16-meter fracture for a 13-hour injection period.

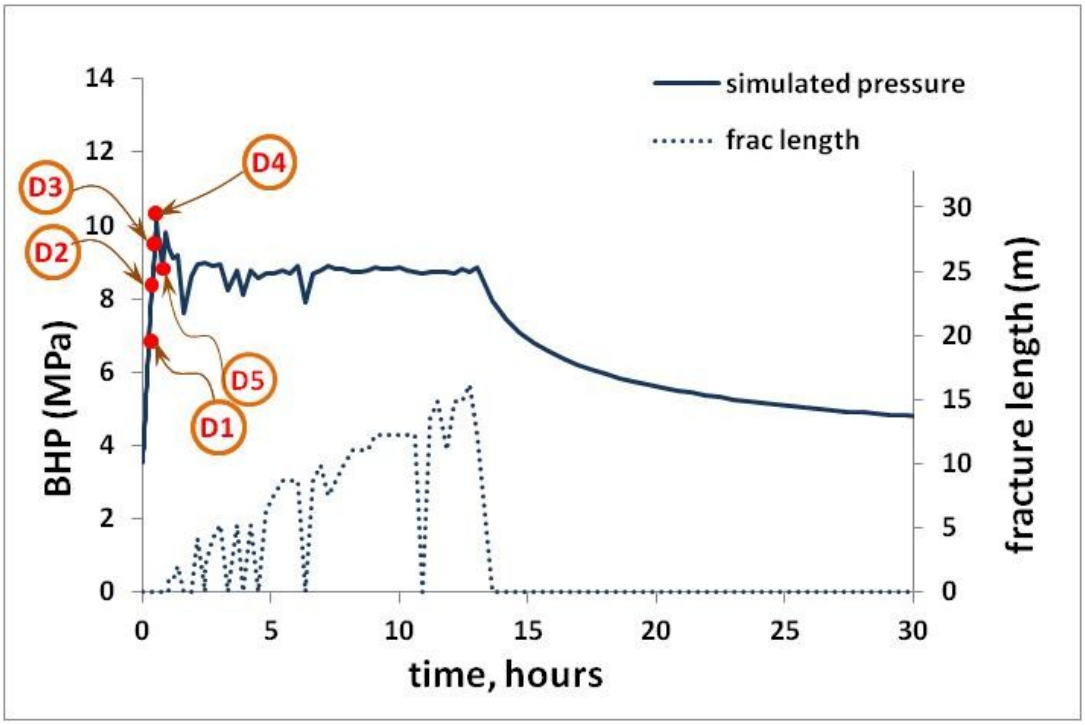

Fig. 5-15: The fracturing response of the oil sands upon cold water injection

The stress path of the hydraulic fracture simulation in Fig. 5-16 indicates that shear yielding starts at Point D1 which corresponds to the pressure of 6.76 MPa. Point D2 in Fig. 5-16 corresponds to the peak shear strength envelope which occurs at a pressure of 8.4 MPa. The compressive stress then drops as the injection pressure continues to rise until the effective stress reaches the tensile strength of the material at Point D3 at 9.4 MPa pressure. A further increase of the bottomhole pressure up to 10.1 MPa (points D3 to D4) degrades the tensile strength of the sand until the tensile strength of the material drops to zero at Point D4 (at 10.1 MPa BHP) when tensile fracturing occurs. The opening of the fracture results in a temporary reduction in pore pressure down to 8.8 MPa at Point D5. At Point D5, the oil sands have totally lost their cohesive and tensile strength due to fracturing. Continuing injection leads to higher pore pressures, reopening the fracture and causing it to propagate. The stress path in Fig. 5-16 shows that cyclic pressure drops and rises during the injection period. It should be noted that part of these cycles, especially during fracture initiation, can be attributed to mesh size, and may be a numerical artifact.

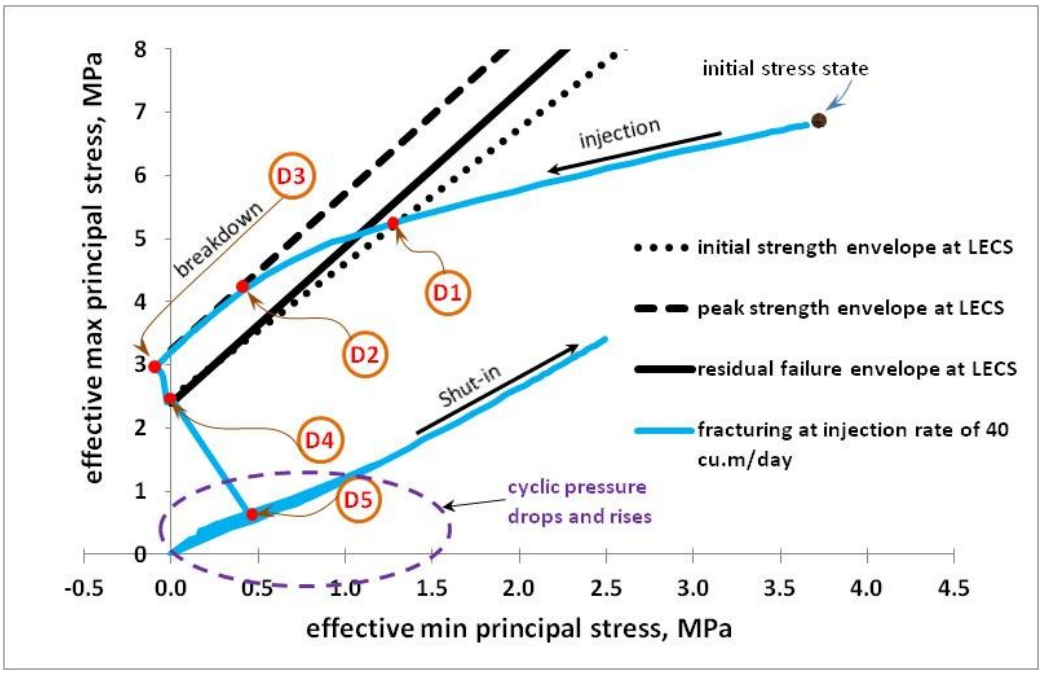

Fig. 5-16: Stress path at the wellbore in the simulated hydraulic fracturing

Fig. 5-17 compares the shear zones of the base case model for the well tests as well as the model with an artificially higher flow rate (to induce a tensile hydraulic fracture). The shear zone in the high-rate model is much larger than that in the simulated well test, which can be attributed to the higher pore pressures, lower effective stresses and, thus, the lower shear strength. The width of the sheared zone perpendicular to the fracture propagation direction is almost unchanged along the fracture and is approximately equal to 10 meters. It is important to note that the shear zone moves 11 meters ahead of the tensile fracture when the tensile fracture is 16 meters.

Some field observations (in terms of fracture pattern) agree with the results obtained in this research. Microseismic monitoring during fracturing pressure of 79 to 83 MPa in Bossier tight sandstone indicated a half-fracture length of 350-450 feet (Settari et al., (2002a). Settari et al. believed that the fracture should be shorter than what the microseismic events indicated and also that the microseismic data were related to both the fracture length and the size of the leak-off zone. The microseismic events around the fracture could extend 50 feet ahead of the fracture tip (the fracture length was predicted using standard methods)

(Settari et al., 2002b) and also 50 meters sideways (Settari et al., 2002a; Settari et al., 2002b). At early injection time, the microseismic events were focused on the close perimeter of the fracture while later they were found everywhere from the wellbore to the fracture tip (Settari et al., 2002b). Shearing creates a zone of shear failure/fracture in the proximity of the main tensile fracture. This type of observation has also been reported in laboratory experiments (McElfresh et al., 2002).

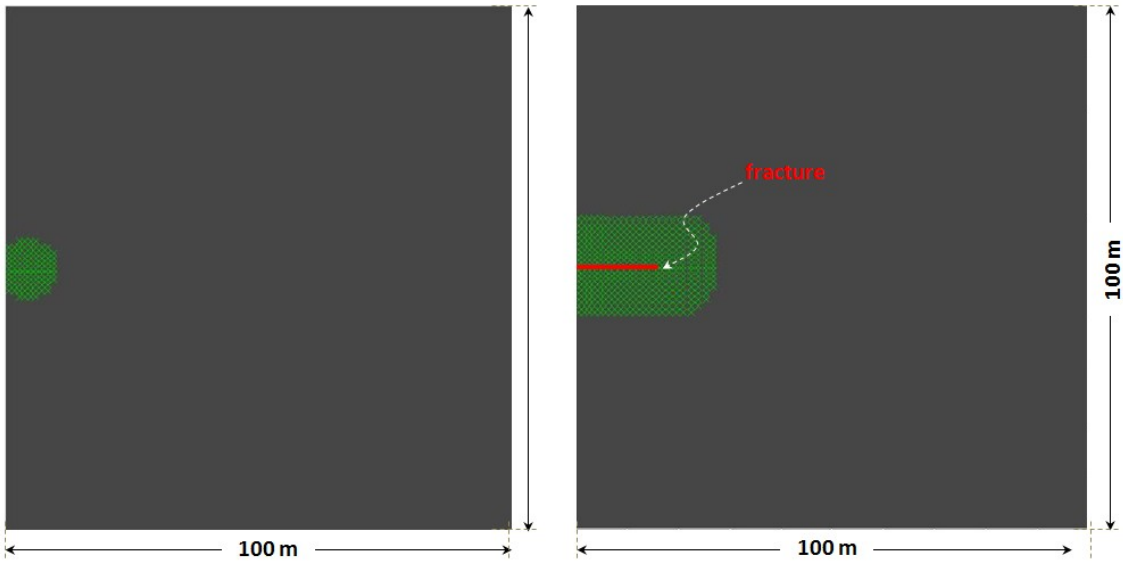

Fig. 5-17: Sheared yield zone due to injection. Left: The simulated well tests. Right: The induced hydraulic fractured model

5.7.3 Sensitivity Analysis

A series of analyses was conducted to evaluate how sensitive the tensile fracture results were to the model mesh size. In addition, further sensitivity analyses were performed with respect to the flow and geomechanical parameters including apparent tensile strength and cohesion of the oil sands, magnitude of the minimum and maximum principal stress, absolute permeability and elastic modulus of the oil sands, ramp-up time and shear permeability evolution rate (B parameter). The analyses were conducted to clarify the influence of the aforementioned parameters on the fracturing response. The results are discussed in the following sections.

5.7.3.1 Mesh size effect

Three different mesh sizes—2m x 2m, 1m x 1m, and 0.5m x 0.5 m—were examined to assess the mesh sensitivity of the results. Fig. 5-18 shows the results of the three mesh sizes. The larger element size (2m x 2m) resulted in a larger fracturing pressure and a significantly shorter fracture. It also shows a more unstable growth of the fracture length. Results appeared to converge as the element size was refined to 1m x 1m and 0.5m x 0.5m. The smaller mesh size shows a smoother fracture growth at the early stage of injection. As the smaller mesh is extremely expensive in terms of solution time (nearly 120 hours on a 2.7 GHz CPU Intel i7 PC, 9GB RAM), a 1m x 1m mesh was selected for the base case model for the rest of the analyses.

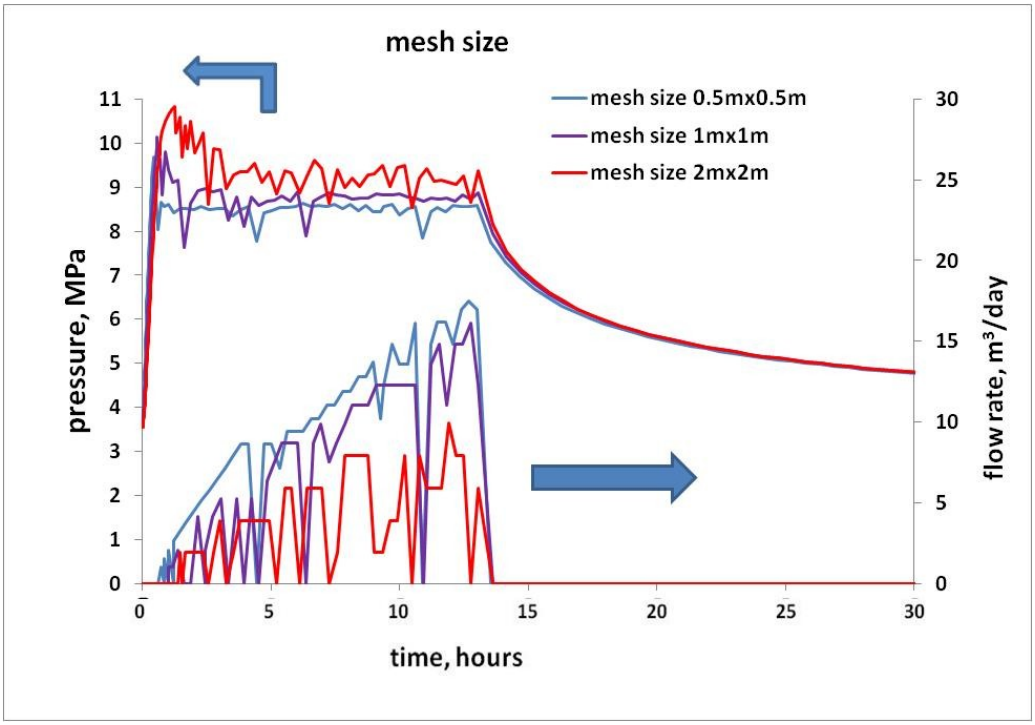

Fig. 5-18: The mesh size impact on fracture pressure and length

5.7.3.2 Apparent tensile strength

Since different values for tensile strength of oil sands have been reported in the literature, a sensitivity analysis was performed against this parameter to evaluate the impact of tensile strength on the reservoir fracturing response. In

addition to the base case (tensile strength of 100 kPa), two different tensile strengths of 0.5 kPa and 1.0 MPa were examined in the simulations.

Fig. 5-19 illustrates the impact of tensile strength on the fracturing response of the reservoir, indicating a shorter fracture and slightly larger fracture propagation pressure for higher tensile strength. The difference in the fracture length with 0.1 and 1.0 MPa tensile strength was almost 5 meters after 13 hours of injection. The difference in the injection pressure, however, was small (almost 0.4 MPa) for the two cases. The lower pressure corresponded to the smaller tensile strength. While the breakdown pressures for the cases with tensile strength of 0.1 MPa and 0.5 MPa showed little difference, the difference for the cases with tensile strength of 0.5 MPa and 1.0 MPa was more noticeable at a difference of 8.75 vs. 9.15 MPa, respectively. In addition, fewer fracture-length fluctuations were observed in the low tensile-strength case, while the fracture length of the larger-tensile-strength case included more closure and opening cycles. This is because the pressure drop in the larger tensile-strength case was more significant than that in the other cases.

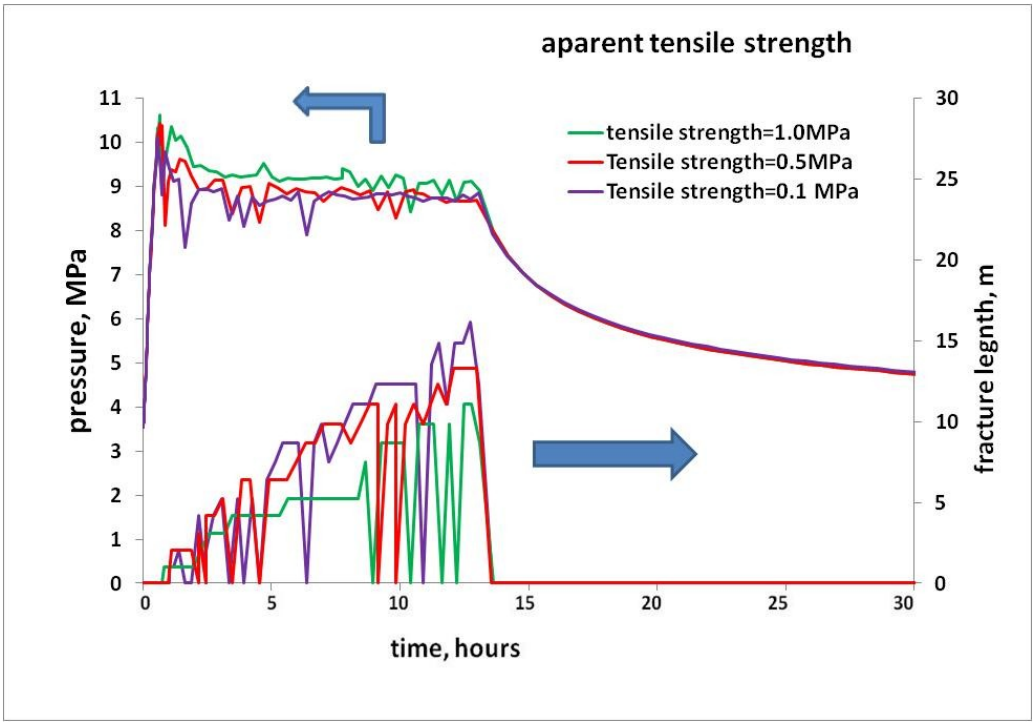

Fig. 5-19: Sensitivity analysis with respect to the tensile strength of oil sands

5.7.3.3 The minimum principal stress

A sensitivity study was also conducted with respect to the magnitude of the minimum principal stress. This parameter is believed to directly control the breakdown and propagation pressure. Two stress magnitudes of 6.7 and 7.7 MPa were studied and compared to the base case results. The results are plotted in Fig. 5-20.

The figure shows that the magnitude of the minimum principal stress has a large impact on fracturing pressure. Breakdown pressures of 9.35, 10.1 and 11 MPa were found for the minimum stress magnitudes of 6.7, 7.2 and 7.7, respectively. For the minimum stress increases in 0.5 MPa increments, the breakdown pressure differences were 0.75 and 0.9 MPa (compared to the base case). Propagation pressures of the three different cases were 9.6, 8.8 and 8.0 MPa, from the larger to smaller minimum stresses, respectively (0.8 MPa increment in propagation pressure for 0.5 MPa increment in the minimum stress). Smaller minimum stress results in a longer fracture.

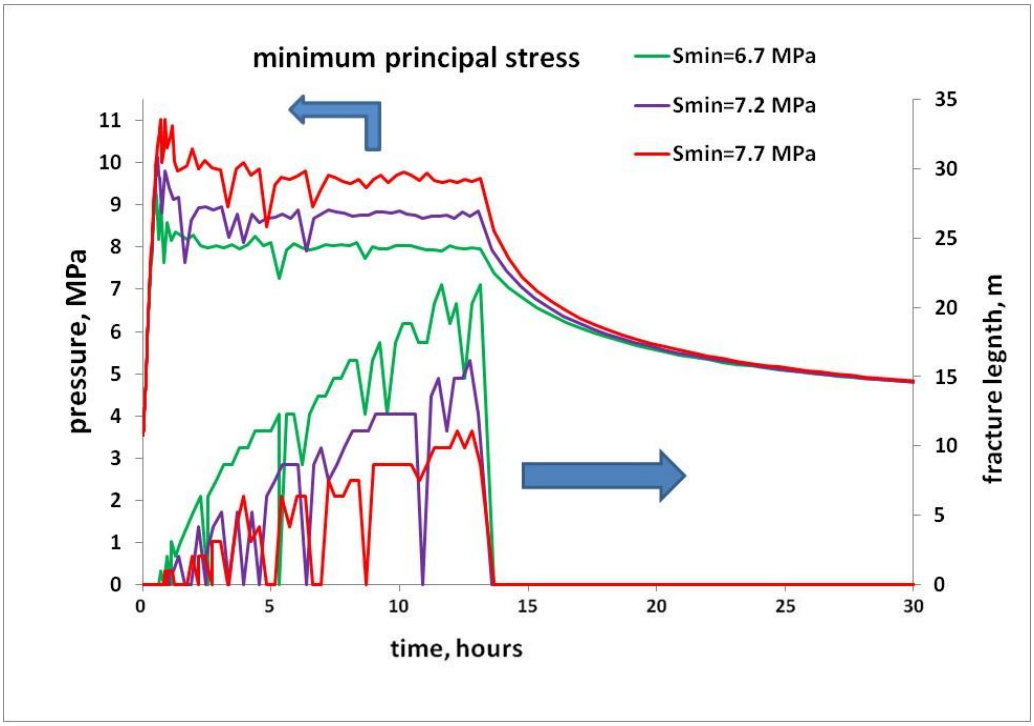

Fig. 5-20: The impact of the minimum principal stress magnitude

5.7.3.4 The maximum principal stress

The influence of the magnitude of the maximum principal stress on the initiation and propagation pressure was also studied. Three different magnitudes of 9.85, 10.35 (the base case) and 10.85 MPa were selected to examine the impact of the maximum principal stress.

As plotted in Fig. 5-21, the three cases show close breakdown pressures within a 0.25 MPa difference. The case with larger maximum principal stress showed a higher propagation pressure, which can be attributed to the higher shear stress, hence, a higher susceptibility to shear yielding and dilation, and the resulting higher compressive stresses in the minimum stress direction. For the same reason, the smaller maximum principal stress resulted in a longer fracture. More shearing enhances the permeability of the reservoir, which in turn increases leak-off and reduces the fracture length. Also due to larger leak-off, total stresses rise, resulting in a higher fracturing pressure and a shorter fracture.

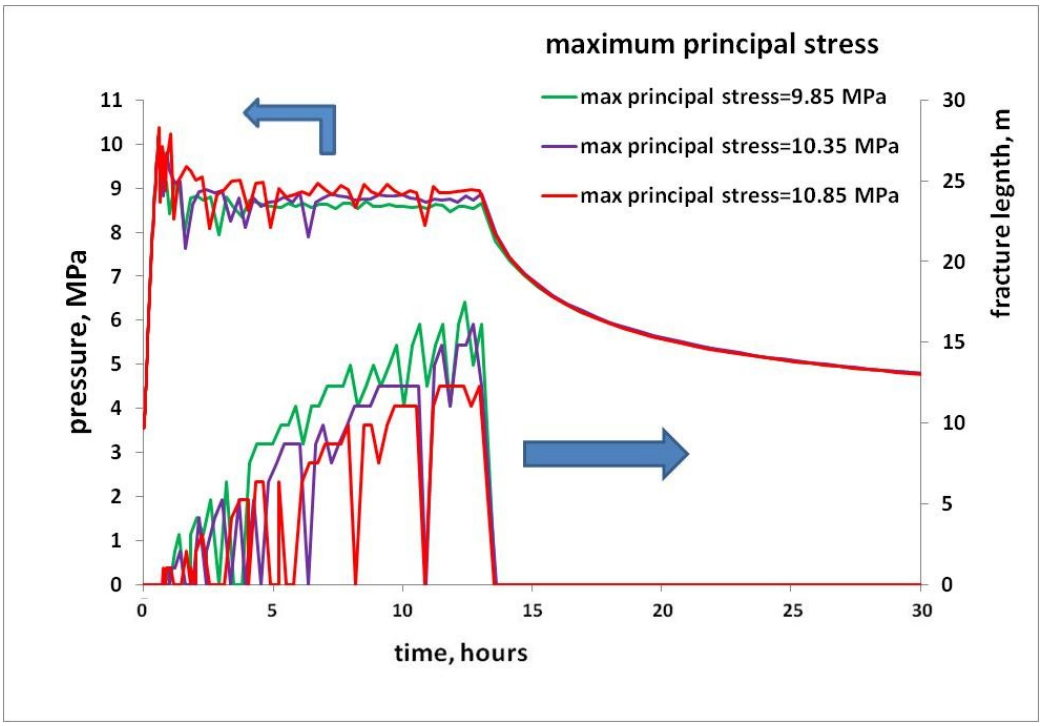

Fig. 5-21: The impact of the maximum principal stress magnitude

The results showed that for the same reservoir and geomechanical conditions, a larger deviatoric stress state resulted in a larger propagation pressure and a shorter fracture.

5.7.3.5 Cohesion

The amount of cohesion influences the shear strength of the reservoir sand, affecting the fluid leak-off due to shear induced permeability, thus impacting the fracturing pressure and length. To examine the influence of the cohesion on the fracturing response, four cohesion values (initial cohesion) of 0.085, 0.425, 0.85 (the base case) and 1.7 MPa were examined and the same ratio (cohesion of the model with respect to the base-case cohesion) was maintained during strain hardening and softening. Fig. 5-22 shows the results.

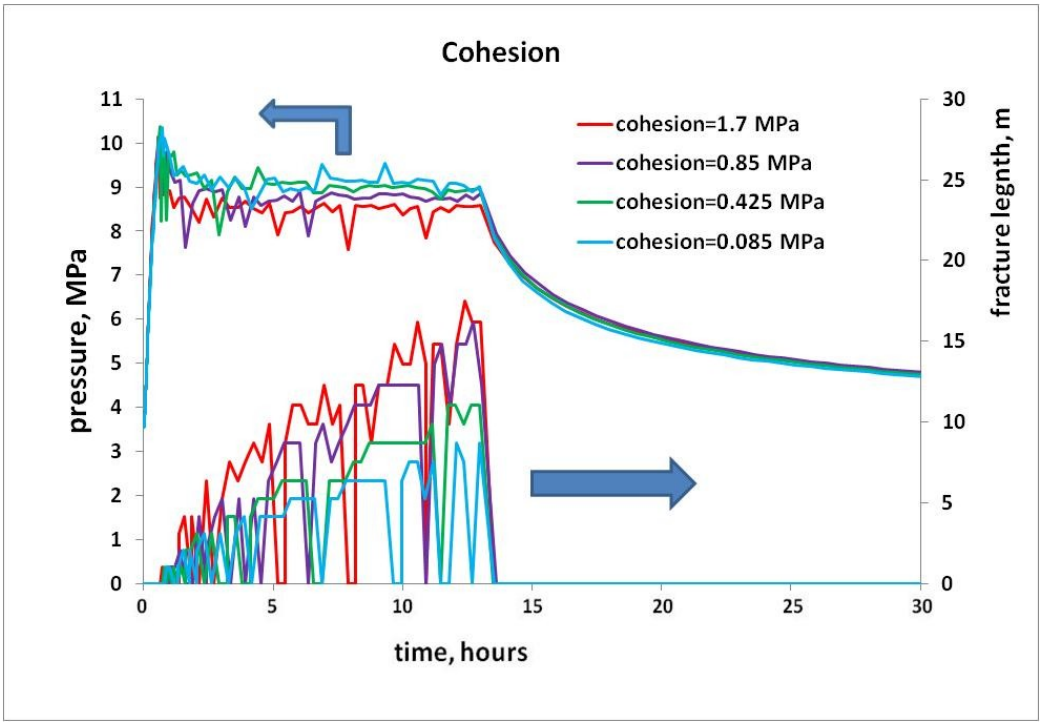

Fig. 5-22: The influence of cohesion on the fracturing response

As expected, the larger cohesion resulted in a longer fracture but lower fracturing pressure. Cohesion values of 0.085, 0.425, 0.85 (the base case) and 1.7 MPa led to the breakdown pressures of 10.36, 10.34, 10.10 and 9.97 MPa, respectively. Also fracture propagation pressures were 9.1, 8.95, 8.75 and 8.55 MPa, respectively.

Results showed that cohesion significantly impacted fracture length. Longer fractures were obtained for larger cohesions due to less shearing and lower leak-off rates from the fracture walls. The low-cohesion case (0.1 MPa) showed cycles of fracture closure and pressure rise that re-opened the fracture during the injection period. This phenomenon can be attributed to the extensive shearing and dilation around the fracture walls and the wellbore. Shearing results in dilation, and increases the magnitude of the local minimum principal stresses. Hence, it tends to close the fracture. To re- open the fracture, higher pressures are needed.

5.7.3.6 Elastic Modulus (E)

The elastic modulus influences the sand deformation and, consequently, the fracture aperture. The elastic modulus is also expected to have a significant impact on the variation of porosity, water saturation, relative permeability, and the leak-off. A sensitivity analysis was performed to study the way in which the oil sands' elastic modulus influences the fracture length and fracturing pressure.

As shown in Fig. 5-23, a lower elastic modulus results in a much shorter fracture with a lower rate of fracture growth. The larger elastic modulus also shows a higher breakdown pressure and a slightly lower propagation pressure. During the shut-in period, the pressure decline rates of the three cases are different. Pressure in the low-E case stabilizes more quickly than in the other cases. The elastic modulus has been the only parameter so far that influences the post-shut-in behavior.

5.7.3.7 Absolute permeability

The impact of the reservoir's absolute permeability on the fracture length and fracturing pressure was also studied through a sensitivity analysis. In addition to the base case (absolute permeability of 300 md), two other absolute permeabilities of 400 and 200 md were examined. The results are shown in Fig. 5-24.

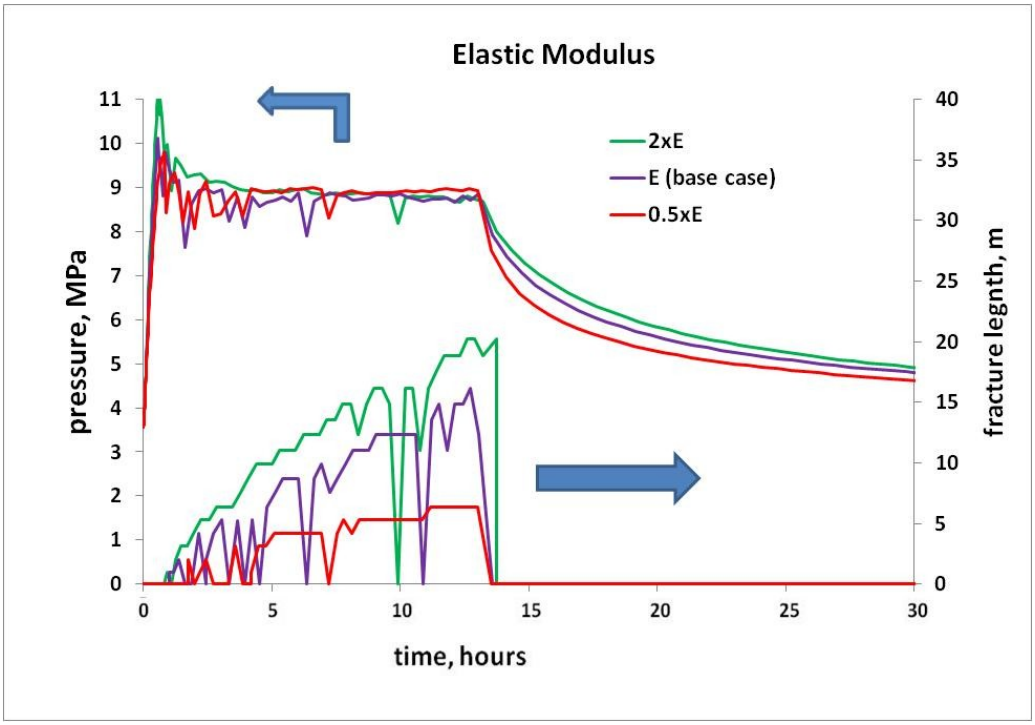

Fig. 5-23: The impact of the elastic modulus on the fracture length and fracturing pressure

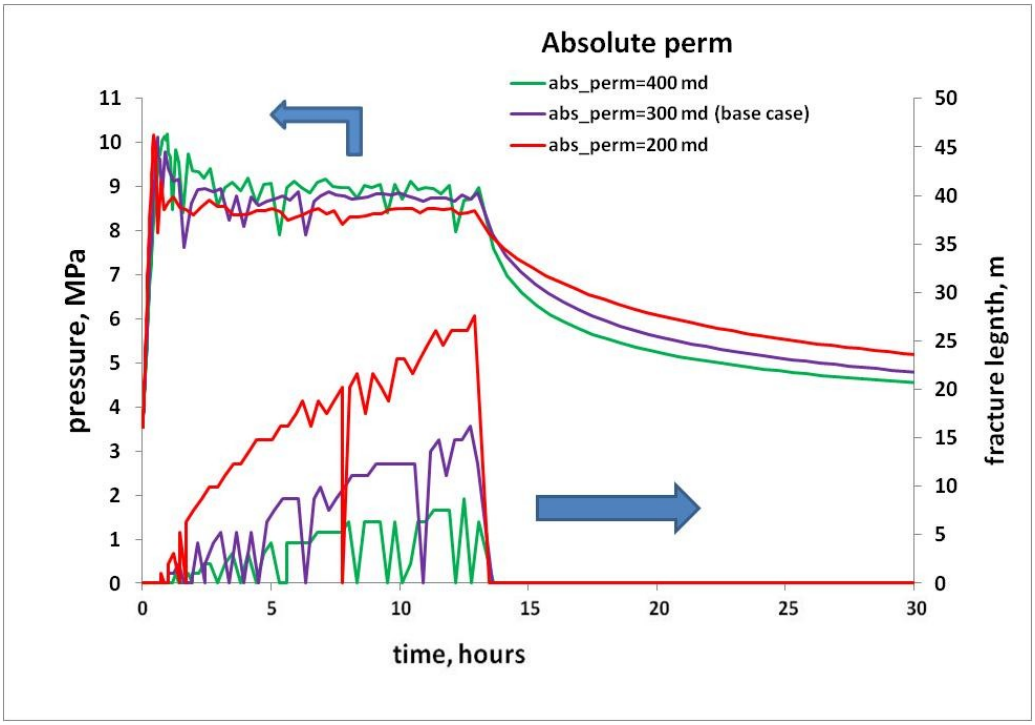

Fig. 5-24: The effect of the reservoir's absolute permeability on the fracture response

All three absolute permeabilities showed the same breakdown pressure, while the propagation pressure was slightly lower for the smaller absolute permeability.

The smaller absolute permeability also showed a significantly longer fracture. Even though the maximum difference in the absolute permeability of the three cases is only 100 md, the two larger absolute permeabilities showed a closer fracture pressure, meaning that the larger the reservoir permeability, the smaller the impact on fracture pressure. Pressures in the larger absolute permeability case stabilized faster and included a lower number of fracture closures and re-openings than the larger permeability cases. The pressure declines during the shut-in period were also quite different.

5.7.3.8 Shear permeability-evolution rate (B parameter).

The B parameter in the Touhidi-Baghini shear permeability model (Touhidi-Baghini, 1998) influences the amount of permeability enhancement with the accumulation of shear deformation, thus affecting the leak-off rate from the fracture walls, and impacting the fracturing pressure and length. The B parameter should be evaluated through permeability measurements during triaxial compression tests. These data were not available for the reservoir being studied and the B value was assumed based on the recommendations of Touhidi-Baghini. To understand the impact of the B parameter on the fracturing response, a sensitivity analysis was performed with respect to this parameter.

Three B_h values of 1, 2 (the base case) and 3 were examined while the B_H/B_h ratio was kept equal to 2. Fig. 5-25 shows the results. All three cases show the same level of breakdown and propagation pressure. However, the larger B parameter shows a slightly shorter fracture which is expected due to a larger water leak-off from the fracture walls. Further, fewer fluctuations in the fracture length were observed for the smaller B parameter, especially at the early injection stages. This could be a function of the smaller permeability at the sheared zone on the fracture walls, allowing less leak-off from the walls. A smaller leak-off results in less shearing, and less variation in stresses and pore pressure near the hydraulic fracture, all of which contribute to more stable fracture growth.

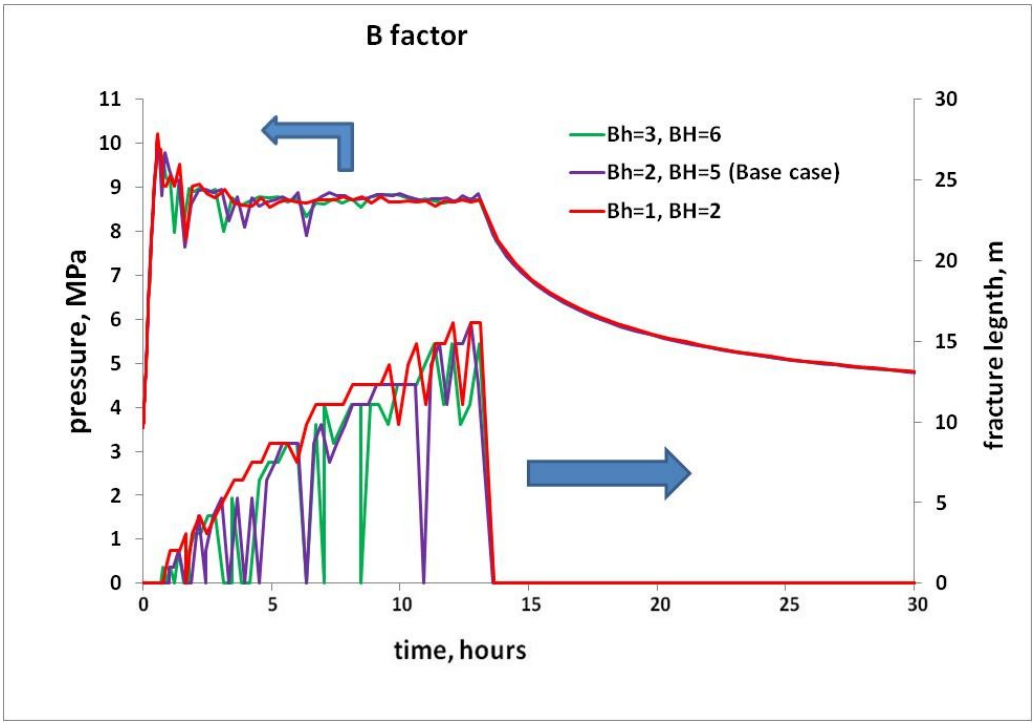

Fig. 5-25: The influence of the shear permeability evolution rate (B parameter)

5.7.3.9 Ramp-up time

A quicker pressure ramp-up results in less leak-off, which impacts the fracturing response. To investigate this effect, four different ramp-up times of 16.5, 33 (base case), 66 and 100 minutes) were examined, as shown in Fig. 5-26.

The figure shows that fracture initiation was delayed for the case with the slower ramp-up. However, there was not a significant variation in the breakdown pressure, nor was in the propagation pressure. A faster injection led to an earlier fracture initiation and a slightly longer fracture.

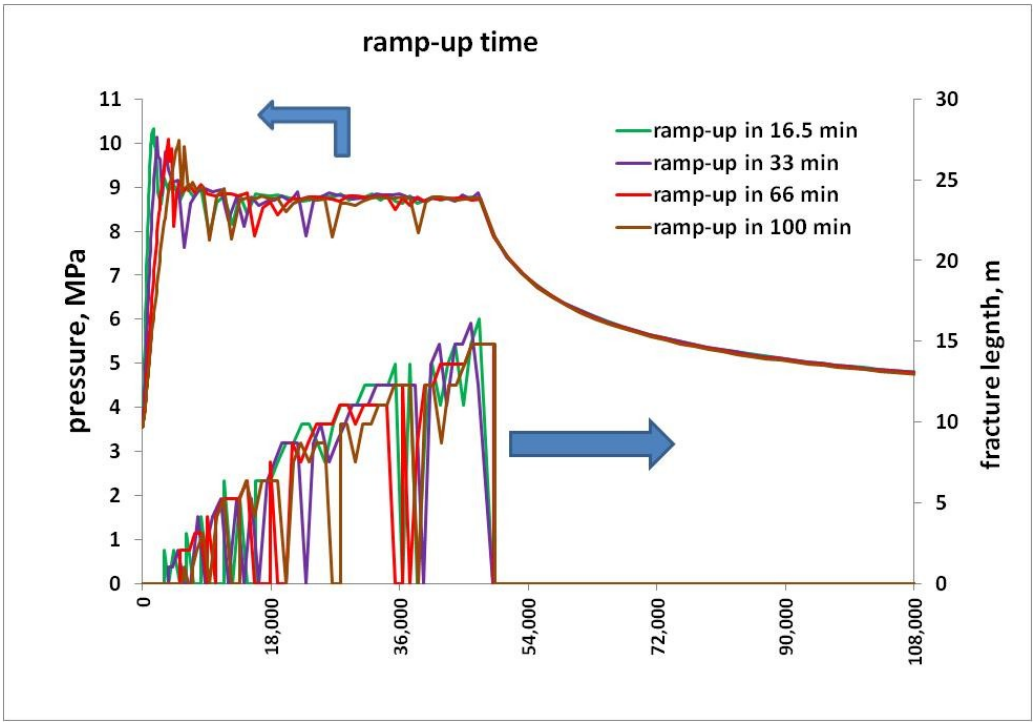

Fig. 5-26: Sensitivity analysis with respect to ramp-up time

5.8 Conclusion

The smeared hydraulic fracture model developed in this research was used to simulate three well tests in a cold oil sands reservoir. Major features of this model include capturing poroelasticity and plasticity, matrix flow, shear and tensile fracturing with the concomitant permeability enhancement (Touhidi-Baghini's shear permeability and the cubic law, respectively), tensile fracture direction, saturation-dependent permeability, stress-dependent stiffness and gradual degradation of oil sands due to dilatant shear deformation. The model could properly initiate and propagate a hydraulic fracture without having to predefine the fracture direction or location.

Simulation results indicate that no tensile hydraulic fracturing formed during the well tests. To investigate the initiation and propagation of a tensile fracture in the reservoir, a hydraulic fracture simulation was carried out using a higher flow rate of 40 m^3/day for a duration of 13 hours. A series of sensitivity studies was conducted with respect to different parameters.

Results indicated that the saturation-dependent relative permeability and the permeability alteration due to shear dilation governed the injection response of the oil sands. The saturation-dependent relative permeability influenced the injectivity during the elastic deformation of the oil sands. After shearing, however, the shear dilation of the oil sands, as well as poroelasticity, influenced the injection response. The initiation and propagation pressures of a tensile fracture for the reservoir condition were 10.1 and 8.8 MPa, which are comparable to the magnitudes of the minimum and maximum principal stresses (7.2 and 10.35 MPa, respectively). Such a large breakdown pressure can be attributed to the poroelasticity and shear dilative phenomena.

Keeping the flow rate constant at 40 m^3/day, the sensitivity analysis showed a higher fracturing pressure and a shorter fracture for a higher tensile strength. Higher minimum in situ stresses increased the fracturing pressure but reduced the fracture length. The increase in fracturing pressure was more significant than the increase in the magnitude of the minimum in situ stress. A 0.5 MPa increase in the minimum in situ stress caused more than a 0.75 MPa increase in the breakdown and propagation pressures.

Larger maximum principal stress also resulted in a larger propagation pressure and a shorter fracture due to higher shearing and larger dilation around the wellbore/tensile fracture. More shearing/dilation locally increased the total stresses and enhanced the permeability in the reservoir, which elevated the leak-off and reduced the fracture length.

Larger cohesion resulted in a longer fracture but lower fracture initiation and propagation pressures. Fracture length was highly influenced by the cohesion value. Larger cohesion induced a longer fracture due to less shearing and lower leak-off rates from the fracture walls. The low-cohesion case (0.1 MPa) induced cycles of fracture closure and pressure rise to re-open the fracture during the injection period. This phenomenon can be attributed to the extensive shearing and dilation around the fracture walls and the wellbore. The shearing increased the magnitude of the minimum principal stress locally and closed the fracture. To re-

open the fracture, additional pressure would be needed. For the same reason, fracturing pressure increased over time in the low-cohesion case.

A smaller elastic modulus (half the base case E) resulted in a significantly shorter fracture with a lower rate of fracture growth. The larger elastic modulus also showed a significantly larger breakdown pressure. The smaller elastic modulus showed a slightly larger fracture propagation pressure due to the extra deformation and leak-off from the sheared zone.

The value of the absolute permeability of the reservoir did not affect the breakdown pressure but resulted in a lower propagation pressure and a longer fracture for smaller absolute permeability.

For the range of geomechanical and flow properties used in this research, the most influential parameters affecting the (tensile) fracturing pressure of a reservoir were (based on their impact level) the magnitude of the minimum in situ stress, the reservoir's absolute permeability, the cohesion and tensile strength of the reservoir rock and the magnitude of the maximum in situ stress. Understanding these parameters and their variation for a specific reservoir is of paramount importance in order to assess a reservoir's hydraulic fracturing pressure.

The B parameter did not impact the reservoir breakdown and propagation pressures. However, a slightly shorter fracture was found for larger B values, which could be attributed to a larger water leak-off from the fracture walls. A smaller B parameter resulted in a smaller leak-off, less shearing and less variation in the magnitudes of total stresses near the hydraulic fracture, hence, a smaller number of fracture closure/opening cycles.

A shear failure zone formed around the tensile fracture and beyond the fracture tip. This did not affect the direction of the tensile fracture but influenced the fracturing pressure and length.

Chapter 6: Conclusion and discussion

6.1 Summary

This research presented the development of a comprehensive 2D numerical model to simulate a hydraulic fracture based on the smeared fracture approach. The model included both the reservoir flow and geomechanics aspects of a reservoir-fracturing response. The reservoir module calculated the pore pressures and the geomechanics module delivered the enhanced porosities and permeabilities induced by pore pressure variations. The two modules were iteratively sequenced. The model was able to incorporate the full permeability matrix with the shear and tensile fractures.

The proposed model can consider multiple shear and tensile fractures. Unlike classic models, this model added enough physics to make it possible to describe phenomena such as poroelasticity and plasticity, matrix and fracture flow, stress-dependent elastic properties, shear and tensile fracturing and the associated permeability enhancement, gradual degradation due to dilatant shear deformation, and strain localization in weak/unconsolidated sandstones. In addition, the model does not require the user to know the fracture direction and location at the beginning of the simulation.

The model was verified against available data in the literature for fracture propagation in an impermeable matrix with cohesion-hardening. The model was verified for all the cases. After reasonable agreement was obtained, the model was used to simulate a large-scale laboratory experiment of hydraulic fracturing in cohesionless sands. Although the injection pressure was larger than both the minimum and maximum principal stresses, the experimental results indicated that no tensile fracture was induced in the sample. The smeared fracture model was successfully used to simulate the experiment.

The model was also used to simulate a series of well tests in oil sands during cold-water injection. The simulations indicated that no tensile hydraulic fractures developed during the well tests and that the failure mode was all in Mode II, i.e.,

shear failure. At injection pressures below the vertical stress for the specified condition, shear failure dominated. Results showed that saturation-dependent relative permeability and the development of shear failure highly influence the fracturing process.

This research also involved the study of initiating and propagating a tensile fracture in an oil sand reservoir using a higher flow rate. Results showed that poroelastic effects, stress-dependent stiffness, and shear yielding (failure) result in breakdown and propagation pressures larger than the maximum in situ stress.

A series of sensitivity studies was conducted with respect to flow and geomechanical parameters to assess the impact of these parameters on fracture response. The following are the high-level findings:

The sensitivity analysis against the magnitude of the minimum in situ stress showed that the enhancement in fracturing pressure is more significant than the increment in the magnitude of the minimum in situ stress.

Fracture propagation pressure was directly and fracture length was inversely affected by the magnitude of the maximum principal stress. Larger deviatoric stress induced more shearing and larger dilation around the wellbore and around the tensile fracture. More shearing/dilation enhances reservoir permeability, increases leak-off and eventually raises the magnitude of total stresses in the reservoir.

Results also showed that propagation pressure drops as cohesion increases (stronger rocks). A larger cohesion results in a longer fracture due to less shearing and a lower rate of leak-off from the fracture walls. It was also found that unlike the high-cohesion cases, the pressure history in a low-cohesion reservoir involves cycles of pressure rise and drop to re-open the fracture due to the extensive shearing and dilation around the fracture walls and the wellbore. For the same reason, fracturing pressure also increases with time in low-cohesion cases.

A smaller elastic modulus may result in a significantly shorter fracture. Stiffer reservoirs are expected to have a higher breakdown pressure but lower propagation pressure.

The absolute permeability of a reservoir does not affect the breakdown pressure. However, propagation pressure is lower and the fracture is expected to be longer in low-permeability reservoirs. Similar to the impact of an elastic modulus, the absolute permeability of oil sands controls the rate of pressure decline during the shut-in period. With a larger absolute permeability, pressure stabilizes faster after shut-in.

Within the examined range of B (Shear-permeability evolution rate) values, it was found that the B parameter does not have any impact on the reservoir breakdown and propagation pressure. However, a shear-permeability rate results in a slightly shorter fracture due to larger water leak-off from the fracture walls.

The simulations show that the model enables an accurate simulation of the fracturing response of weak rocks, especially weakly/unconsolidated sandstones. Such a response couldn't be fully addressed by classic models. In addition, it was concluded that the fracturing pressure of these geomaterials is expected to be in the range of the maximum principal stress and higher. Through the sensitivity analyses, the understanding of cold-water fracturing of oil sand reservoirs has also been enhanced.

6.2 Major findings and contributions

In this research, a method was presented to implement the cubic law to describe the flow inside a tensile fracture in a continuum-smeared tensile fracture model together with the appropriate mechanical behavior. A smeared shear failure scheme (including both geomechanical and fluid flow aspects) was also implemented in the model and was added to the smeared tensile fracture model. The model was validated and verified against existing research in the literature, a large-scale laboratory experiment, and a series of well tests in oil sands. For the latter, assuming a single-phase flow (during cold water injection), an equation

was derived to calculate the relative permeability of oil sands to water based on water saturation (and its variation) at any given time. This parameter is a function of porosity and volumetric strain and their variations.

This research showed that the fracturing pressure of cohesionless sand and unconsolidated oil sands is not only larger than the initial minimum principal stress, but can also be in the range of the maximum principal stress or larger.

Poroelasticity effects, stress-dependent stiffness, shearing and shear-enhanced permeability as well as dilative shear behavior are the main parameters that cause high fracture pressure. Shear-enhanced permeability is a significant factor which must be considered in a hydraulic fracturing simulation. At pressures lower than the maximum principal stress, shear strength, shear-enhanced permeability and poroelasticity are the main factors controlling a reservoir's fracturing response. In all the cases simulated in this research, the fracturing pressure was found to be in the range of the maximum principal stress or higher. Parameters such as tensile strength, matrix permeability, shear strength, shear-enhanced permeability rate, stress-dependent stiffness of the reservoir rock, in situ stress levels and fluid viscosity influenced the fracturing response.

Further, for the range of geomechanical and flow properties used in this research, the most influential parameters that impact the (tensile) fracturing pressure of a reservoir are (based on their impact level) the magnitude of the minimum in situ stress, the reservoir absolute permeability, cohesion and tensile strength of the reservoir rock and the magnitude of the maximum in situ stress. Understanding these parameters and their variations for a specific reservoir is of paramount importance in order to assess the reservoir's hydraulic fracturing pressure.

6.3 Recommendation for future work

The developed smeared hydraulic fracture model can be a framework to which more features can be added. These features may include:

1. Extension to a 3D model to incorporate 3D-fluid flow

2. Multi-phase flow and thermal effects
3. Frac-packing model to simulate proppant transport and frac-pack effects
4. Non-Darcy fracture flow

In addition, this model makes it possible to study the impact of shear banding at the fracture tip in hard low permeability rocks and its impact on potential fracture deviation. The model is also a proper tool for fracturing shale gas and shale oil reservoirs if the appropriate constitutive behavior of shales is calibrated and implemented.

Bibliography

Abass, H. H., Hedayati, S. and Meadows, D. L. 1996. Nonplanar Fracture Propagation From a Horizontal Wellbore: Experimental Study. SPE Production & Operations. 24823

Adachi, J., Siebrits, E., Peirce, A. and Desroches, J. 2007. Computer simulation of hydraulic fractures. International Journal of Rock Mechanics and Mining Sciences **44**: 739-757.

Adams, J. and Rowe, C. 2013. Differentiating Applications of Hydraulic Fracturing. International Society for Rock Mechanics.

Anderson, T. L. 1991. Fracture Mechanics: Fundamentals and Applications. CRC Press, Boca Raton.

Armirola, F., Pinto, C., Machacon, M., Lastre, M., Milne, A. W. and Bravo, O. 2011. Optimizing Fracture Geometry and Productivity in High Permeability Reservoirs. SPE European Formation Damage Conference, Noordwijk, The Netherlands. 143785

Aud, W. W., Wright, T. B., Cipolla, C. L. and Harkrider, J. D. 1994. The Effect of Viscosity on Near-Wellbore Tortuosity and Premature Screenouts. SPE Annual Technical Conference and Exhibition, New Orleans, Louisiana. 28492

Aydin, A. 2001. Fracture void structure: implications for flow, transport and deformation. Environmental Geology **40**: 672-677.

Barenblatt, G. I. 1962. The mathematical theory of equilibrium cracks in brittle fracture. Advances in Applied Mechanics **7**: 55-129.

Bažant, Z. 1984. Microplane Model for Strain-Controlled Inelastic Behaviour. Page 15 *in* Mechanics of Engineering Material. John Wiley & Sons.

Bažant, Z. and Oh, B. 1983. Crack band theory for fracture of concrete. Materials and Structures **16**: 155-177.

Bažant, Z. P., Lin, F.-B. and Lippmann, H. 1993. Fracture energy release and size effect in borehole breakout. International Journal for Numerical and Analytical Methods in Geomechanics **17**: 1-14.

Bésuelle, P., Desrues, J. and Raynaud, S. 2000. Experimental characterisation of the localisation phenomenon inside a Vosges sandstone in a triaxial cell. International Journal of Rock Mechanics and Mining Sciences **37**: 1223-1237.

Bieniawski, Z. T., Denkhaus, H. G. and Vogler, U. W. 1969. Failure of fractured rock. International Journal of Rock Mechanics and Mining Sciences & Geomechanics Abstracts **6**: 323-341.

Bohloli, B. and de Pater, C. J. 2006. Experimental study on hydraulic fracturing of soft rocks: Influence of fluid rheology and confining stress. Journal of Petroleum Science and Engineering **53**: 1-12.

Chalaturnyk, R. J. 1996. Geomechanics of the steam-assisted gravity drainage process in heavy oil reservoirs. NN10577. University of Alberta (Canada), Canada.

Chang, H. 2004. Hydraulic Fracturing in Particulate Material. PhD Thesis. Georgia Institue of Technology, Georgia, Atlanta.

Chen, Z., Qian, J.-z., Luo, S.-h. and Zhan, H.-b. 2009. Experimental study of friction factor for groundwater flow in a single rough fracture. Journal of Hydrodynamics, Ser. B **21**: 820-825.

Chin, L. Y. and Montgomery, C. T. 2004. A Numerical Model for Simulating Solid Waste Injection in Soft Rock Reservoirs. SPE Annual Technical Conference and Exhibition, Houston, Texas. 90507

Cleary, M. P., Johnson, D. E., KogsbÃ¸ll, H.-H., Owens, K. A., Perry, K. F., Pater, C. J. d., Stachel, A., Schmidt, H. and Tambini, M. 1993. Field Implementation of Proppant Slugs To Avoid Premature Screen-Out of Hydraulic Fractures With Adequate Proppant Concentration. Low Permeability Reservoirs Symposium, Denver, Colorado. 25892

Cook, B. K., Lee, M. Y., DiGiovanni, A. A., Bronowski, D. R., Perkins, E. D. and Williams, J. R. 2004. Discrete Element Modeling Applied to Laboratory Simulation of Near-Wellbore Mechanics. International Journal of Geomechanics **6**: 19-27.

Crook, T., Willson, S., Yu, J. G. and Owen, R. 2003. Computational modelling of the localized deformation associated with borehole breakout in quasi-brittle materials. Journal of Petroleum Science and Engineering **38**: 177-186.

Daneshy, A. A. 2003. Off-Balance Growth: A New Concept in Hydraulic Fracturing. SPE Journal of Petroleum Technology. 80992

Daneshy, A. A. 2005. Proppant Distribution and Flowback in Off-Balance Hydraulic Fractures. SPE Production & Operations. 89889-PA

Daneshy, A. A. 2011. Hydraulic Fracturing of Horizontal Wells: Issues and Insights. Society of Petroleum Engineers.

Das, B. M. 2008. Advanced Soil Mechancis. 3rd edition. Taylor and Francis, New York.

de Borst, R. and Nauta, P. 1985. Non-Orthogonal Cracks in a Smeared Finite Element Model. Engineering Computations **2**: 12.

de Pater, C. J. and Dong, Y. 2007. Experimental Study of Hydraulic Fracturing in Sand as a Function of Stress and Fluid Rheology. Page 10 SPE Hydraulic Fracturing Technology Conference. Society of Petroleum Engineers, College Station, Texas USA. SPE 63233

de Pater, H. 1996. Delf Fracturing Consersium, internal presentation.

Desai, C. S. 2001. Mechanics of materials and interfaces: the disturbed state concept. CRC Press.

Di Lullo, G., Curtis, J. and Gomez, J. 2004. A Fresh Look At Stimulating Unconsolidated Sands With Proppant-Laden Fluids. Page 5 SPE Annual Technical Conference and Exhibition. Society of Petroleum Engineers, Houston, Texas. 90813-MS

Dusseault, M. B. 2001. Comparing Venezuelan and Canadian Heavy Oil and Tar Sands. Canadian International Petroleum Conference, Calgary, AB, Canada.

Dusseault, M. B., Danyluk, P. G. and Bilak, R. A. 1998. Slurry Fracture Injection of Solid and Liquid Heavy Oil Wastes. Society of Petroleum Engineers.

Economides, M. J., Oligney, R. E. and Valkó, P. t. 2002. Unified Fracture Design: Bridging the gap between theory and practice. Orsa Press.

Economides, M. J. and Wang, X. 2010. Design Flaws in Hydraulic Fracturing. SPE International Symposium and Exhibiton on Formation Damage Control. Society of Petroleum Engineers, Lafayette, Louisiana, USA. 127870

Gidley, J. L., Holditch, S. A., Nierode, D. E. and Veatch, R. W., Jr. 1989. Recent Advances in Hydraulic Fracturing. Society of Petroleum Engineers, Dallas, Texas.

Gil, I. 2005. Hydraulic fracturing of poorly consolidated formations: Considerations on rock properties and failure mechanisms. PhD Thesis. University of Oklahoma, Oklahoma.

Gil, I. and Roegiers, J. 2006. The Effect of Fluid Leakoff on Rock Failure Mechanisms During Frac-Pack Treatments. Page 7 International Symposium and Exhibition on Formation Damage Control. Society of Petroleum Engineers, Lafayette, Louisiana U.S.A. 98170

Golder Associates Ltd. 1992. Laboratory Simulation and Constitutive Behavior for Hydraulic Fracture Propagation in Oil Sands, Final Report (Phase 2).

Golovin, E., Jasarevic, H., Chudnovsky, A., Dudley, J. W. and Wong, G. K. 2010. Observation And Characterization of Hydraulic Fracture In Cohesionless Sand. Page 9 44th U.S. Rock Mechanics Symposium and 5th U.S.-Canada Rock Mechanics Symposium. American Rock Mechanics Association, Salt Lake City, Utah. ARMA10-359

Goodman, R. E. 1989. Introduction to rock mechanics. John Wiley & Sons.

Hagoort, J. 1978. Hydraulic Fracturing Pressures In Permeable Subsurface Layers. Page 28. Society of Petroleum Engineers. 7110

Hagoort, J., Weatherill, B. D. and Settari, A. 1980. Modeling the Propagation of Waterflood-Induced Hydraulic Fractures. SPE Journal **20**: 293-303. 7412

Hannan, S. S. and Nzekwu, B. I. 1992. AOSTRA mini-frac manual: Field testing analysis and interpretation procedures. Alberta Oil Sands Technology and Research Authority.

He, Q., Suorineni, F. and Oh, J. 2015. Modeling Interaction between Natural Fractures and Hydraulic Fractures in Block Cave Mining. American Rock Mechanics Association.

Howard, G. C. and Fast, C. R. 1970. Hydraulic Fracturing. Millet the Printer, Dallas TX.

Hu, D. W., Zhou, H., Zhang, F. and Shao, J. F. 2010. Evolution of poroelastic properties and permeability in damaged sandstone. International Journal of Rock Mechanics and Mining Sciences **47**: 962-973.

Huang, H., Zhang, F., Callahan and Ayoub, J. 2011. Fluid Injection Experiments in Two-dimensional Porous Media. Page 8 SPE Hydraulic Fracturing Technology Conference. Society of Petroleum Engineers, The Woodlands, Texas, USA. 140502-MS

Huitt, J. L. 1956. Fluid flow in simulated fractures. AIChE Journal **2**: 259-264.

Itasca Consulting Group Inc. 2011. FLAC Fast Lagrangian Analysis of Continua: User's Guide, Minneapolis, Minnesota.

Jafarpour, M., Rahmati, H., Azadbakht, S., Nouri, A., Chan, D. and Vaziri, H. 2012. Determination of mobilized strength properties of degrading sandstone. Soils and Foundations **52**: 658-667.

Jasarevic, H., Golovin, E., Chudnovsky, A., Dudley, J. W. and Wong, G. K. 2010. Observation And Modeling of Hydraulic Fracture Initiation In Cohesionless Sand. Page 9 44th U.S. Rock Mechanics Symposium and 5th U.S.-Canada Rock Mechanics Symposium. American Rock Mechanics Association, Salt Lake City, Utah. ARMA 10-360

Ji, L. 2008. Modeling Hydraulic Fracturing Fully Coupled with Reservoir and Geomechanical Simulation. Ph.D. Dissertation. University of Calgary, Calgary, AB.

Ji, L., Settari, A. and Sullivan, R. B. 2006. A New Approach to Hydraulic Fracturing Modeling— Fully Coupled With Geomechanical and Reservoir Simulation. SPE Europec/EAGE Annual Conference and Exhibition: 9.

Ji, L., Settari, A. and Sullivan, R. B. 2009. A Novel Hydraulic Fracturing Model Fully Coupled With Geomechanics and Reservoir Simulation. SPE Journal **14**: 423-430. SPE-110845-PA

Ji, L., Settari, A., Sullivan, R. B. and Orr, D. 2004. Methods For Modeling Dynamic Fractures In Coupled Reservoir And Geomechanics Simulation. Page 9 SPE Annual Technical Conference and Exhibition. SPE, Houston, Texas. 90874-MS

Khodaverdian, M. and McElfresh, P. 2000. Hydraulic Fracturing Stimulation in Poorly Consolidated Sand: Mechanisms and Consequences. Page 13 SPE Annual Technical Conference and Exhibition. Society of Petroleum Engineers, Dallas, Texas. SPE 63233

Khodaverdian, M., Sorop, T., Postif, S. and Hoek, P. V. d. 2010. Polymer Flooding in Unconsolidated-Sand Formations: Fracturing and Geomechanical Considerations. SPE Production & Operations **25**: 211-222. SPE 121280

Kisman, K. E. and Yeung, K. C. 1995. Numerical Study of the SAGD Process in the Burnt Lake Oil Sands Lease. Society of Petroleum Engineers.

Klerck, P. A. 2000. The Finite Element Modelling of Discrete Fracture in Quasi-Brittle Materials. PhD Thesis. University of Wales Swansea.

Kumar, D., Gutierrez, M., Frash, L. P. and Hampton, J. C. 2015. Numerical Modeling of Experimental Hydraulic Fracture Initiation and Propagation in Enhanced Geothermal Systems. American Rock Mechanics Association.

Leshchyshyn, T. H., Seffari, A. and Ali, S. M. F. 1996. Minifrac Analysis of Shear Parting In Alberta Reservoirs And Its Impact Towards On-site Fracture Design. SPE Annual Technical Meeting, Calgary, Alberta. 96-79

Li, D. and Engler, T. W. 2001. Literature Review on Correlations of the Non-Darcy Coefficient. SPE Permian Basin Oil and Gas Recovery Conference. 2001,. Society of Petroleum Engineers Inc., Midland, Texas. 00070015

Li, P. and Chalaturnyk, R. J. 2006. Permeability Variations Associated With Shearing and Isotropic Unloading During the SAGD Process. Journal of Canadian Petroleum Technology. 06-01-05

Lian, Z. L., Wang, X. X., Wu1, H. A., Xue1, B., Zhang, J. and Zhang, S. C. 2006. Modeling and Simulation of Hydraulic Fracturing Propagation in Permeable Reservoirs. Key Engineering Materials **324-325**: 383-386.

Lomize, G. M. 1951. Filtratsiya v Treshchinovatykh Porodakh (Flow in Fractured Rocks). Gosenergoizdat, Moscow.

Louis, C. 1969. A Study of Groundwater Flow in Jointed Rock and Its Influence on the Stability of Rock Masses. Imperial College of Science and Technology, London.

Mahrer, K. D., Aud, W. W. and Hansen, J. T. 1996. Far-Field Hydraulic Fracture Geometry: A Changing Paradigm. SPE Annual Technical Conference and Exhibition, Denver, Colorado. 36441

Marongiu-Porcu, M., Liu, W. and Economides, M. J. 2010. Flaws in Fracture Designs: A Continuing Problem. Canadian Unconventional Resources and International Petroleum Conference. Society of Petroleum Engineers, Calgary, Alberta, Canada. 137377

McElfresh, P. M., Khodaverdian, M. F. and Baycroft, P. D. 2002. Frac Packing in Soft Formations: Low Efficiency Fluids Exacerbate Formation Damage. Page 12 International Symposium and Exhibition on Formation Damage Control. Society of Petroleum Engineers, Lafayette, Louisiana.

Nagel, N., Gil, I., Sanchez-Nagel, M. and Damjanac, B. 2011. Simulating Hydraulic Fracturing in Real Fractured Rocks - Overcoming the Limits of Pseudo3D Models. Page 15 SPE Hydraulic Fracturing Technology Conference. Society of Petroleum Engineers, The Woodlands, Texas, USA. SPE-140480-MS

Nghiem, L. X., Forsyth Jr., P. A. and Behie, A. 1984. A Fully Implicit Hydraulic Fracture Model. SPE Journal of Petroleum Technology. 10506

Nicholl, M. J., Rajaram, H., Glass, R. J. and Detwiler, R. 1999. Saturated flow in a single fracture: evaluation of the Reynolds Equation in measured aperture fields. Water Resour. Res. **35**: 3361-3373.

Nouri, A., Kuru, E. and Vaziri, H. 2009. Elastoplastic Modelling of Sand Production Using Fracture Energy Regularization Method. 09-04-64

Olson, J. E., Holder, J. and Hosseini, S. M. 2011. Soft Rock Fracturing Geometry and Failure Mode in Lab Experiments. Page 9 SPE Hydraulic Fracturing Technology Conference. SPE, The Woodlands, Texas, USA. SPE 140543

Onaisi, A., Ochi, J., Mainguy, M. and Souillard, P. A. 2011. Modelling Non-matrix Flow and Seals Integrity in Soft Sand Reservoirs. SPE European Formation Damage Conference. Society of Petroleum Engineers, Noordwijk, The Netherlands. 144801

Oron, A. P. and Berkowitz, B. 1998. Flow in rock fractures: The local cubic law assumption reexamined. Water Resour. Res. **34**: 2811-2825.

Osorio, G. and Lopez, C. F. 2009. Geomechanical Factors Affecting the Hydraulic Fracturing Performance in a Geomechanically Complex, Tectonically Active Area in Colombia. Latin American and Caribbean Petroleum Engineering Conference, Cartagena de Indias, Colombia. 122315

Pak, A. 1997. Numerical Modeling of Hydraulic Fracturing. PhD Thesis. Alberta, Edmonton.

Pak, A. and Chan, D. H. 2004. A Fully Implicit Single Phase T-H-M Fracture Model for Modelling Hydraulic Fracturing in Oil Sands. Journal of Canadian Petroleum Technology **43**: 10.

Palmer, I. D., Moschovidis, Z. A. and Cameron, J. R. 2007. Modeling Shear Failure and Stimulation of the Barnett Shale After Hydraulic Fracturing. SPE Hydraulic Fracturing Technology Conference, College Station, Texas, U.S.A. 106113

Papanastasiou, P. 1997a. The influence of plasticity in hydraulic fracturing. International Journal of Fracture **84**: 61-79.

Papanastasiou, P. 1999. An efficient algorithm for propagating fluid-driven fractures. Computational Mechanics **24**: 258-267.

Papanastasiou, P. C. 1997b. A coupled Elastoplastic Hydraulic Fracturing Model. International Journal of Rock Mechanics and Mining Sciences **34**: 240.e241-240.e215.

Parrish, D. R. 1963. Fluid Flow in Rough Fractures. Page 9 University of Oklahoma-SPE Production Research Symposium. Society of Petroleum Engineers, Norman, Oklahoma. 563-MS

Pietruszczak, S. and Mróz, Z. 1981. Finite element analysis of deformation of strain-softening materials. International Journal for Numerical Methods in Engineering **17**: 327-334.

Plewes, H. D. 1987. Undrained Strength of Athabasca Oil Sands. University of Alberta, Edmonton, Alberta.

Qian, J., Zhan, H., Chen, Z. and Ye, H. 2011. Experimental study of solute transport under non-Darcian flow in a single fracture. Journal of Hydrology **399**: 246-254.

Qian, J., Zhan, H., Luo, S. and Zhao, W. 2007. Experimental evidence of scale-dependent hydraulic conductivity for fully developed turbulent flow in a single fracture. Journal of Hydrology **339**: 206-215.

Qian, J., Zhan, H., Zhao, W. and Sun, F. 2005. Experimental study of turbulent unconfined groundwater flow in a single fracture. Journal of Hydrology **311**: 134-142.

Rahmati, H. 2013. Micromechanical Study of Borehole Breakout Mechanism. University of Alberta, Edmonton.

Rahmati, H., Nouri, A., Vaziri, H. and Chan, D. 2012. Validation of Predicted Cumulative Sand and Sand Rate Against Physical-Model Test.

Rege, N. 1996. Computational modeling of granular Materials. Thesis. MIT, Cambridge, Mass.

Reynolds, M. M. and Buendia, J. 2017. Permanently Sequester Anthropogenic Carbon Dioxide - Through Hydraulic Fracturing. Society of Petroleum Engineers.

Settari, A. 1980. Simulation of Hydraulic Fracturing Processes. SPE Journal **20**: 487-500. 7693-PA

Settari, A. 1988. Modeling of Fracture and Deformation Processes in Oil Sands. Page 14 4th UNITAR/UNDP Conference on Heavy Crude and Tar Sands, Edmonton, AB, Canada. Paper No. 43

Settari, A., Ito, Y. and Jha, K. N. 1992. Coupling Of A Fracture Mechanics Model And A Thermal Reservoir Simulator For Tar Sands. 92-09-02

Settari, A., Kry, P. R. and Yee, C. T. 1989. Coupling Of Fluid Flow And Soil Behaviour To Model Injection Into Uncemented Oil Sands. The Journal of Canadian Petroleum Technology **28**: 12. 89-01-08

Settari, A., Puchyr, P. J. and Bachman, R. C. 1990. Partially Decoupled Modeling of Hydraulic Fracturing Processes. SPE Production Engineering **8**: 8. SPE 16031

Settari, A., Sullivan, R. B. and Bachman, R. C. 2002a. The Modeling of the Effect of Water Blockage and Geomechanics in Waterfracs. SPE Annual Technical Conference and Exhibition, San Antonio, Texas. 77600

Settari, A., Sullivan, R. B., Walters, D. A. and Wawrzynek, P. A. 2002b. 3-D Analysis and Prediction of Microseismicity in Fracturing by Coupled Geomechanical Modeling. SPE Gas Technology Symposium, Calgary, Alberta, Canada. 75714

Suidan, M. and Schnobrich, W. C. 1973. Finite Element Analysis of Teinforced Concrete. Journal of the Structural Division, ASCE **99**: 12.

Sulem, J., Vardoulakis, I., Papamichos, E., Oulahna, A. and Tronvoll, J. 1999. Elasto-plastic modelling of Red Wildmoor sandstone. Mechanics of Cohesive-frictional Materials **4**: 215-245.

Taghipoor, S., Nouri, A., Chan, D. and Vaziri, H. 2013. Numerical Modeling of Hydraulic Fracturing in Weakly Consolidated Sandstones Using Smeared Fracture Approach. Canadian Energy Technology and Inovation (CETI) Journal **1**: 11.

Tortike, W. S. and Ali, S. M. F. 1993. Reservoir Simulation Integrated with Geomechanics. Journal of Canadian Petroleum Technology **32**. PETSOC-93-05-02

Touhidi-Baghini, A. 1998. Absolute permeability of McMurray Formation oil sands at low confining stresses. PhD Thesis. University of Alberta, Edmonton.

Tran, D., Settari, A. and Nghiem, L. 2004. New Iterative Coupling Between a Reservoir Simulator and a Geomechanics Module. SPE Journal **9**: 362-369. 00088989

van Dam, D. B., Papanastasiou, P. and Pater, C. J. d. 2000. Impact of Rock Plasticity on Hydraulic Fracture Propagation and Closure. SPE Annual Technical Conference and Exhibition. Copyright 2000, Society of Petroleum Engineers Inc., Dallas, Texas. 63172

Vardoulakis, I. and Sulem, J. 1995. Bifurcation analysis in geomechanics. Blackie.

Vermeer, P. A. and De Borst, R. 1984. Non-Associated Plasticity for Soils, Concrete and Rock. **350**: 163-196.

Waite, M. E., Ge, S. and Spetzler, H. 1999. A new conceptual model for fluid flow in discrete fractures: An experimental and numerical study. J. Geophys. Res. **104**: 13049-13059.

Waite, M. E., Ge, S., Spetzler, H. and Bahr, D. B. 1998. The effect of surface geometry on fracture permeability: A case study using a sinusoidal fracture. Geophys. Res. Lett. **25**: 813-816.

Warpinski, N. R. 1985. Measurement of Width and Pressure in a Propagating Hydraulic Fracture. Society of Petroleum Engineers Journal **25**: 46-54. 00011648

Weijers, L., Wright, C. A., Sugiyama, H., Sato, K. and Zhigang, L. 2000. Simultaneous Propagation of Multiple Hydraulic Fractures-Evidence, Impact and Modeling Implications. Int. Oil and Gas Conference and Exhibition in China, Beijing, China. 64772

Weill, L. and Latil, M. 1992. Modelling Hydraulic Fractures in a Finite Difference Reservoir Simulator.*in* M. A. Christie, F. V. Da Silva, C. L. Farmer, O. Guillon, Z. E. Heinemann, P. Lemonnier, J. M. M. Regtien, and E. Van Spronsen, editors. ECMOR III: 3rd European Conference on the Mathematics of Oil Recovery. Delft University Press, Delf University of Technology, Delf, Netherland.

White, F. M. 2011. Fluid Mechanics. McGraw Hill.

Witherspoon, P. A., Wang, J. S. Y., Iwai, K. and Gale, J. E. 1980. Validity of Cubic Law for fluid flow in a deformable rock fracture. Water Resour. Res. **16**: 1016-1024.

Wolf, H., König, D. and Triantafyllidis, T. 2003. Experimental investigation of shear band patterns in granular material. Journal of Structural Geology **25**: 1229-1240.

Wong, R. C. K. 2003. A Model for Strain-Induced Permeability Anisotropy in Deformable Granular Media. Canadian Geotechnical Journal **40**: 95-106.

Wong, R. C. K., Barr, W. E. and Kry, P. R. 1993. Stress–Strain Response of Cold Lake Oil Sands. Canadian Geotechnical Journal **30**: 220-235.

Wu, R. 2006. Some Fundamental Mechanisms of Hydraulic Fracturing. Georgia Institute of Technology, Atlanta.

Xia, G. W., Dusseault, M. B. and Marika, E. 2007. A Hydraulic Fracture Model With Filtration For Biosolids Injection. American Rock Mechanics Association.

Xu, B. 2010. Finite element simulation of hydraulic fracturing in unconsolidated sands. Ph.D. Dissertation. University of Calgary, Calgary, AB.

Xu, B. and Wong, R. C. K. 2010. A 3D Finite Element Model for History Matching Hydraulic Fracturing in Unconsolidated Sands Formation. Journal of Canadian Petroleum Technology **49**: 58-66.

Xu, B., Yuan, Y. and Wong, R. C. K. 2010. Modeling of the Hydraulic Fractures In Unconsolidated Oil Sands Reservoir. 44th U.S. Rock Mechanics Symposium and 5th U.S.-Canada Rock Mechanics Symposium. American Rock Mechanics Association, Salt Lake City, Utah. 10-123

Xue, B., Wu, H. a., Wang, X., Lian, Z., Zhang, J. and Zhang, S. 2006. A Three-dimensional Finite Element Model of Hydraulic Progressive Damage. Key Engineering Materials **324-325**: 375-378.

Yeung, K. C. 1995. Cold Flow Production of Crude Bitumen at the Burnt Lake Project, Northeastern Alberta. Sixth UNITAR International Conference on Heavy Crude and Tar Sands, Houston, Texas.

Yeung, K. C. and Adamson, M. F. 1991. Burnt Lake Project - Bitumen production form the Cold Lake oil sands deposit without steam. Pages 77-83 44th Canadian Geotechnical Conference. Canadian Geotechnical Society, Calgary, AB, Canada.

Yuan, S. C. and Harrison, J. P. 2005. Development of a hydro-mechanical local degradation approach and its application to modelling fluid flow during progressive fracturing of heterogeneous rocks. International Journal of Rock Mechanics and Mining Sciences **42**: 961-984.

Zandi, S., Renard, G., Nauroy, F., Guy, N. and M.Tijani. 2010. Numerical Coupling of Geomechanics and Fluid Flow during Steam Injection in SAGD. Page 10 *in* SPE 129739 presented at the Improved Oil Recovery Symposium. Society of Petroleum Engineers, Tulsa, Oklahoma, USA.

Zhai, Z. 2006. Fracturing and Fracture Reorientation in Unconsolidated Sands and Sandstones. PhD Thesis. The University of Texas at Austin, Austin.

Zhai, Z. and Sharma, M. M. 2005. A New Approach to Modeling Hydraulic Fractures in Unconsolidated Sands. SPE Annual Technical Conference and Exhibition. Society of Petroleum Engineers, Dallas, Texas. SPE 96246

Zhang, G. M., Liu, H., Zhang, J., Wu, H. A. and Wang, X. X. 2010. Three-dimensional finite element simulation and parametric study for horizontal well hydraulic fracture. Journal of Petroleum Science and Engineering **72**: 310-317.

Zhao, S., Qi, Q., Ouyang, Z. and Li, H. 2012. Mechanism of Deep Hole High Hydraulic Fracturing Prevent Rock Burst in Deep Thick Coal Seam. International Society for Rock Mechanics.

Zhou, J., Dong, Y., Pater, C. J. d. and Zitha, P. L. J. 2010. Experimental Study of the Impact of Shear Dilation and Fracture Behavior During Polymer Injection for Heavy Oil Recovery in Unconsolidated Reservoirs. Page 14 Canadian Unconventional Resources and International Petroleum Conference. SPE, Calgary, AB. SPE 137656-MS

Zimmerman, R. W. and Bodvarsson, G. S. 1996. Hydraulic conductivity of rock fractures. Transport in Porous Media **23**: 1-30.

Zimmerman, R. W. and Yeo, I. W. 2000. Fluid flow in rock fractures: From the Navier-Stokes equations to the cubic law. Pages 213-224 Dynamics of Fluids in Fractured Rock. AGU, Washington, DC.

Appendix A: Validation of Touhidi-Baghini's Model for Sandstone

Touhidi-Baghini's shear permeability model (Touhidi-Baghini, 1998) has been proposed for both isotropic unloading (steam injection) and shearing of oil sands which are unconsolidated sands. It was decided to further validate this model against weakly consolidated or consolidated sandstones to see if this criterion still holds. For this purpose, the published data (in the literature) about permeability measurement during triaxial testing of Red Sandstone (Hu et al., 2010) has been chosen. This is shown in Fig A-1. The uniaxial compressive strength (UCS) of this sandstone is approximately 14 MPa. Fig A-1 shows that the permeability of the samples decreases up to a certain level of compaction and then remains almost constant when dilation starts and eventually increases. Therefore, the constant part of permeability is eliminated from the data (shown by the dashed-line in Fig A-1). The permeability evolution (ratio of k/k0) during compaction is shown in Fig. A-2.

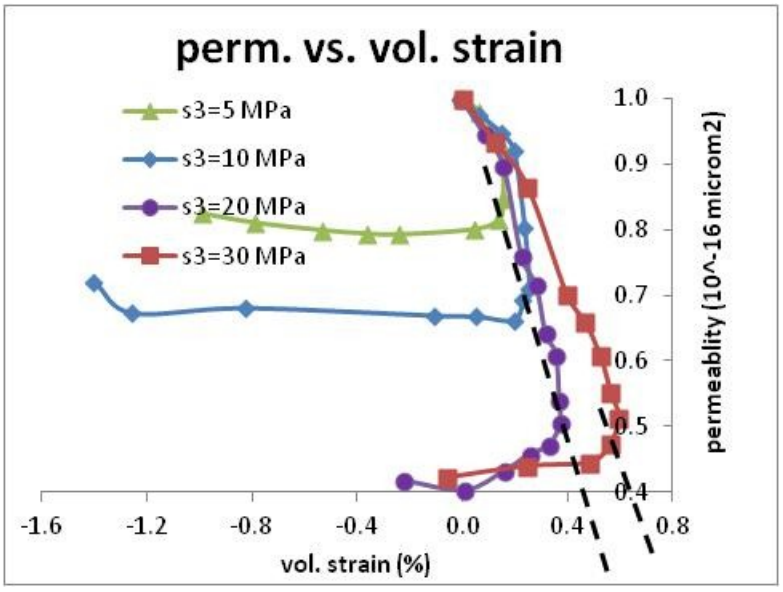

Fig A-1: Permeability measurement during triaxial tests conducted by Hu et al. (2010)

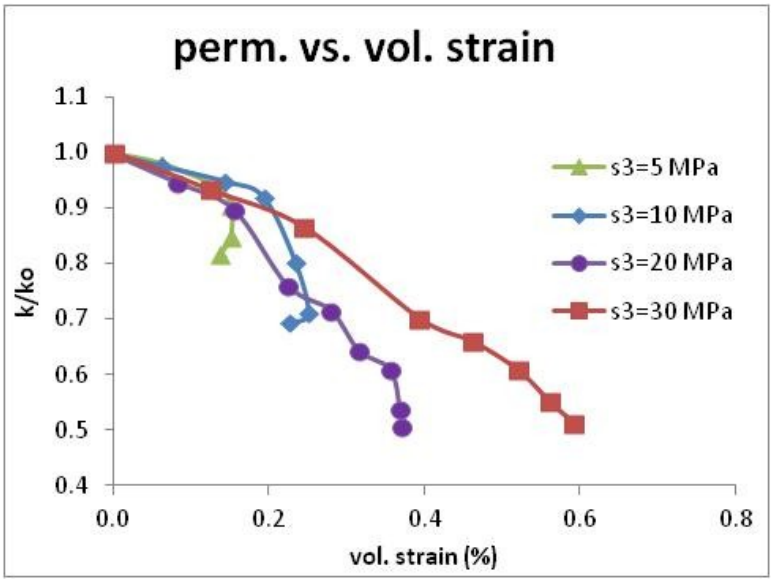

Fig. A-2: Permeability evolution of Red Sandstone during compaction (Hu et al., 2010)

According to Touhidi-Baghini's shear permeability model (1998), which is shown by Eq. (2-34), there should be a linear relationship between ($ln\ k/k_0$) and the volumetric strain. For this purpose, the data of Hu et al. (2010) are shown in Fig. A-3 with a linear equation fitted to the data.

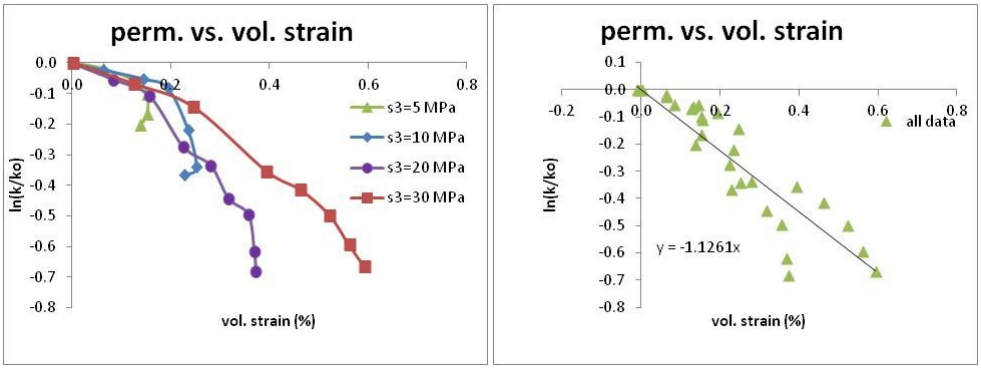

Fig. A-3: Variation of permeability ratio of Red Sandstone during compaction (Hu et al., 2010)

From Fig. A-3, the coefficient of (B/ϕ_0) is equal to -1.1143. Knowing the initial porosity of 0.21, the B factor will be equal to -0.236. Touhidi-Baghini's model with B=0.233 is illustrated in Fig. A-4 for all the experiments.

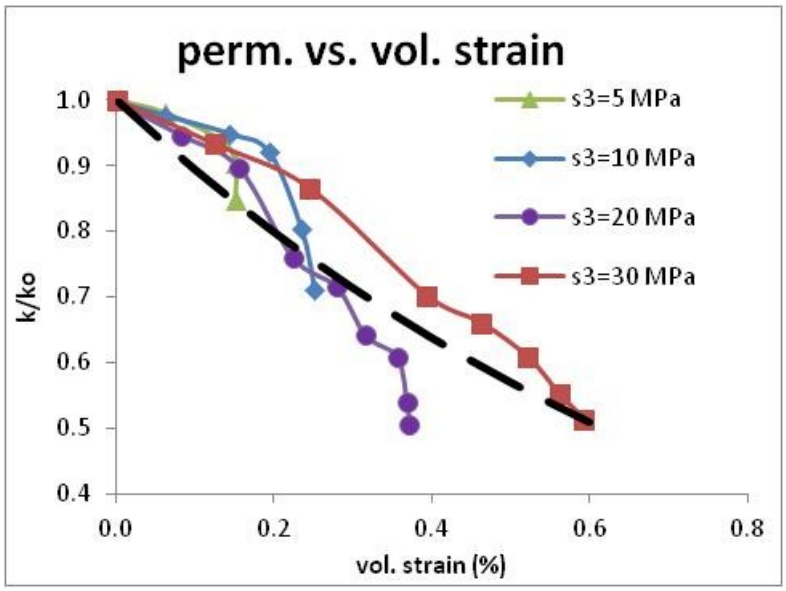

Fig. A-4: Touhidi-Baghini's model with B=0.233 for all the experiments done by Hu (2010)

Fig. A-4 shows that Touhidi-Baghini's model is consistent with the weakly consolidated Red Sandstone test results and still holds for this kind of material.

Appendix B: Constitutive Model Calibration for Samples from Cold Lake Oil Sands Based on Triaxial Compression Tests

A bilinear Mohr-Coulomb model (with strain hardening/softening behavior) was calibrated against a series of triaxial tests on Cold Lake oil sands (Wong et al., 1993). Wong (1993) performed triaxial compression tests on Cold Lake oil sands at confining stresses of up to 18 MPa and temperatures of up to 200°C using core samples with a diameter of 89 millimeters . The constitutive model calibration was performed on these experiments (at confining stresses of 0.6, 0.7, 1, 4.5, 9 and 12 MPa) based on the method proposed by Nouri (2009). In the calibration process, the loading/unloading cycles during some of the experiments were neglected.

To determine the elastic modulus of the oil sand samples under the applied confining stresses, the following function is used:

$$E = KP_a\left(\frac{\sigma_c}{P_a}\right)^{\eta}, \quad \text{(B-1)}$$

where σ_c is the confining stress, Pa is the reference pressure, and K and η are constants. For the selected experiments, the K and η are found to be 539.84 and 0.5229, respectively. For the Poisson ratio, the values calculated by Wong (1993) were used. These were measured for axial strains of less than 0.2%.

To differentiate the two lines of the Mohr-Coulomb failure envelope, the confining stresses of 0.6, 0.7, 1 and 4.5 were selected as the low effective confining stress and the confining stresses of 9 and 12 MPa were selected for the high range of effective confining stress. As explained by Nouri (2009), the friction angle, and cohesion and dilation angles of the oil sand samples are defined as a piecewise linear function of equivalent plastic strain or EPS (Itasca Consulting Group Inc., 2011; Taghipoor et al., 2013).

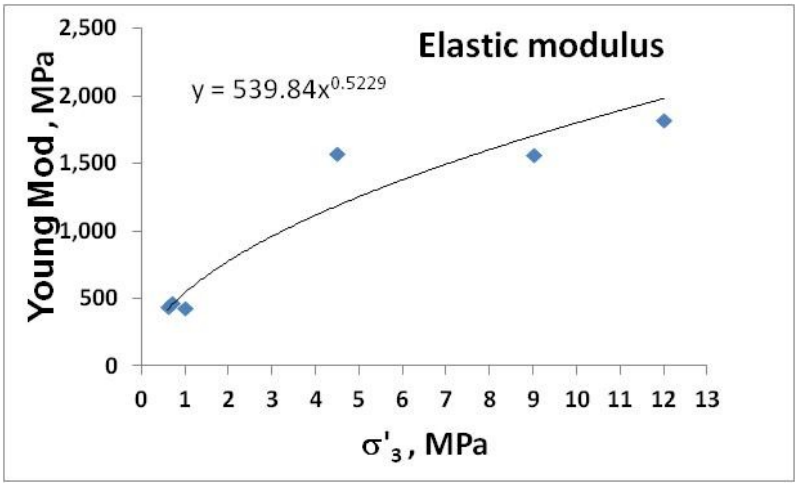

Fig. B-1: Elastic modulus of the oil sands as a function of confining stress

Sulem et al. (1999) propose that all the softening must be related to microcracking, which results in a drop in the material's tensile strength during all stages of deformation. However, it is more appropriate to assume that the material loses its capacity to mobilize additional frictional resistance (Sulem et al., 1999). Accordingly, we assume that the tension cut-off is constant up to the peak of the mobilized friction angle (peak strength), implying that there is no microcracking during the friction hardening phase. In other words, the friction angle increases with the EPS before the peak strength and remains constant after that. Beyond the peak strength, the cohesion fully mobilizes and drops as a function of EPS while the friction angle remains constant.

In this plasticity model, two failure envelopes are used to describe the yield processes for low and high confining stresses. It is assumed that the material strength increases with accumulation of plastic shear strain until it reaches a peak value. Then the shear strength decreases because the material's cohesion degrades, while the friction angle remains constant.

The yield surfaces can be expressed in the following form (Nouri et al., 2009; Jafarpour et al., 2012):

$$F = T - (q + P)\mu = 0, \quad \text{(B-2)}$$

where P is the mean effective stress, and T is the square root of the second invariant of the deviatoric stress tensor in an axisymmetric state of stress (as in a triaxial compression experiment), and both are defined as:

$$P = \left(\sigma'_z + 2\sigma'_r\right)/3, \quad \text{(B-3)}$$

$$T = \left|\sigma'_z - \sigma'_r\right|/\sqrt{3}, \quad \text{(B-4)}$$

and μ is the friction coefficient which is equal to tan(ϕ_σ). It is related to the friction angle (ϕ_a) in the following form:

$$\tan\phi_\sigma = \frac{2\sqrt{3}Sin\phi_a}{3 - Sin\phi_a}, \quad \text{(B-5)}$$

and q is equal to the tension limit (q_r) at low effective confining stress (LECS) which is related to real cohesion (C_r) and the friction angle (ϕ_r) using the following equation:

$$q_r = -C_r/\tan\left(\phi_r\right), \quad \text{(B-6)}$$

The yield surface intersects the T-axis at:

$$T = q_r\mu_{\sigma r} = \left(\frac{2\sqrt{3}Cos\left(\phi_r\right)}{3 - Sin\phi_r}\right)C_r, \quad \text{(B-7)}$$

More details on this formulation can be found in Jafarpour et al. (2012) and Nouri et al. (2009).

For the mobilized dilation angle, the equation proposed by Vermeer and De Borst (1984) is used:

$$\sin\psi = \frac{\dot{\varepsilon}^p_v}{-2\dot{\varepsilon}^p_{\cdot} - \dot{\varepsilon}^p_v}, \quad \text{(B-8)}$$

where ψ is the mobilized dilation angle and $\dot{\varepsilon}^p_v$ and $\dot{\varepsilon}^p_{\cdot}$ are the plastic volumetric strain rate and the maximum principal plastic strain rate, respectively. Fig. B-2 shows the calculated friction and dilation angles of Cold Lake oil sands based on the triaxial compression tests.

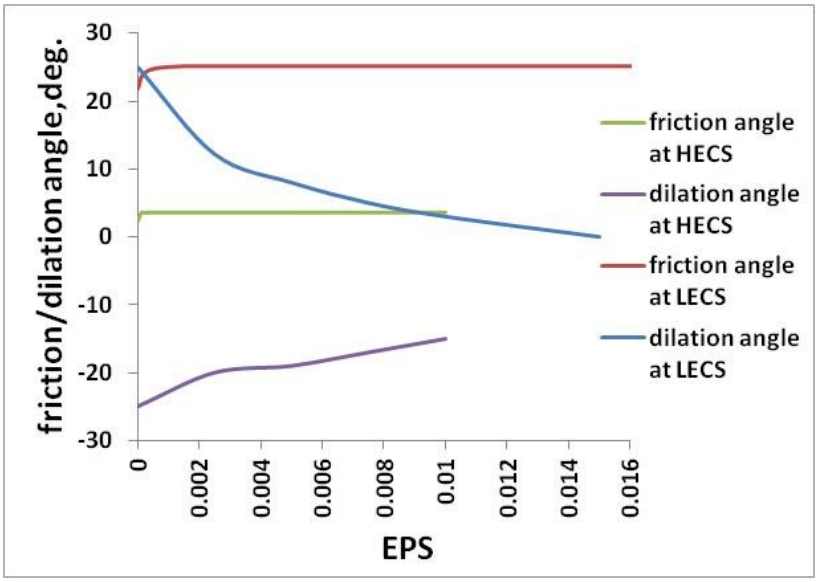

Fig. B-2: Friction and dilation angle of Cold Lake oil sands as a function of the equivalent plastic strain at low and high effective confining stresses

According to the calibration method, cohesion also increases until the peak strength and then drops to a residual value with EPS, representing the degradation of the material. The variation of cohesion with EPS at HECS and LECS is shown in Fig. B-3.

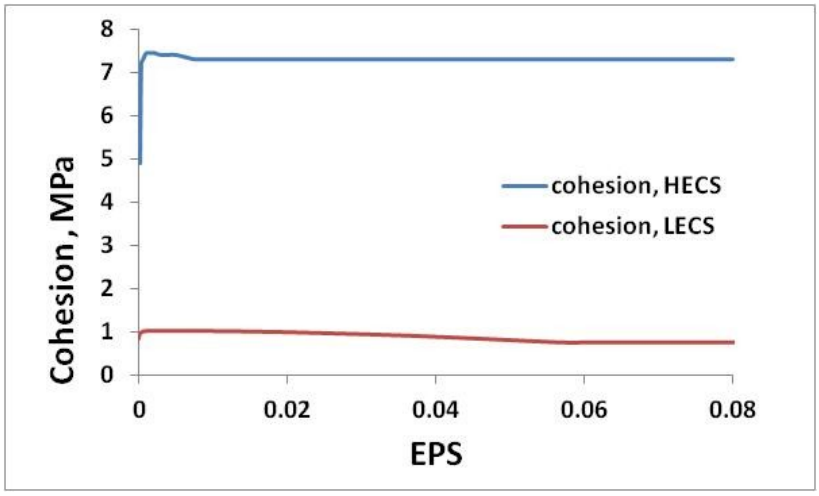

Fig. B-3: Cohesion of Cold Lake oil sands as a function of the equivalent plastic strain at low and high effective confining stresses

The average grain size (D_{50}) of the oil sands is 0.08 millimeters (Dusseault, 2001), which is used in fracture energy regularization to reduce the mesh dependency.

The simulation of the triaxial compression tests was performed with the above-calculated properties. The results are shown in Fig. B-4. A typical shear band captured in the simulation at low confining pressure is also shown in this figure.

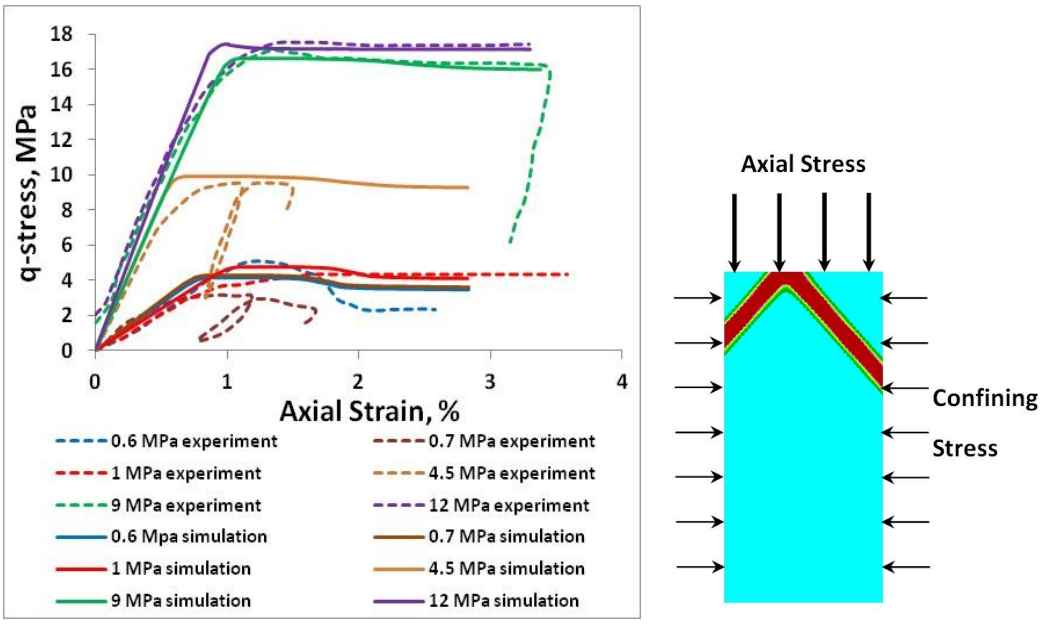

Fig. B-4: Simulation results for the triaxial compression tests performed by Wong et al. (1993): Top) the stress-strain plots for all tests, and Bottom) a typical shear band captured for the lowest effective stress test